CZECH TECHNICAL UNIVERSITY IN PRAGUE

FACULTY OF NUCLEAR SCIENCES AND PHYSICAL ENGINEERING

DEPARTMENT OF MATERIALS

DISSERTATION THESIS

MULTISCALE STRAIN LOCALIZATION IN THERMOMECHANICAL FATIGUE OF NiTi SHAPE MEMORY ALLOYS

Ing. Lukáš Kadeřávek

Degree Program :	Applications of Natural Sciences
Field of Study :	Physical Engineering
Specialization :	Structure and Properties of Materials

Supervisor :

prof. Dr. Ing. Petr Haušild / CTU FNSPE – Prague

Co-Supervisor – specialist :

RNDr. Petr Šittner, CSc. / FZU CAS – Prague

Number of Pages :	143	*Date :* March 2023
Number of Figures :	87	
Number of Tables :	3	*Number of copy :* 1

Bibliographic Entry

Author	Ing. Lukáš Kadeřávek Czech Technical University in Prague, Faculty of Nuclear Sciences and Physical Engineering, Department of Materials
Title of Dissertation	Multiscale strain localization in thermomechanical fatigue of NiTi shape memory alloys
Degree Program	Applications of Natural Sciences
Field of Study	Physical Engineering
Supervisor	prof. Dr. Ing. Petr Haušild, Department of Materials, Faculty of Nuclear Sciences and Physical Engineering - CTU, Prague
Supervisor specialist	RNDr. Petr Šittner, CSc., FZU - Institute of Physics of the Czech Academy of Sciences, Prague
Academic Year	2022/2023
Number of Pages	143
Keywords	NiTi, SMA, Shape memory alloys, fatigue, localization, digital image correlation, Lüders bands, plasticity, electron microscopy, in-situ studies, martensitic transformation, superelasticity, shape memory

Bibliografický záznam

Autor	Ing. Lukáš Kadeřávek České vysoké učení technické v Praze Fakulta jaderná a fyzikálně inženýrská Katedra materiálů
Název práce	Víceúrovňová lokalizace deformace při termomechanické únavě slitin s tvarovou pamětí NiTi
Studijní program	Aplikace přírodních věd
Studijní obor	Fyzikální inženýrství
Školitel	prof. Dr. Ing. Petr Haušild České vysoké učení technické v Praze Fakulta jaderná a fyzikálně inženýrská Katedra materiálů
Školitel specialista	RNDr. Petr Šittner, CSc. Fyzikální ústav AV ČR, v. v. i. Oddělení funkčních materiálů
Akademický rok	2022/2023
Počet stran	143
Klíčová slova	NiTi, SMA, slitiny s tvarovou pamětí, únava, lokalizace deformace, digitální korelace obrazu, Lüdersův pás, plasticita, elektronová mikroskopie, martenzitická transformace, superelasticita, tvarová paměť

Abstract

Commercial polycrystalline NiTi shape memory alloy (SMA) displays strain of several percent (~5%) due to stress-induced cubic to monoclinic martensitic transformation, which is recoverable in cyclic thermomechanical loads. This gives rise to functional stress-strain-temperature behaviors, which are already utilized in engineering applications. Assuming that only elastic deformation and deformation/transformation processes derived from martensitic transformation take place, stress-strain-temperature responses of SMAs are completely reversible in closed-loop thermomechanical cycles for the very large number of cycles comparable to elastic deformation only. In reality, this is not the case, since plastic deformation accompanies martensitic transformation proceeding under stress and causes cyclic instability of stress-strain-temperature responses, accumulation of damage, nucleation, and growth of cracks and fatigue failure after a relatively low number of cycles in tension even in case of a relatively small mean strain and strain amplitude. A unique feature of NiTi SMAs, which further deteriorates fatigue performance, is the tendency of this material to localized macroscopic deformation in tension.

The motivation of this thesis was to investigate how the fatigue properties of commercial NiTi can be improved. If this is achieved, the range of engineering applications of NiTi would broaden significantly. Since the strain localization was identified to be very important for the fatigue performance of NiTi, a unidimensional digital image correlation method has been developed and used to follow strain localization patterns (temporal and spatial distribution of local strains) during monotonic and cyclic (thermo)mechanical loads on thin NiTi wires with controlled austenitic microstructures. Following, key experimental results beyond the state-of-the-art in the field were obtained.

As concerns strain localization in tension, it was found that tensile deformation of superelastic NiTi wire taking place via stress-induced martensitic transformation followed by plastic deformation of stress-induced martensite gives rise to complex strain localization phenomena (long plateaus due to deformation localized in macroscopic Lüders bands, localized deformation in successive multiple plateaus, necking, etc.). It was newly discovered that, in addition to the localized deformation of NiTi via stress-induced martensitic transformation, localized plastic deformation may occur also during the plastic deformation of the wire in the martensite phase. It was shown to proceed either as

necking leading to fracture at 13-15 % strain or via propagation of macroscopic Lüders band fronts with unusually large plastic strain (up to ~ 40 %).

As concerns to fatigue performance of NiTi wires cycled in tension, it was found that the number of cycles until failure: i) decreases with increasing test temperature (plateau stress) regardless of the applied strain or stress limit, ii) does not correlate with the instability of stress-strain response and accumulated residual strain (functional fatigue), iii) strain localization phenomena drastically affect the performance of superelastic NiTi wires in partial superelastic cyclic tests.

The problem with strain localization in fatigue is that the material displays cyclic softening and, therefore, tends to deform (transform) only in locations, where Lüders band fronts move upon tensile cycling. Plastic deformation accompanying martensitic transformation proceeding under stress (only in locations, where the Lüders band fronts move) generates lattice defects and internal stress in the wire microstructure which accumulate upon tensile cycling, while in locations, where Lüders band fronts do not move, wire microstructure remains unaffected.

It was found that periodic overloading of superelastically cycled NiTi wire may result in a significant increase in fatigue life. The observation was explained by the beneficial effect of periodic plastic deformation taking place selectively at crack tips in cycled material.

A very long fatigue lifetime of commercial NiTi wire was achieved in superelastic tensile cycling with adaptive limits at 10 °C (N_c > 200000 cycles). This is considered a real breakthrough. The observation was explained simply as a consequence of a combination of minimization of the upper plateau stress and optimization of virgin austenitic microstructure for resistance to accumulation of fatigue damage.

Abstrakt

Komerčně vyráběné polykrystalické slitiny s tvarovou pamětí NiTi vykazují deformaci o několik procent (~5 %) v důsledku napětím indukované martenzitické transformace (z kubické do monoklinické mřížky), která je vratná při cyklickém termomechanickém zatěžování. Vzniká tak funkční chování napětí-deformace-teplota, které lze využít pro inženýrské aplikace. Za předpokladu, že dochází pouze k elastické deformaci a k deformačně/transformačním procesům odvozených od martenzitické transformace, jsou napěťově-deformačně-teplotní odezvy slitin s tvarovou pamětí zcela vratné v rámci termomechanického cyklování pro velmi velký počet cyklů srovnatelný pouze s elastickou deformací. Ve skutečnosti tomu tak není, protože plastická deformace doprovází martenzitickou transformaci probíhající pod napětím a způsobuje cyklickou nestabilitu napěťově-deformačně-teplotní odezvy, akumulaci poškození, nukleaci a růst únavových trhlin a finálně lom po relativně malém počtu cyklů v tahu i v případě relativně malé střední deformace a amplitudy deformace. Jedinečnou vlastností slitin s tvarovou pamětí na bázi NiTi, která dále zhoršuje únavové vlastnosti, je tendence tohoto materiálu k lokalizované makroskopické deformaci v tahu.

Motivací této práce bylo zjistit, jak lze zlepšit únavové vlastnosti komerčních slitin NiTi v technických aplikacích. Pokud by se to podařilo, výrazně by se rozšířili možnosti uplatnění NiTi. Jelikož bylo zjištěno, že lokalizace deformace je velmi důležitá pro únavové vlastnosti NiTi, byla vyvinuta metoda „jednorozměrné“ digitální obrazové korelace, která byla použita ke sledování změn lokalizované deformace (časové a prostorové rozložení lokálních deformací) během monotónního a cyklického termomechanického zatěžování tenkých drátů NiTi s kontrolovanou mikrostrukturou. Následně se podařilo získat klíčové experimentální výsledky přesahující nejnovější poznatky v této oblasti.

Pokud jde o lokalizaci deformace v tahu, bylo zjištěno, že tahová deformace superelastického NiTi drátu probíhající prostřednictvím napětím indukované martenzitické transformace následovanou plastickou deformací martenzitu vede ke komplexním jevům lokalizace deformace (dlouhá napěťová plata v důsledku deformace lokalizované v makroskopických Lüdersových pásech, lokalizovaná deformace v po sobě jdoucích vícenásobných platech, krčku atd.). Nově bylo zjištěno, že kromě lokalizované deformace NiTi prostřednictvím martenzitické transformace vyvolané napětím může docházet k lokalizované plastické deformaci také během plastické deformace drátu

v martenzitické fázi. Ukázalo se, že probíhá buď v krčku vedoucí k lomu při 13-15 % deformaci, nebo prostřednictvím šíření makroskopických Lüdersových pásů s neobvykle velkou lokalizovanou plastickou deformací (až ~ 40 %).

Pokud jde o únavové vlastnosti NiTi drátů cyklicky namáhaných v tahu, bylo zjištěno, že počet cyklů do porušení: i) klesá s rostoucí zkušební teplotou (transformačním napětím) bez ohledu na aplikovanou deformaci nebo mezní napětí, ii) nekoreluje s nestabilitou napěťově-deformační odezvy a akumulovanou zbytkovou deformací (funkční únavou), iii) jevy lokalizace deformace drasticky ovlivňují vlastnosti superelastických NiTi drátů i při částečných superelastických cyklických zkouškách.

Problém s lokalizací deformace při únavě spočívá v tom, že materiál vykazuje cyklické měknutí, a proto má tendenci se deformovat (transformovat) pouze v místech, kde se při cyklickém tahu pohybují Lüdersovy pásy. Plastická deformace doprovázející martenzitickou transformaci probíhající pod napětím (pouze v místech, kde se pohybují čela Lüdersových pásů) vytváří v mikrostruktuře drátu krystalové poruchy a vnitřní napětí, které se při cyklování v tahu hromadí, zatímco v místech, kde se čela Lüdersových pásů nepohybují, zůstává mikrostruktura drátu nepoškozena.

Bylo zjištěno, že periodické přetěžování superelasticky cyklovaného NiTi drátu může vést k výraznému prodloužení únavové životnosti. Toto pozorování bylo vysvětleno příznivým účinkem periodické plastické deformace, která probíhá selektivně na čelech trhlin v cyklicky zatěžovaném materiálu, tak může docházet k řízené retardaci růstů trhlin.

Velmi dlouhé únavové životnosti komerčního NiTi drátu bylo dosaženo při superelastickém cyklování v tahu za pomoci adaptivních limitů testu, při 10 °C (N_c > 200 000 cyklů). To je považováno za skutečný průlom. Výsledek lze vysvětlit jako důsledek kombinace minimalizace horního napěťového transformačního plata a optimalizace původní austenitické mikrostruktury drátu pro odolnost vůči akumulaci únavového poškození.

Acknowledgment

I would like to sincerely thank both of my supervisors Prof. Petr Haušild and Dr. Petr Šittner for their leadership and assistance during my studies. This thesis represents only a portion of results acquired in past years of working within the area of shape memory alloys at the Institute of Physics CAS in Prague, in the Department of Functional Materials, namely, in the Laboratory of Functional Materials and Composites, where I spent most of my time and done most of my experiments, and at the Faculty of Nuclear Sciences and Physical Engineering of the Czech Technical University in Prague, where I attended all courses and training in several disciplines in the course of the Ph.D. program.

I am grateful to Prof. Haušild for giving me an opportunity to study at the Czech Technical University in Prague at the Faculty of Nuclear Sciences and Physical Engineering allowing me to investigate various approaches, techniques, and more in-depth knowledge in several areas, supporting me academically and giving me his time and expertise.

I would like to thank Dr. Petr Šittner with whom I have been working on different topics and several progressive directions in the field of Shape memory alloys not only the NiTi-based but a lot broader area of material sciences. I would like to thank him for teaching me a great deal about how to conduct methodical scientific research and develop skills that will benefit me immensely in my future work. I think him for including me in a variety of research activities and projects, and for giving me academic freedom and the opportunity for developing research areas and topics on my own.

I would like to sincerely thank all the members of the Faculty of Nuclear Sciences and Physical Engineering for their excellent professionalism, leading-edge education program, and wonderful environment. My thanks are also extended to the members of laboratories of functional materials and composites, electron microscopy, and to all members of colleagues and institutes with whom we participate in the research grants and projects.

Special thanks for the help and ingenuity of the technical staff of the Institute of Physics, providing support during experiments or realization of the novel equipment required for the proper testing at controlled conditions.

My sincere thanks go to Dr. Orsolya Molnárová for the support with the post-mortem transmission electron microscopy and characterization on several samples for better understanding of the evolution of the microstructure, before investigated on mesoscale.

Finally, I would like to express my deepest gratitude to my family and friends for their constant support, help, and unconditional love throughout all my studies.

Aims of the Thesis

1. A deeper understanding of fatigue of NiTi shape memory alloys, characterization of strain localization, and accumulation of irreversible changes in the microstructure.
2. Investigation of martensitic transformation localization effects during cyclic deformation of NiTi alloys and limits of reversibility of martensitic transformation.
3. Analysis of the temperature dependence of transformation/deformation modes in NiTi alloys having different microstructures.
4. Examination of the effect of sample preparation, especially heat treatment and shape modification, on fatigue of NiTi alloys.

Abbreviations

BF – bright field

CW – cold work

DF – dark field

DIC – digital image correlation

EBSD – electron backscatter diffraction

EDS – energy dispersive spectroscopy

HCF – high-cycle fatigue

KAM – Kernel average misorientation

LCF – low-cycle fatigue

MT – martensitic transformation

PE – pseudoeleasticity

PT – pulse treatment

RT – room temperature

SAED – selected area electron diffraction

SE – superelasticity

SEM – scanning electron microscopy

SM – shape memory

SMAs – shape memory alloys

SME – shape memory effect

TEM – transmission electron microscopy

List of Figures

Table of Contents

1 Introduction

Since the discovery of the shape memory effect in the 1930s by the Swedish chemist Gustav Arne Ölander on Au-Cd, shape memory alloys (SMAs) constantly attract attention for their wide range of particularly unmatched capabilities and characteristics in numerous fields. After the discovery of NiTinol alloy in 1963, the shape memory alloys, and technology based on NiTi flourished and filled numerous gaps in the application fields. In particular, exciting functionalities of NiTi were used in medical devices and implants [1-6] and substituted already existing solutions and engineering designs in the aerospace industry, mechanical and civil engineering. The shape memory behavior is usually separated into two types of shape memory effects (SMEs), mechanical memory (pseudoelasticity, PE, often called superelasticity, SE) and thermal memory (one/two-way SMEs). Both types, however, origin from the existence of reversible martensitic transformation, a solid-state transformation where a parent phase (austenite) with higher symmetry of the crystal lattice transforms to a daughter phase (martensite) having single or several variants of the crystal lattice/s with lower symmetries and theoretical capability to be fully reversible. The martensitic transformation takes place upon cyclic thermal and/or mechanical loading. While the reversible martensitic transformation has been under constant development, various fundamental aspects have been described. However, many links and connections between multiscale problems of SMAs are missing in relation to the localization of martensitic transformation. These aspects can lead to a better understanding of the fatigue properties of SMAs and to the development of alloys with high transformation temperatures and fatigue resistance (both with thermal and mechanical stability). The necessity to fill these gaps in the area is giving a strong driving force for the wide research activities and trends in the SMAs field [7-10].

1.1 Overview of chapters 2 to 6

Chapter 2 introduces the fundamental aspects of NiTi shape memory alloys as follows: (i) martensitic phase transformation and mechanical behavior of shape memory and superelastic NiTi alloys under thermomechanical loading, (ii) crystallography of the shape memory, (iii) the benefits of functional behavior for medical and technical applications, (iv) origins of localized deformation in NiTi-based shape memory alloys, (v) the fatigue issues accompanied the martensitic transformation of NiTi.

Chapter 3 illustrates the techniques and methods that have been applied to study the shape memory effect during stress-induced B2 to B19' phase transformation or actuator cycling under constant stress, mechanical properties of Ni-rich and Ti-rich shape memory alloys with different heat treatments. Tensile tests until failure, cyclic deformation in the whole deformation range, and actuator cycling within a wide stress-strain-temperature range in tension, coupled with in-situ techniques such as digital image correlation and EBSD. The microstructure techniques are also described.

Microstructure evolution of an in-situ tested sample in monotonic tension under the SEM, the texture, and plastic deformation of a local area are discussed and evaluated using electron back-scattering diffraction (EBSD).

Chapter 4 introduces the techniques used for the preparation of NiTi wire samples to distinguish between fast and conventional heat-treatments (conventional furnace and or pulse treated).

Chapter 5 presents the response of NiTi during stress-induced transformation during monotonic thermomechanical loading of samples treated conventionally in the furnace and by a fast electric pulse.

Study of the plastic deformation of the superelastic NiTi wires during monotonic loading in tension (B2→B19' and beyond). To address the complexity and flexibility of the transformation-deformation mechanisms, which by novel discovery and understanding may open a completely new potential for the use and application of NiTi shape memory alloys. The macro mechanism is discussed mainly in contrast to the detailed DIC study, which then is in-depth discussed in contrast to microstructural changes studied by TEM. The mechanisms of localization on a micro-scale are revealed by the EBSD method during in-situ loading of NiTi in SEM.

Chapter 6 presents the fatigue properties of conventionally annealed wires. The effect of composition, type of testing, testing temperature, and stress-strain limits the fatigue performance of the NiTi SMAs. The residual strains upon unloading were evaluated and compared to the functional macroscopic stress-strain responses.

Digital image correlation study on the B2→B19' phase transformation and the degradation in the conventionally treated wires under various range stress-strain limits.

The evolution of local axial strains during propagation of the localized Lüders band fronts was analyzed in detail from cyclic experiments. The importance of the temperature under which the transformation takes place is discussed in both types of modes (superelasticity, thermal cycling). The limits for stress-induced transformation accompanied by plastic deformation are discussed in a range of microstructures and testing temperatures. The geometrical shape and strain rate sensitivity of martensitic transformation are presented.

Study about the reinforcement of superelastic NiTi by overloading cycles during cyclic loading-unloading in tension for two typical annealing conditions for medical grade NiTi wires and various testing temperatures. The fractographical analysis of fracture surfaces for linking the thermomechanical history with the effect on the fatigue life and the drawbacks and the potential benefits of the focused structural fatigue.

Detailed digital image correlation study on 2D structures with identic microstructure loaded cyclically in tension where actively the reversible B2→B19' phase transformation takes place in form of macroscopic bands. To present the influence of the material degradation (functional fatigue) and the effect of local stress risers affecting the local accumulation of defects (structural fatigue) the tracking of 2D local strain maps was studied in contrast to the change of macro mechanical behavior.

Study on the elaborate manufacturing and controlling the development of microstructure during cyclic loading-unloading consisting of B2→B19' phase transformation capable of careful self-adapting of the functional behavior to suppress the formation and accumulation of lattice defects leading to failure. The study is accompanied by a detailed DIC study and post-mortem TEM analysis.

2 State of the art

Shape memory alloys (SMAs) exhibit diffusionless martensitic phase transformations (MTs) the progress of which can be controlled by changes in temperature and/or mechanical stress. Martensitic transformation is first-order solid-state transformation proceeding via the motion of internal interfaces. Martensitic transformations in SMAs are phase reversible and can be strain reversible under special circumstances. SMAs display unique functional thermomechanical properties which derive from martensitic transformations, particularly from deformation processes derived from martensitic transformation.

The functional thermomechanical properties of SMAs, depend on alloy composition, defect density, thermo-mechanical treatment (i.e., annealing, precipitation, quenching, aging, etc.), grain size, the shape of the microstructure elements, applied stress during transformation, maximal strain, ductility and ultimate tensile strength of the particular microstructure, purity of the initial composition (the content of additives forming inclusions), the temperature at which is the microstructure forced to transform. One might add other aspects, that might play a role in fatigue such as an environment with accelerated corrosion. However, as it will be shown these effects seem less important in comparison with the formation of martensite or defects during phase transformation in the initial (virgin) microstructure with particular composition unless using extreme environments or combined effects such as high stress and/or high temperature in harsh environments [8-10,11-17]. While the other effects might be regulated by the design parameters of the structure or limitation of the working conditions (i.e., load or displacement), martensitic transformation is allowing for large tunability of performance/output control and optimization of the properties of the SMAs for the specific applications. Martensitic transformation plays a key role in SMA fatigue, which is the focus of this thesis.

According to the state-of-the-art understanding of SMAs fatigue, there is functional fatigue (evolution of stress-strain-temperature response upon cycling and structural fatigue (accumulation of damage and number of cycles until failure) [18]. These terms are strictly related to the observations regarding the classical and the simplest testing techniques of materials - the tensile/compressive testing (i.e., stress-strain characteristic). By other means, one can observe a drastic degradation of functional behavior (residual strain, transformation strain, and evolution of hysteresis), therefore, labeled as functional

fatigue. However, when a sudden failure occurs in a relatively stable structure due to the cyclic loading creating cracks, it is called structural fatigue [19-20]. Therefore, we would like to emphasize the importance of the multi-scale localization present in NiTi-based SMAs often accompanied by plastic deformation, which leads to fatigue crack initiation. Investigation of the localization of strain from the macroscale to the nanoscale is of high importance. It affects the generation and cyclic accumulation of lattice defects (i.e., the evolution of the microstructure upon cycling), which in turn results in the gradual change of functional behavior and affects fatigue performance.

2.1 Functional thermomechanical properties of shape memory alloys

The functional thermomechanical behavior SMAs include superelasticity, shape memory effect, and thermomechanical actuation (ability to generate force and perform work in thermomechanical load cycles). There are many other useful and interesting physical properties (e.g., the ability to dump mechanical vibrations due to hysteresis or generation/absorption of latent heat) but they are less important.

In the case of the shape memory effect, the SMA element deformed at low temperature in the martensite state undergoes a large deformation after mechanical loading and recovers this deformation (i.e., original shape) when it undergoes reverse martensitic transformation upon stress-free heating above austenite finish temperature, as shown in Fig. 1a.

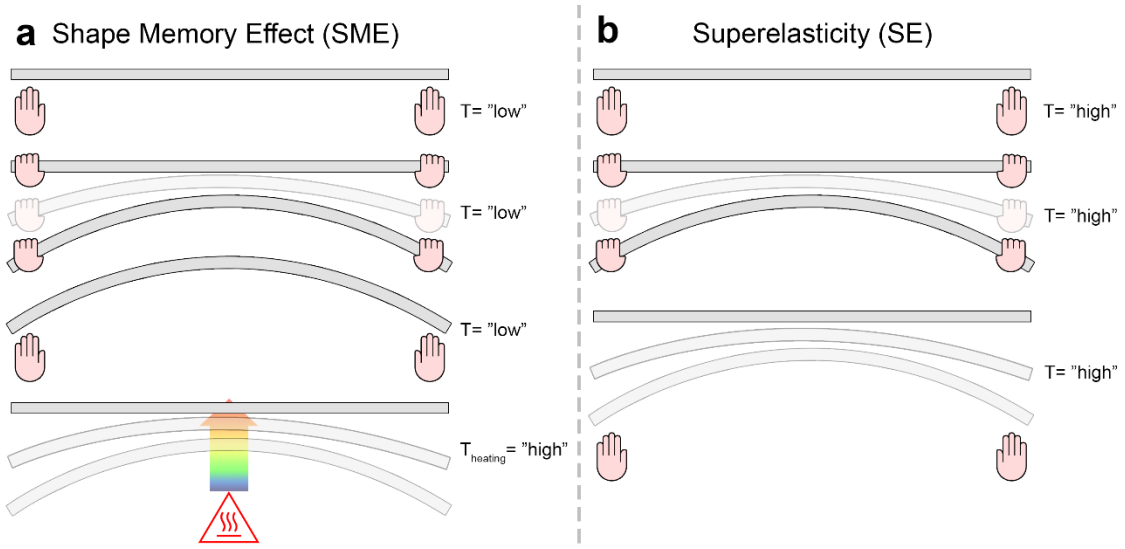

Figure 1: Schematic illustration of a difference between two major behaviors possessed by the shape memory alloys: a) Shape memory effect and b) Superelasticity.

In the case of superelasticity, the SMA element deformed at "high" temperature (by twisting, bending, compressing, tensioning, compressing, or combined loading) reach large deformations and then retrieve the original shape upon unloading (Fig. 1b) [7,8,21].

In the case of actuation, the SMA element loaded by an elastic spring deforms reversibly in the thermal cycle (i.e., generates force and performs mechanical work upon thermal cycling).

2.2 Crystallography of martensitic transformation

The functional thermomechanical properties are due to the change of crystal structure between austenite and martensite. Therefore, these structural changes have to be investigated in detail to develop engineering applications of SMAs. As schematically shown in Fig. 2a-d, the microstructure of austenite with the highest symmetry can transform to the single or multiple variants either oriented in a particular direction (usually the direction in which a mechanical loading is applied) or self-accommodated one to multiple possible variants with nature goal to minimize the internal energy. The martensitic transformation tends to create oriented or self-accommodated variants to minimize the strain energy associated with the shape change [7, 22-24].

The SMAs reversible martensitic transformation is considered as:

- a diffusionless process with the cooperative movement of the atoms, with relatively small displacements of around 1/10 of the distance between atoms.
- In theory, the SMAs are to a large extent reversible, while only a very small number of irreversible defects are introduced.

Used terminology for martensitic transformation was adopted from the well-known effect of steel, specifically the quenching process of carbon steels which induced large volume variation inside the microstructure, thus creating many oriented defects and significantly hardening the microstructure. However, unlike for SMAs such martensitic transformation in carbon steels is not reversible [25].

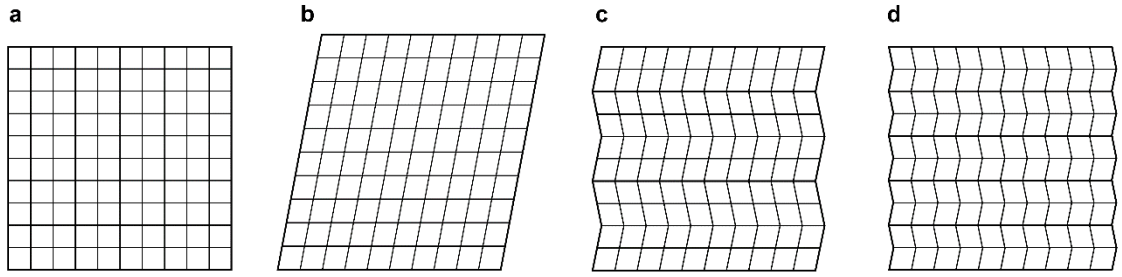

Figure 2: Schematic configuration of SMAs microstructure: a) austenite, b) oriented martensite, c-d) examples of self-accommodated martensite, inspired by [8].

2.3 Thermomechanical behaviors of SMAs due to martensitic transformation

The functional properties of SMAs are inherently thermomechanical in the sense that both temperature and mechanical loads drive the martensitic transformation and the SMA element responds by change of strain (stress). The schematic pyramid, shown in Fig. 3, outlines thermomechanical loading applied to SMAs. The change of stress and temperature driving the progress of the martensitic transformation in SMAs are mutually coupled [7-10,13-17]. The coupling is described by the Clausius-Clapeyron equation (Eq. 1):

$$\frac{d\sigma}{dT} = -\frac{\Delta S}{\varepsilon_{tr}} = -\frac{\Delta H}{T \cdot \varepsilon_{tr}}, \tag{1}$$

where σ is uniaxial applied stress, ε_{tr} - transformation strain, T - temperature, ΔS - the change of entropy of the transformation, and ΔH – the change of the enthalpy of the transformation. Since the entropy decreases with the transformation from austenite to martensite (ΔS is negative), the slope $d\sigma/dT$ is positive, i.e., the stress required to drive the martensitic transformation increases with increasing temperature [7]. Table 1 provides a detailed explanation of Fig. 3.

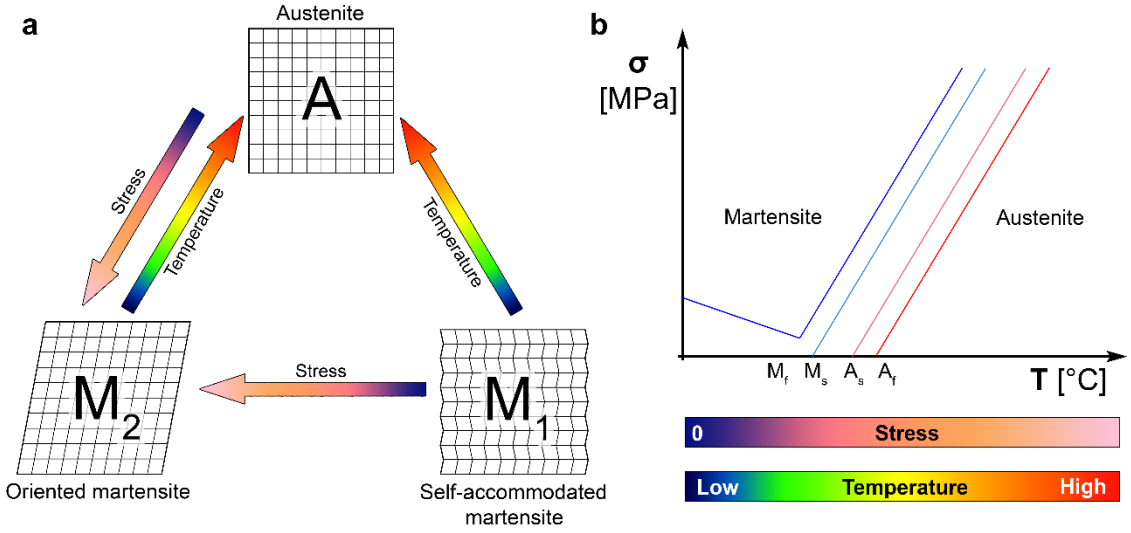

Figure 3: Schematic illustration of the paths of martensitic transformation based on the way stress and/or temperature is varied in a) and the schematic graph of Clausius-Clapeyron relationship, where martensite finish, martensite start, austenite start, and austenite finish are labeled as M_f, M_s, A_s, A_f, respectively.

Table 1: Reversible martensitic transformation in SMAs

Label	Name	Possible combinations of behavior
A	Austenite	$A \rightarrow M_1$ and $A \rightarrow M_2$
M_1	Self-accommodated martensite	$M_1 \rightarrow A$ and $M_1 \rightarrow M_2$
M_2	Oriented martensite	$M_2 \rightarrow A$

- A→M1: Upon stress-free cooling, the austenite transforms below the M_s temperature via thermally induced martensitic transformation into a self-accommodated microstructure of martensite variants.
- A→M2: If the external load is applied at a constant temperature, austenite transforms into oriented martensite, via stress-induced martensitic transformation.
- M1→A: Self-accommodated martensite can easily reversibly transform thermally back to the parent phase (austenite) by increasing temperature at small or stress-free conditions.
- M1→M2: Self-accommodated martensite can be converted into oriented martensite by applying stress in the martensite state by changing the orientation of martensite variants in favor of these giving the largest strain in the direction of the applied load via the deformation process called martensite reorientation.
- M2→A: The oriented martensite undergoes reverse martensitic transformation to the austenite on i) unloading and/or ii) heating.

2.4 NiTi shape memory alloys

The near-equiatomic NiTi alloys are unique among the already discovered SMAs. Many of the known SMA alloys are highly limited in their engineering applications, either due to a limited range of transformation temperatures or due to poor mechanical properties, such as maximal stress, crystallographic limits of strain, and availability in industrial polycrystalline form. In this respect, NiTi alloys (phase diagram in Fig. 4) display excellent mechanical strength, ductility, relatively large transformation strains (5-8 %), and high work output. The first engineering applications were developed 50 years ago, firstly by the military as cryogenic couplings of the tubing in the Grumman F-14 Tomcat aircraft in the 70s.

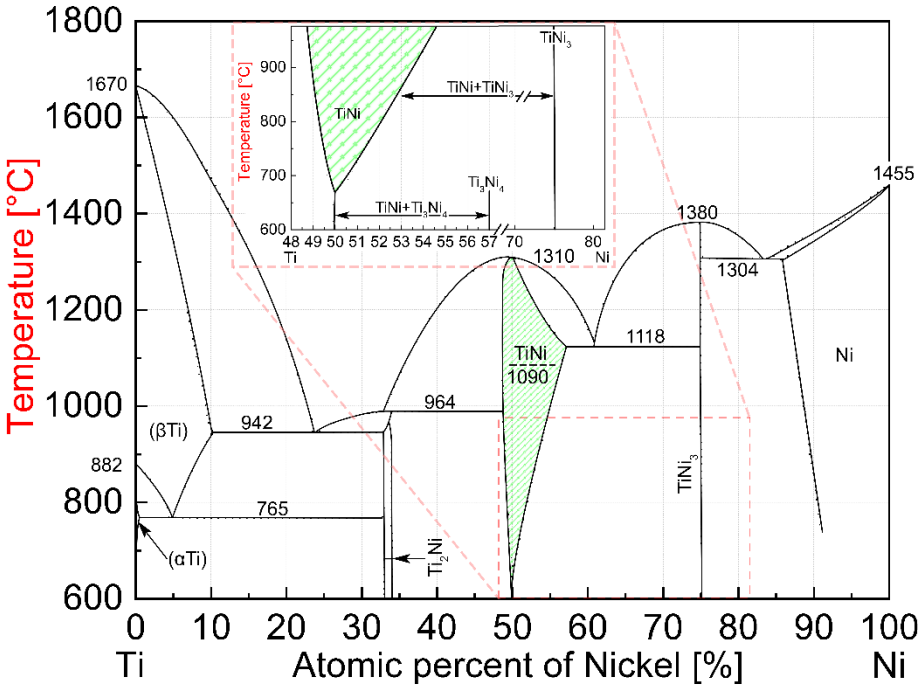

Figure 4: Adapted scheme of the phase diagram of Ni-Ti, where the composition window for binary Ni-Ti is highlighted with green hatching, also magnified detail shows the concentrations and temperature where the coherent Ni_4Ti_3 and incoherent Ni_3Ti precipitates can form, adopted from [9].

Due to the above-mentioned excellency in highlighted properties of NiTi SMAs, they provide the desired combination for many engineering, technological, and medical applications, so they are used in a wide variety of commercial smart design solutions. Moreover, the relative affordability of NiTi-based alloys, their great oxidation (passivation of TiO_2) properties in harsh environments, and biocompatibility, have made them even more utilized for their superelastic properties [26-29]. The engineering application using the SME is stably growing and catching up with the relatively simpler SE elements having easier application (i.e., due to the constant temperature).

On the other hand, SE can be also used for technical applications, such as special stand-alone newly developed and promising parts used for damping, in microdevices, as electrical connectors for a secure connection, or as refrigeration cycling elements (in elasto-caloric cooling devices).

Shape memory materials are becoming more popular for their usage as actuators, in thermal cycles for energy harvesting, in automotive and aeronautics as changing shapes of wings, facets, vents, helical springs (push/pull or valves), composite parts of wind turbine blades, textiles, etc. Moreover, SMAs are growing in popularity in robotics and remote-control parts, electromechanical systems, and other smart structures such as autofocus elements in small optics and a wide variety of positioners and simple actuators (Fig. 5) [1-6].

Figure 5: Examples of applications of the NiTi SMAs. From left top to bottom right: stents, endodontic files, bone staples, SE rims for glasses, rods for spiral spine scoliosis, braces, chevrons for noise reduction of a Boeing 787 Dreamliner, heat-activated stiffening elements, micro-optics for lens camera of smartphones, automatic valve, and coupling for pipe connection.

2.5 Crystallography of martensitic transformation in NiTi

The binary near-equiatomic NiTi alloys undergo martensitic transformation among three phases B2 cubic austenite, rhombohedral R-phase, and monoclinic B19' martensite.

The R-phase is an intermediate phase observed under special circumstances between the austenite and martensite phases (Fig. 7). B2-R transformation is characterized by a sharp increase of electrical resistivity with extremely small temperature hysteresis (1-3 °C). Transformation temperatures M_s, M_f, A_s, A_f, R_s, and R_f are conveniently determined using differential scanning calorimetry (DSC) measurement (Fig. 6). B2→R transformation is a competitor to the B2→B19' transformation and, if R-phase appears first, the transformation will proceed as B2→R→B19'. This transformation can occur in three cases:

1) in Ni-rich alloys by precipitation of Ni_4Ti_3 phase, 2) residual stress field present after heat-treatment of cold-worked material, 3) when some % of Ni is substituted by Fe or Al [7].

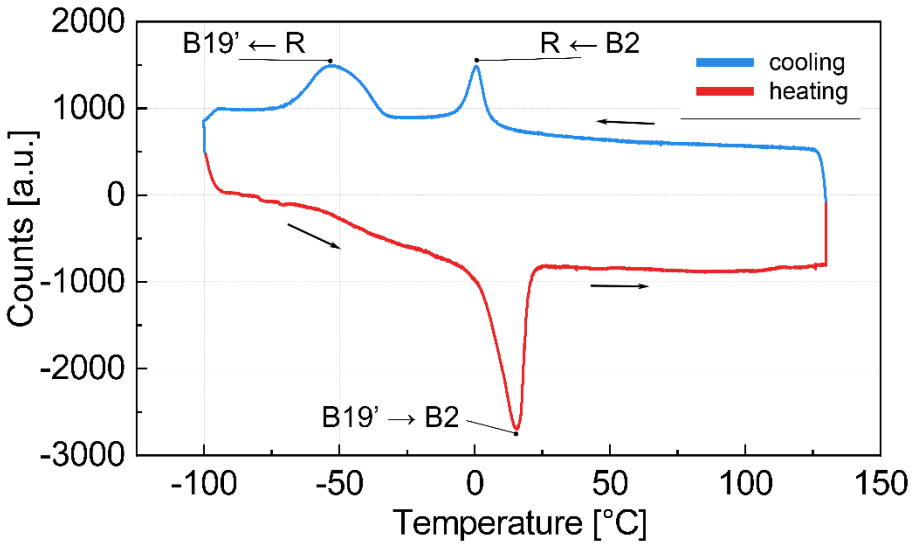

Figure 6: Stress-free differential scanning calorimetry of a NiTinol exhibiting all three phases: B2- Austenite, B19'- Martensite, and rhombohedral- R-phase.

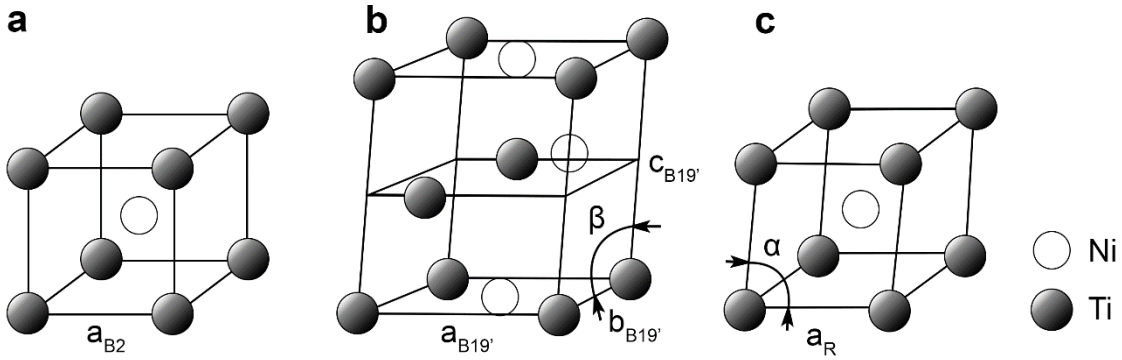

Figure 7: The binary NiTi alloy crystal structures. a) Parent cubic austenite (A) B2 structure, b) daughter monoclinic martensite (M) B19' structure, and c) rhombohedral R-phase, adopted from [6,25].

2.6 Strain localization in thermomechanical loading of NiTi

Systematic experimental investigations have been carried out since 1970 to understand deformation mechanisms in NiTi SMAs derived from martensitic transformation. These works include the investigation of localized deformation via propagation of Lüders-like deformation bands in tension. Recently, it was found that localized deformation of NiTi occurs in various deformation modes (uniaxial tensile, torsion, compressive, or combined loading) [37,39-47].

An early experimental result shown in Fig. 8 represents one tensile loading and unloading of SE NiTi (SE cycle) of the wire with a diameter of 1.07 mm at a quite low strain rate [38]. As it is shown in Fig. 8a, four extensometers (E1-4) were used in one sample while the local evolution upon loading for each extensometer is shown in Fig. 8b.

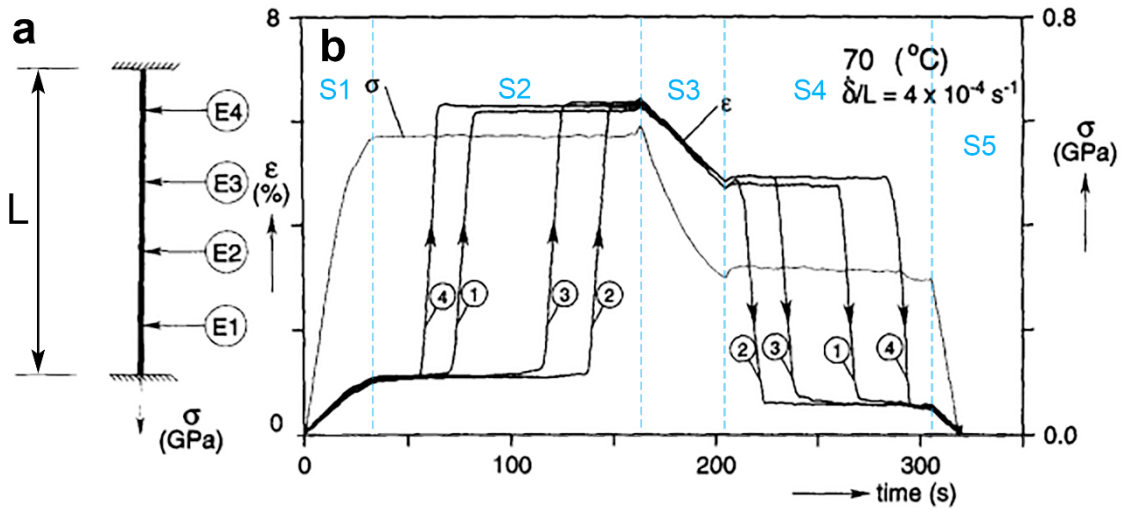

Figure 8: Simple scheme of measurement using few extensometers in a), The full Stress-time and localized strain-time responses corresponding to the extensometers in a) [38].

To understand the details of the process, the loading and unloading are separated into five stages (S1-5):

- S1 represents a linear increase of stress and strain and corresponds to the elastically loaded austenite phase, therefore all responses of the individual extensometers are uniform.
- S2 corresponds to nucleation of the martensite phase; the different parts of the wire do not transform simultaneously – this is reflected in different responses of the extensometers, forming plateaus from about 1 to 6.2 % of strain.
- S3 demonstrates that the sample, elastically unloaded to about 5 % of strain, consists of stress-induced martensite.
- S4 shows that reverse transformation takes place at different times similarly as in the case of forward transformation but proceeds at a lower value of the stress.
- S5 corresponds to the elastic unloading of the austenite phase.

Since early observations of such localized deformation, several methods for observing the localization phenomena in NiTi alloys have been successfully utilized:

- **Multiple extensometers:** as shown in Fig. 8, more extensometers redistributed the specimen length have been used on larger samples and utilized in earlier studies [31,38-39].
- **Surface coatings or oxide fracturing:** Methods utilizing either an inelastic coating or natural TiO_2 oxide, which is commonly present on the surface of NiTi. The large strain of MT gives the possibility of tracking the change of reflection of

such cracked surfaces. However, it is usually harder to be qualitatively utilized as the cyclic instability changes its nature [30,39-40].

- **Changing reflection of light and/or Nomarski contrast:** it is possible and relatively easy to be used on polished samples (especially for single crystals or large grains) to observe the localization of MT [34,39-40,47].
- **Profilometer:** Since the MT occurs without volume change the longitudinal strain variation will reduce the thickness of the sample, therefore, a relatively large change in the profile is present as shown in Fig. 9a [37].
- **Thermometry:** The MT is highly exothermic, the localization of deformation will produce also localized heat sources, which are released during phase transformation and its propagation. Therefore, the observation of the temperature changes during forward and reverse transformation is carried out as it is represented in Fig. 9b. However, it needs to be pointed out that heat diffusion is highly affected by sample properties and equipment capabilities [39-40,48-49].
- **Digital image correlation:** Applying either random or ultra-precise patterns on the surface and measuring the displacement and strain fields by digital image correlation (DIC) provided valuable information in the field of NiTi SMAs as well [38-39,43,46,50-54].
- **X-Ray or Neutron diffraction (beam scanning) techniques** for the observation of localized deformation in SMAs: An example of synchrotron study on a helical spring and the visualization of redistribution of the phases are presented in Fig. 9c. Another example illustrating a such method of scanning of the Lüders band on loaded SE NiTi wire in tension was reported in [55-56].
- **Scanning electron microscopy (SEM)** utilizing a combination of secondary electrons with the electron back-scattered diffraction (EBSD & 3D EBSD) and electron dispersive spectroscopy (EDS) as shown in Fig. 9d, is an excellent method for analysis of localization phenomena on the mesoscale of individual polycrystal grains. Combination of techniques such as EBSD and nanoindentation hardness mapping as shown in Fig. 9e.
- **Transmission electron microscopy (TEM)** is a key method for the detailed analysis of lattice defects created by the MT on the meso- and micro-scales [57-60].

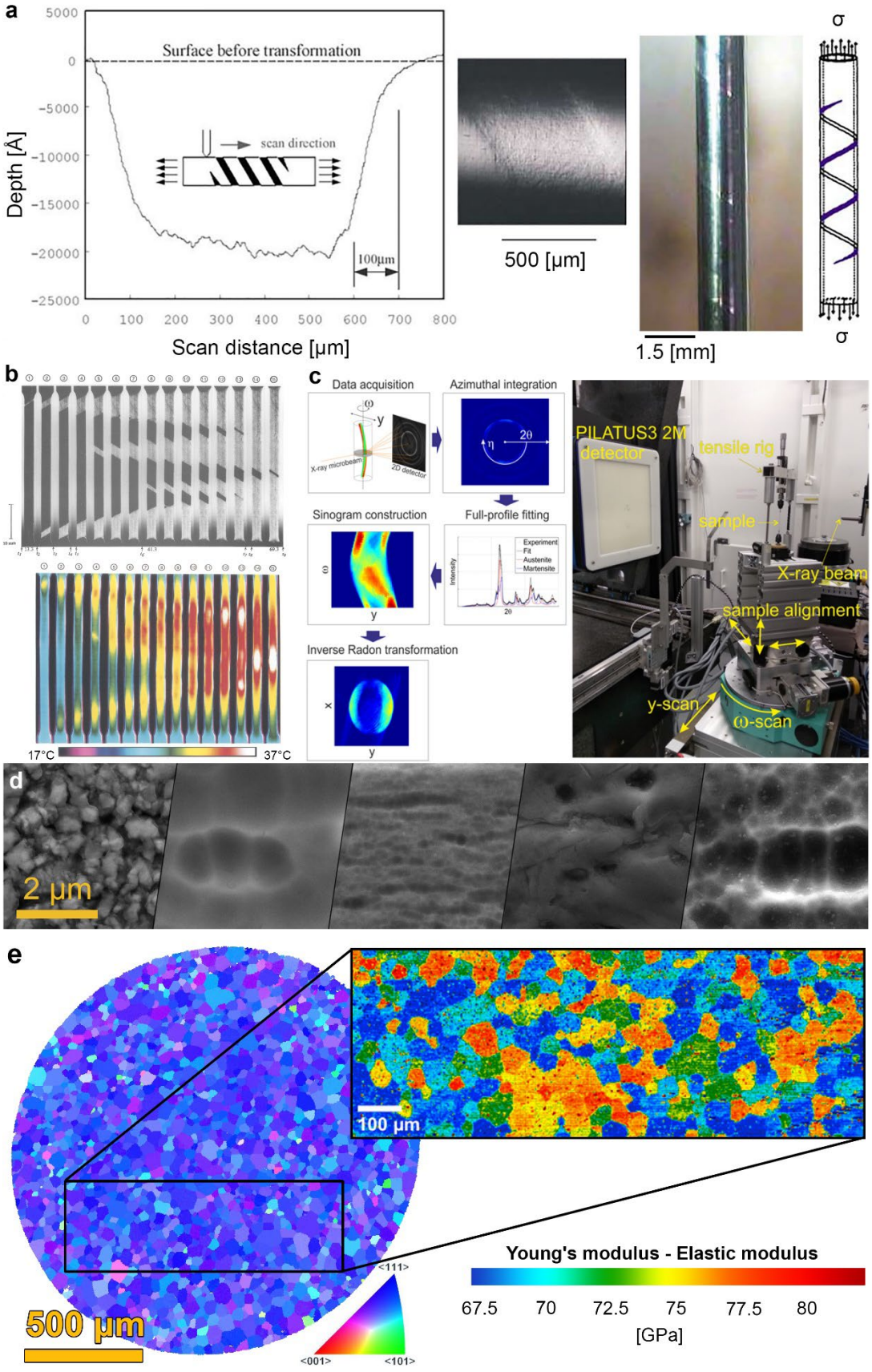

Figure 9: Schematic examples of different measurements of stress-induced localization on NiTi micro bars in a), local strain and corresponding thermal response on strip dog-bone in b), 3D reconstruction of redistribution of phases in helical spring in c) [37,39,56], different surface treatments of NiTi affecting the localization on microscale observed in SEM in d) and EBSD map in comparison with nanoindentation hardness mapping in d).

2.7 Fatigue of NiTi shape memory alloys

Improvement of fatigue performance of NiTi so that cyclic thermomechanical loading can be performed on commercial bulk NiTi elements with large reversible strain (~5 %) under high stresses (500 MPa) for a large number of cycles (10^5-10^6) belongs among key targets of current NiTi research. If solved, new perspectives will be opened for NiTi technologies in several areas such as actuation, elastocalorics, seismic protection, etc. There exists already a notable amount of references regarding the ways allowing to control and optimize the properties of NiTi for specific applications. The last few decades benefitted from fundamental and application-related research, resulting in a better understanding of mechanical and microstructural aspects regarding the functional behavior of SMAs [12-20]. However, fatigue still tends to limit the performance, service, and design of shape memory components. As a result, the origins, and the presence of both structural and functional fatigue of SMAs are still being investigated [16-18,20,55,60-64].

On the one side, structural fatigue tends to refer to the fatigue of SMAs around the nucleation and growth of cracks during cycling loading emerging from surface or subsurface defects and leading to fatigue failure. On the other side, the functional fatigue origins from the clear degradation of some functional properties (i.e., plateau stress, recoverable strain, hysteresis width, transformation temperatures, the stroke of the actuator during the fixed heating-cooling cycle, or their combination), for instance, large irrecoverable strains and disappearance of the plateau stress caused by irreversible microstructural changes.

2.7.1 Structural fatigue of NiTi shape memory alloys

Investigation of the structural fatigue in NiTi SMAs is motivated by the goal of achieving better cyclic performance of NiTi members in existing engineering applications. This is of particular importance in the case of medical implants [16-17,20,65-66]. As a representative example, one can consider fatigue of braided or laser cut stents as implants for blood vessels in the human body, which are exposed to cyclic fatigue. Such stents should be in service at least for 10 years, and during that time they are required to sustain the integrity of the whole structure and thus with numbers of cycles exceeding 10^8. Another kind of example from the medical field is endodontic files for extensive root canal treatments, which are used similarly as drills. Either manually or

mechanically driven, they are used for cleaning and shaping the root canals, which often have various deformities, sharp angles, and mechanical obstructions. At first look, such a comparison of the above-mentioned cases could seem unfair, however, both cases can in some circumstances fail similarly, i.e., a fatigue crack propagation. The thermomechanical conditions of loading and unloading split the life paths between low-cycle fatigue and high-cycle fatigue regimes (LCF and HCF) [18,62,67-70]. In the HCF regime, the crack initiation and propagation are significantly delayed and tightly controlled by the microstructural processes leading to the nucleation and propagation of the cracks. On the other hand, in the LCF regime, the cracks nucleate rather fast, thus, fatigue life is mainly controlled by the capability of the material to shield itself from propagating of fatigue cracks. It is commonly reported that the nucleation of cracks originates at the surface. The initiation of the surface cracks is affected by the type and quality of the surface. The existence of surface defects like scratches, notches, and die drawing marks, is therefore also in the spotlight. Such defects can act as local stress concentrators, thus shifting the applied stresses on micro levels and leading to the accelerated formation of fatigue cracks. However, in the absence of surface or sub-surface microcracks, the formation of fatigue cracks localizes preferably at the carbide or oxide inclusions, which are always present in the volumes in some amounts corresponding to the purity of raw materials, the methods of ingot manufacturing and the profile manufacturing. Various attempts have been made to improve surface parameters, by reducing the surface polishing (i.e., mechanical, electropolishing), introducing compressive stresses in surface regions [65,71,72], or reducing the volume, size, or chemistry of impurities [28,74]. The propagation of cracks in SE SMAs is different from the conventional engineering materials due to the different material responses to the local stresses in front of the crack tip. The reversible stress-induced martensitic transformation allows the material to deform significantly at relatively low stress without damaging the crystal lattice surrounding the crack tip [74,75]. This slows down the crack propagation rate of NiTi with respect to the conventional elastoplastic materials deformed with the same strain amplitude, which deform plastically in front of the advancing crack tip.

Meanwhile, structural fatigue follows regular stages well-known from the structural engineering materials. (1) crack initiation, (2) crack propagation, and (3) fast macroscopic growth and fracture [76,77]. It has been shown in literature, that NiTi SMAs cycled in the SE regime are prone to inducing cracks with ease and in large densities at various loading conditions [9,16,17,56]. However, the effects of localized deformation on the inducing of

MT and vice versa are important, and its effect on the slow propagation of the crack in the earlier stages is paid surprisingly reduced attention.

2.7.2 Functional fatigue of NiTi shape memory alloys

In the vast majority of SMAs, functional fatigue is caused by the accumulation of defects created during phase transformation or overstressing of the microstructure [78,79]. The continuous degradation created by cyclic transformation can occur generally in SMAs upon thermal cycling, thermal cycling under stress, and mechanical SE cycling. The connection of irreversible transformation in relation to microstructural changes resulting in functional fatigue was already observed in the early 1970s [80]. Based on the results of transmission electron microscopy for tracking the dislocations and defects accumulated during cycling in NiTi SMAs, one can suggest that these defects might provide a block in the form of residual stresses, which might support or suppress recovery processes. In general, defects created during cyclic martensitic transformation are formed in order to obtain the necessary compensation for the crystallographic misfit between austenite and martensite [20,81-84]. Lattice defects created by martensitic transformation fronts propagating back and forward affect the sub-sequential cycles, and phase transformation behavior in some particular way. It seems, that these defects can cause of stabilization of martensite [85-87]. Recently, a system of irreversible defects created via coordinated slip or twinning creating the newly oriented microstructure was proposed ($B2 \rightarrow B19' \rightarrow B2^{T}$), which plays a large role as a mechanism leading to functional fatigue [20,61]. Such change in stability of the structure leads to degradation (i.e., ratcheting and elongating) while being cycled in actuator cycling. Moreover, a decrease in hysteresis occurs during each cycle. Therefore, the experimental data provided for alloying of NiTi structure for instance with Cu exhibit better stability of such behavior, and thus one can expect better compatibility between the crystal lattices of martensite and austenite [25,88]. Thus, fewer defects are produced and accumulated in the microstructure during sub-sequential transformation cycling, while assuming that the crystallographic compatibility plays a role in either stress-free cycling or cycling with applied stress [89].

Tuning the parameters for better crystallographic compatibility is by far not the only option to reduce functional fatigue. Two major groups of state-of-the-art are highlighting different ways which can be applied:

- Smoothening of transformation processes to reduce the irreversibility of transformation by changing the crystallography parameters, as discussed above.

- Stronger SMAs in order to create fatigue resistance by creating microstructure more resistive to plastic deformation [58,90,91]. Another possibility is particle strengthening using precipitation of either binary or alloyed NiTi- based systems [87,92]. A third option, which might be included in this category is the intentional introduction of residual stresses to the structure by ion-implantation, shot peening, laser shock peening, or sand-blasting [93-95].

2.7.3 Coupling of structural and functional fatigue of SMAs

Despite the clear differentiation between structural and functional fatigue, the processes are not simple to distinguish in the practice [9,55,65,96]. Numerous studies have reported how applied stress affects the number of cycles until failure during actuator cycling. Similarly, higher temperature affects the stress plateau value in stress-induced transformation during SE cycling [17]. Nowadays, the mechanisms of the majority of the crack's lifetime are still not completely clear, even if there are numerous studies, proving the existence of a large density of short cracks propagating perpendicularly to the loading direction in tension. There has been suggested that cycling results in an increase in surface roughness, which might cause the initiation and early propagation of the cracks [9,97]. Nevertheless, additional work is required to analyze how and in which way the incompatibilities of the martensite and austenite lattices are about to be addressed as the cause of the irreversibility of the martensitic transformation and the degree of coupling between the functional and structural fatigue of SMAs.

3 Materials and methods

Various samples of nearly equiatomic NiTi Shape Memory Alloys are studied in this work. Samples have different geometries such as rods, thin and thick wires, ribbons, and sheets with different cold work and heat treatments, which allowed us to study a variety of samples exhibiting transformation behavior under different conditions. The large variety of sample conditions was selected for numerous reasons, such as grain size, the density of defects, stability of the material properties upon cycling, and the ability to process the multiscale studies (i.e., fully annealed microstructures and larger grains). One of the studies used the snake-shaped springs for simulating stent-like combined deformation in a reproducible manner. Some sample shapes used for the different studies are presented in Fig. 10, however, for better clarity and easier understanding the largest effort was focused on studies of polycrystalline NiTi SMA wires.

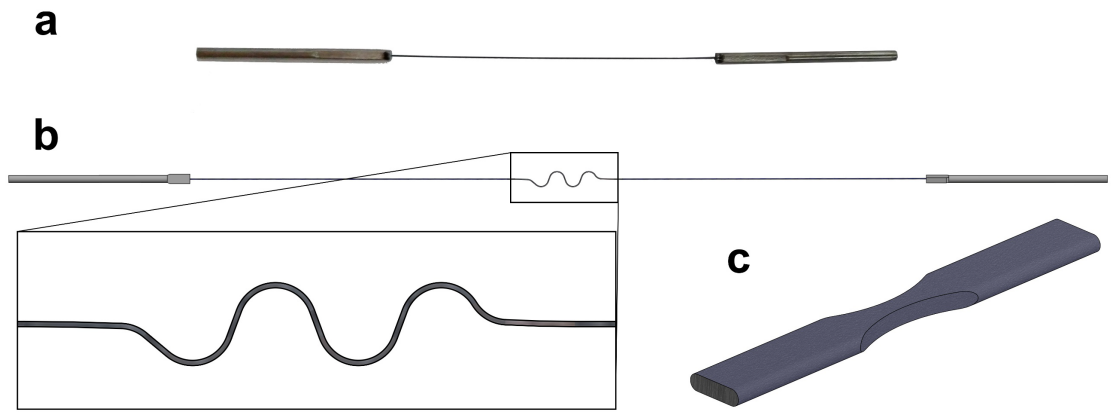

Figure 10: Examples of NiTi samples used in the study. a) NiTi wire sample with a diameter of 100 µm clamped in stainless steel capillary, snake-like spring created by shape setting of the wire using specific fixtures in b) and dog-bone shape sample created either from ribbon or rod in c).

Most of the studies were performed using 100 and 200 µm NiTi wires in diameter. The composition range of binary near-equiatomic NiTi with SMA properties is narrow as shown in the phase diagram in Fig. 4. Within the window, the composition ratio of Ni-Ti affects mainly the transformation temperatures, in such a way, that for the so-called Ti-rich samples (S02) the transformation temperatures are higher than in the opposite case Ni-rich (S01) as listed in Table 2.

Table 2: Table of original sample geometries with description

Nr. [-]	Name [-]	Composition [at. %]	Dimensions [mm]	As received [-]	Manufacturer [-]
S01	NiTi#1	50.97 Ni 49.03 Ti	wire 0.2; 0.1	38 % CW	Fort Wayne Metals
S02	Flexinol	49.9 Ni 50.1 Ti	wire 0.2	annealed	Dynalloy
S03	NiTi bar	51.1 Ni 48.9 Ti	rod 12.7	Hot rolled	SAES Smart Materials
S04	NiTi sheet	51 Ni 49 Ti	0.1	flat annealed	SAES Smart Materials

Even the basic characterization of SMAs can be relatively problematic due to several factors. Even such a simple task as clamping of samples for tensile testing can be problematic for SMAs as during clamping the transformation might be only partially finished and when more stress is applied, the sample can easily slip. As it was discussed in details above, the SMA behavior is highly affected by temperature. In our study, we try to deal with both problems with the highest priority and minimize any effects, specifically by using either stainless-steel capillaries for wires, dog-bone, or hour-glass shaped samples and by the usage of in-house designed temperature chambers allowing the precise temperature control in a relatively wide range (from -170 °C to about 600 °C). The Peltier's chamber for mid-range (-30 to 200 °C) or resistive elements for high temperatures (above 200 °C) and the liquid nitrogen for temperatures below -30 °C.

The basic characterization was performed using two differential scanning calorimeters (DSC) machines (Linkam DSC 600 and TA DSC 25). These machines were used to determine the temperatures of the martensitic transformation, the sample was subjected to heating and cooling in the temperature range from +120 to -150 °C with a cooling rate of 3 °C min^{-1} and 1 °C min^{-1}.

For the macroscopic measurements, we utilized the machines UTTRMO, MITTER, and FATTER (horizontal testing machines with close-loop Ni-cRIO and LabView programming). These three, in-house designed and build machines have been specifically designed for testing small samples, with a precise position of magnetic sensors of (± 10 μm/m) with various load cells ranging from 10 N, 440 N up to 5 kN on UTTRMO. Originally used for better precision of the strain measurements, the stainless-steel capillaries help to define the initial length. For larger samples, the electro-dynamic tension-torsion INSTRON Electropuls E10000 was used. For most measurements we took advantage of relatively large changes in resistivity difference between all phases

(i.e., austenite, martensite, R-phase) and thus in-situ measurement of resistance is implemented.

The thermomechanical processing of NiTi is one of the major parts of acquiring the SME. Thus, while we did not focus on cold-working or manufacturing the samples from ingots or pellets, the heat-treatment of the NiTi samples was a crucial step in sample preparation. Several annealing methods were used for NiTi processing: annealing in a conventional air furnace, pulse heat treatment by electric current, or furnaces either filled with inert gas or sealing the samples in the quartz to minimalize any oxidation at high temperatures. It should be taken into account, that there is a high probability to expect the growth of Ni_4Ti_3 coherent precipitates at relatively low temperatures ($\geq$ 400 °C) and the possible growth of thicker TiO_2 oxide layers, which might affect the results, especially in connection to the presence of R-phase transformation or influence of the surface quality on the fatigue.

Furthermore, a detailed description of the other methods and techniques will be provided separately in the subsections of each case study for better clarity.

3.1 Experimental setup of tensile testing

As it is shown in the corresponding scheme of the basic layout in Fig. 11a, the sample was mounted in the horizontal testing machine with the initial length L_0 defined by the samples mounted to the jaws using stainless steel capillaries. Both sides of grips are water-cooled, mainly due to the force shift of a load-cell mounted on one side, but also in order to limit the thermal expansion of the jaws, which plays a large role, especially during high-temperature measurements. Moreover, the jaws are electrically insulated from the machine in order to avoid any noise during resistance measurements. The systems are designed in such a way that only one side is movable while the other part is fixed. The cross-head displacement is tracked, while the axial force is recorded during the test. Then the engineering stress ($\sigma_0 = F/S_0$) and engineering strain $\varepsilon_0 = \Delta L / L_0$ can be evaluated.

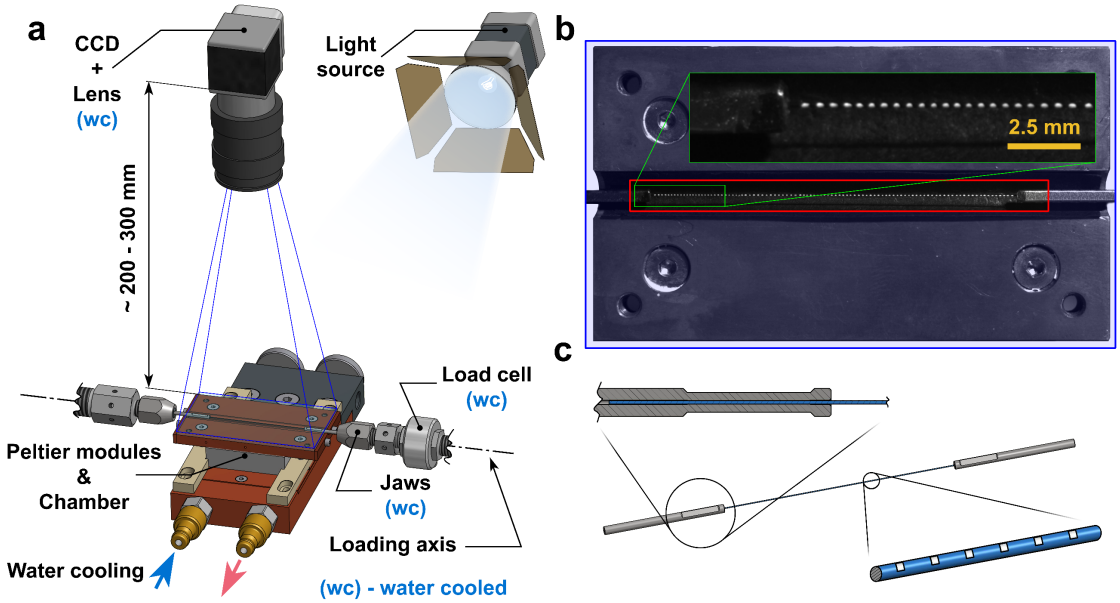

Figure 11: Schematic of the in-house designed UTTRMO testing machine with tensile testing sample environment and DIC setup (a-b) and sample crimped to the capillaries with the dotted pattern for tracking of local strain in c).

Depending on the type of experiment, the real local strain displacement was acquired by the optical measurements, in addition to the strain provided from the displacement of the cross-head used instead of the extensometer due to the diameter of samples (50 μm). The typical engineering stress-strain curves for the NiTi loaded in tension at a temperature above A_f (Fig. 12a) and below M_f (Fig. 12b) are shown in Fig. 12. It is worth to mentioning that when a sample is loaded and unloaded at low temperature ($T<M_f$ as shown in Fig. 12b), and then heated above A_f the strain would be recovered close to 0 %. The DIC method allows to evaluate the displacements at the beginning of a test, deformation of the tensile machine or gripping system, pointing out possible sliding of the sample from the capillaries or jaws (grips) or more importantly to observe any localized deformation within the resolution capabilities of the particular setup.

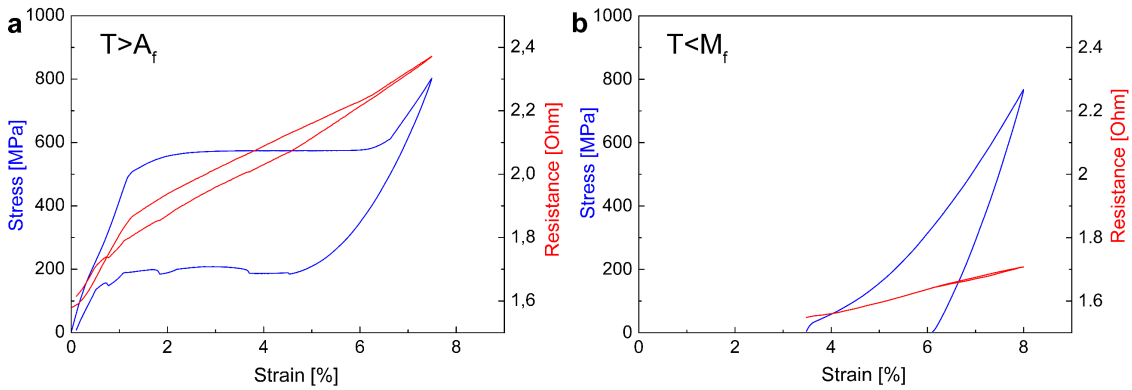

Figure 12: Stress-strain response upon loading and unloading of NiTi at the temperature above A_f (superelastic cycling) and below M_f (martensite reorientation) in a) and b), respectively.

3.2 Tracking of the localized deformation in NiTi

The analysis of the local strain field can qualitatively help to characterize the heterogeneity of the strain field during the loading and unloading of SE NiTi samples, and/or thermally cycled SM samples in an actuator regime usually loaded at constant stress. An example of the localization of deformation in the dog-bone-shaped flat sample of SE NiTi wire electro-discharge machined and polished from a round bar listed in Table 2 as S03 (Fig. 13a) during one full SE cycle at 25 °C is presented in Fig. 13b. Due to the synchronization of strain field measurements and the data acquired via the testing rigs (force, displacement, resistance) in time, we can connect every marked point on the curve to the corresponding recalculated strain field pattern. The advantage of using the DIC method is in the possible distinction of redistribution of strain fields in direction of elongation, contraction, and shear strains (i.e., ε_{YY}, ε_{XX} and ε_{XY}, respectively). We highlighted eleven separate time stamps corresponding to different places on the macroscopic stress-strain curve (Fig. 13b) during loading and unloading and plotted the ε_{YY} strain field maps in Fig. 13c, which corresponds to the direction of the applied force in tension.

The main parts of the superelastic loading and unloading can be then described as follows: elastic loading of austenite (1-2), stress-induced nucleation of Lüders bands (2-4), propagation of Lüders bands (4-6), the merging of the Lüders bands (6-7), elastic unloading of martensite until the Lüders bands nucleate in the martensite phase and propagates to transform the martensite back to austenite on the reverse plateau (7-8), reverse propagation of the Lüders bands till their merging fully back to the austenite (8-10), elastic unloading of austenite (10-11). The nucleation and propagation of Lüders bands are driven by the shear stress, there exists a critical value for the nucleation of Lüders bands.

The martensite band front separates the highly deformed martensite band (5-10 % axial strain component) from the yet undeformed austenite part of the sample (~1 % axial strain component). Since the macroscale deformation has to be compatible at such a moving macroscopic interface, the Lüders bands take a form of a plate inclined 56° to the loading axis in the case of a thin ribbon (Fig. 13 c-d). The local shear strains along the gauge length serve to highlight the geometry of the transformation band (Fig. 13e). The local shear strain at the Lüders band front leads to kinking (~ 1-2°) of the gauge length as the magnitude of the moment increases. The martensitic transformation proceeds (and

strain changes) only within the moving Lüders bands. In theory, the forward and reverse transformations within the moving Lüders bands may take place during the mechanical cycling without generating lattice defects. As the moving Lüders bands propagate, they generate residual strain by the accumulation of lattice defects.

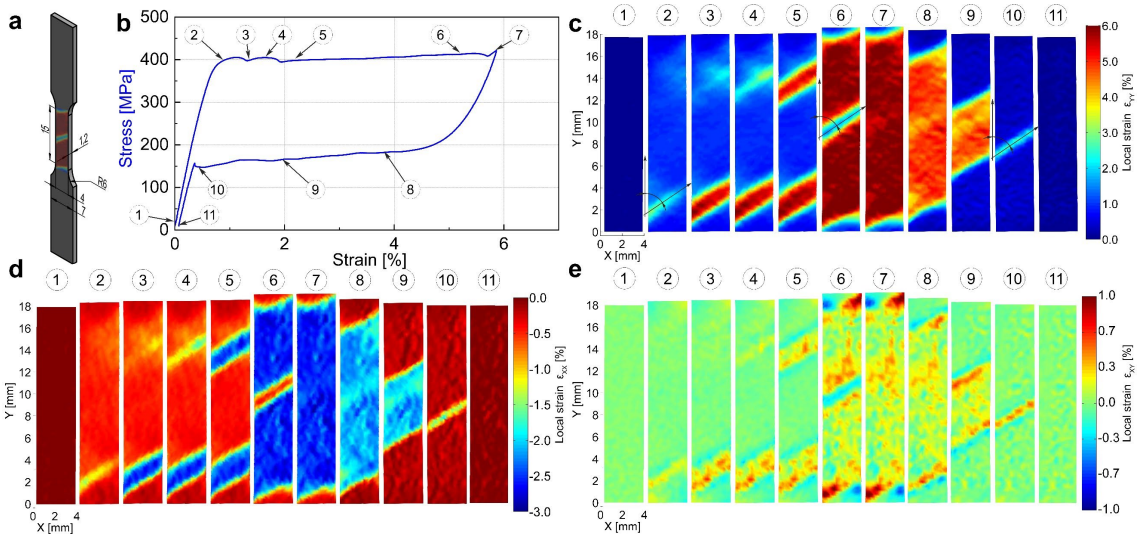

Figure 13: Tensile loading and unloading of SE NiTi flat dog-bone sample a), macroscopic stress-strain curve till the end of the transformation plateau and unloading in b) and corresponding strain field DIC patterns in direction of the loading axis (axial strain, ε_{YY}) in c), strain field DIC patterns in the radial direction (contraction, ε_{XX}) in d), and strain field DIC patterns of shear strain, ε_{XY} in e).

A similar interface to the Lüders bands in flat samples is expected to be formed in the structure with a round wire or rod axis. However, due to the symmetry in one internal axis, a symmetrically rotated interface an hour-glass like interface is formed instead of a tilted interface. Recently, such a heterogeneous 3D interface was studied in detail by micro beam on the synchrotron, providing grain-by-grain information of the redistribution of phases and sub-sequential calculation of internal strains and stresses [55].

In the case of samples, which are commonly significantly longer and thinner, it is possible to neglect the real macroscopic shape of the interface for tracking any localized deformation. This huge size effect allows to use of one-dimensionality of the strain values and thus significantly simplify the computation time and utilize the DIC even for long-term experimental procedures, unlike the "full field" methods. A single-axis measurement, which we call a 1D-DIC method was successfully utilized even in combination with thin wires (as thin as 30 µm in diameter), using either homogenously spaced marks or random spackle patterns. During all experiments, the camera facing the pattern on the surface was pointed on the special in-house designed furnace with a relatively thin window from Simax/Pyrex glass with relatively high thermal conductivity

to assure precise thermal control of the wire surroundings. By the DIC software, the acquired images were converted into strain control maps informing about the evolution of the local axial strain component along the wire length in the space-time coordinates. An exemplary scheme of such tracking is provided in Fig. 14, in this case representing the SE cycle of NiTi wire with 200 µm in diameter.

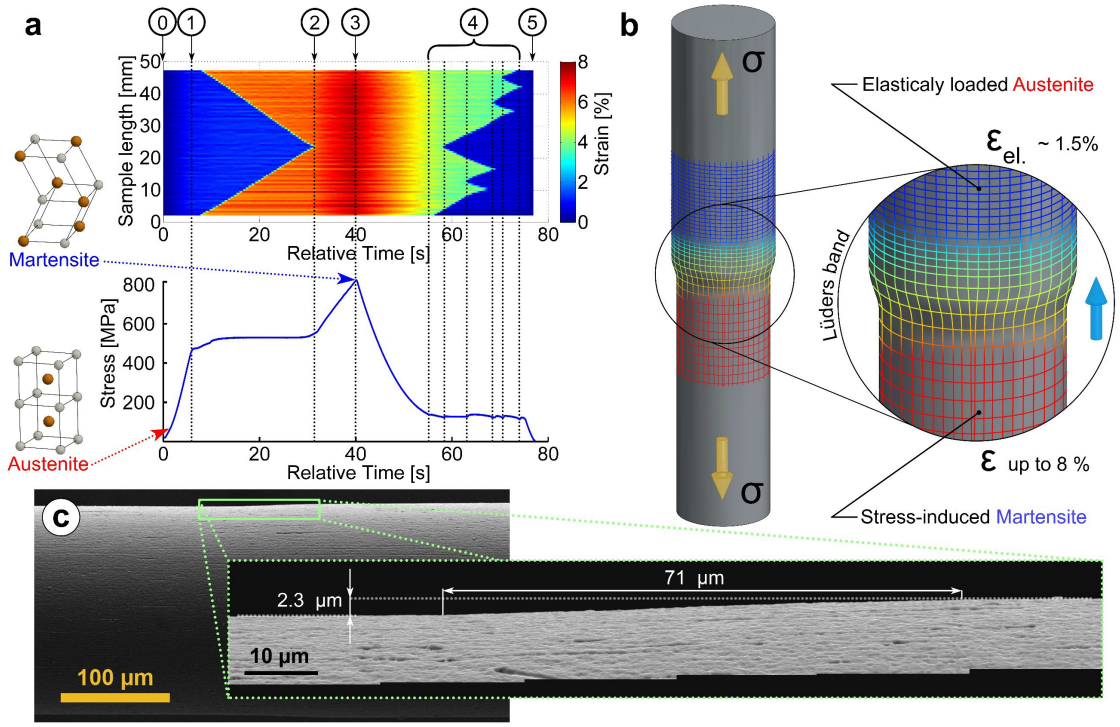

Figure 14: Schematic picture of the 1D-DIC method used for tracking of localization in thin NiTi wires in a), Scheme of the localized deformation in the Lüders bands on wires in b), and in-situ microscopic detail of the Lüders band interface geometry on the 200 µm wire in c).

Fig. 14a shows the 1D-DIC strain patterns plotted relative to time, where the cycle is again divided into sections from 0 to 5, and their description would be as follows: (0-1) elastic loading of austenite, (1) nucleation of Lüders bands at each end where the wire was already crimped and thus stress-induced in the martensite inside the capillary, (1-2) propagation of Lüders bands, (2) merging of the bands, (2-3) elastic loading in martensite, (3-4) unloading of martensite, (4) nucleation of Lüders bands during reverse transformation and finally (4-5) elastic unloading of martensite. Fig. 14b-c shows the propagating Lüders band observed by SEM.

3.2.1 Digital Image Correlation

Digital image correlation (DIC) is originally an optical contactless deformation measurement method that allows using recorded images and recalculates the displacement of the objects on the surface of a sample gauge length by correlating a

reference image with a sequence of images acquired during deformation [38,43,50-54]. Prior to the mechanical testing, a pattern (dots, lines, or speckles) is created on the sample gauge length. By computing the displacement in between the patterns during loading/unloading, it is possible to study the pattern evolution and calculate the surface strain field within the computed area using a DIC algorithm. DIC methodology can be applied on a different scale level: macroscopic level (over the entire sample gauge length) or on the microscopic level (using either small particles or surface features in micrographs).

In the present work, Mercury RT Realtime software for strain measurement UI and in-house Matlab scripts was used to compute macroscopic local engineering strain. The method is based on identifying the grid locations in a square pattern along the gauge length for the first (reference) image and then the calculation of their displacements in the following figures. Each frame has then a specific redistribution of the local axial strains along the computed area. The data was then correlated with the macroscopic engineering stress-strain data obtained from the stress rig (magnetic, optic measurement of the movement of the cross-head).

Furthermore, for thin and long samples we frequently utilize for thin and long samples the 1D-DIC technique, which uses the same method but then for representation of the specific loading stage (at specific time during test), just one line of pixels (representing local strains) might reduce the complexity of the common 2D maps. Moreover, especially in our case and often studied large deformation, this technique proves as a very useful tool for qualitative analysis of the evolution of the local strain.

Generally, the DIC method tracking the displacement of the speckle pattern consists of (i) determining the grids and facets based on the resolution and quality of the pattern, (ii) then selecting one of the points with defined surrounding. Each grid point defines the center of the squared region in the reference image. These points and their surroundings is tracked and used for calculation of displacement by the image correlation algorithm. This algorithm uses the facets to calculate the three-dimensional position and tangential plane of the speckled object surface for each point in the grid.

3.3 Microstructure characterization

3.3.1 Optical microscopy

For metallographic examination, the assessment of the surface quality and the first observation of the machining, grinding, polishing, and or etching (Kroll's regent: hydrofluoric acid 4.5 %, nitric acid 9 %, demi water 86 %) the optical observation and optical micrographs were taken on a ZEISS Axio Imager, Keyence VHX-1000 and Keyence VHX-7000.

3.3.2 Scanning electron microscopy

Scanning electron microscopy enabled inspection, testing, and other experimental techniques such as electron back-scattering diffraction (EBSD).

In order to observe the microstructure and microstructure changes caused by plastic deformation during monotonic or cyclic loading, the TEM lamellas were cut from the sub-surface layer parallel to the wire axis by focused ion milling (FIB) using FEI Quanta 3D FEG microscope with a Ga ion source. Other in-situ macroscopic testing and observations were performed using the TESCAN FERA3 GM microscope with a larger vacuum chamber.

EBSD enables determining of local texture, individual grain orientations, pixel-to-pixel orientation correlations, and phase distribution and identification near the surface of the samples (in our case bulk of polycrystals). In the area of interest, the morphology of microstructure is characterized in detail by the orientation contrast in the back-scattering electron images. The EBSD was performed using a TESCAN FERA3 GM microscope operating at 30 kV, with a large working distance of ~ 28 mm due to the experimental setup with DEBEN In-situ Microtest testing stage with the synchronous movement of both grips and EDAX DigiView 5 high-resolution digital camera and electron beam at conditions of 30 kV, ~ 4.86 nA of the probe current. The scanned area size, step size, and acquisition time all need to be considered for the grain size conditions.

The post-processing of EBSD maps was done using OIM Analysis 8.6 software suite. The maps were cleaned by removing random data spikes, and thresholding the band contrast by NPAR analysis. The B2 and B19' phases were identified. For most calculations, a minimum area of 8 pixels was used to identify subgrain/grain structures and as a critical value for misorientation of 2° was used for grain reconstruction. Higher

misorientations can be classified as low-angle boundaries and high-angle boundaries between > 2° to 15° and above 15°, respectively. The Kernel Average Misorientation (KAM) then can qualitatively describe the intergranular heterogeneity of plastic deformation and be correlated to geometrically necessary dislocation activity. While the average misorientation between a local pixel and its neighbors is within the range of critical subgrain angle and describes the local intergranular misorientation. The average of these misorientations can be expressed by the (Eq. 2).

$$KAM_{P_x} = \frac{1}{N}\sum_{k=1}^{N} \Delta\theta_{xk}, \quad (2)$$

where, KAM_x is the KAM value at pixel x, $\Delta\theta_{xk}$ is the misorientation angle between pixels x and k, N is the number of surrounding pixels that have misorientation with pixel x is within a critical sub-grain angle.

3.3.3 Transmission electron microscopy

TEM was used for a detailed examination of the microstructure from micro- to nano- scale. The samples in the form of the lamellae cut by FIB-SEM were observed at 200 KeV using the double tilt sample holder in an FEI Tecnai TF20 X-twin transmission electron microscope equipped with a field emission gun.

4 NiTi wires used in experiments

NiTi wires of different chemical compositions (Table 2), diameter and cold work/ heat treatment were used in experiments. The SE NiTi #1 wires (Table 2) manufactured for the production of medical devices display quite a large amount of impurities, as it is shown in EDS in Fig. 15b-c. While the presence of nonmetallic inclusions in NiTi wires is common, the size and volume fraction of inclusions observed in NiTi #1 wire was quite large. Although the size and density of inclusions were not systematically evaluated, inclusions as large as 2 μm were frequently observed.

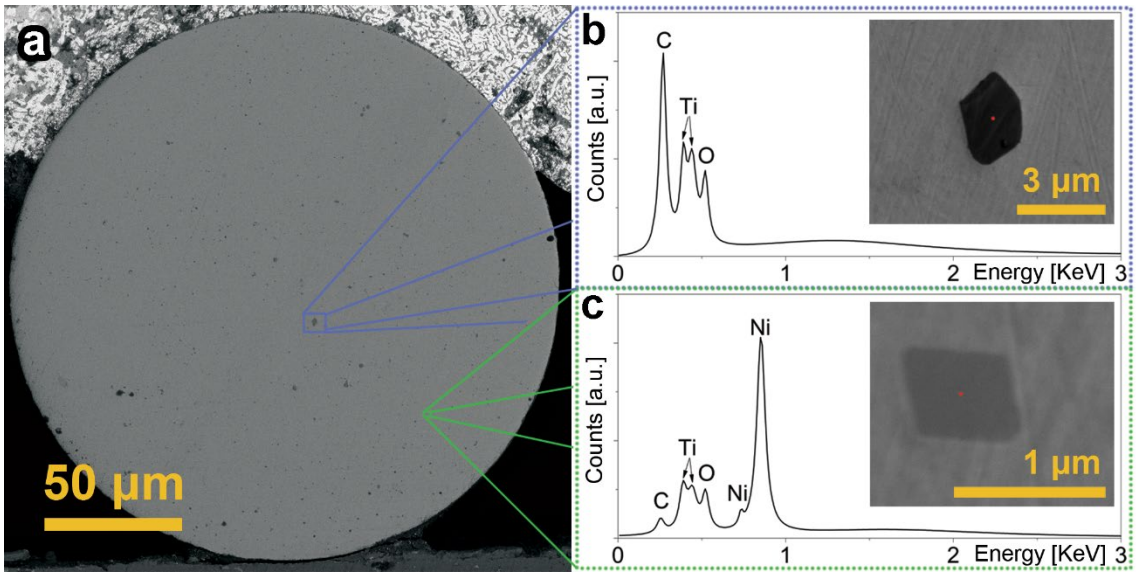

Figure 15: SEM image of the cross-section of (S01) SE NiTi#1 wire in a), corresponding EDS spectra of TiC(O) with a significant amount of substitutional oxygen and intermetallic oxide Ti_4Ni_2O inclusion in b) and c), respectively.

Cold-worked NiTi wires were heat treated either by isothermal annealing in an electric furnace or by Joule heating via a short pulse of electric power. An example of the strong effect of the heat-treatment in a furnace (various annealing times at 350 °C and various annealing temperatures for 30 min. annealing time) on the superelastic stress-strain curves in tensile tests at a constant temperature of 25 °C is shown in Fig. 16a. With increasing annealing time at 350 °C, the shape of the superelastic curve changes and also there is a significant increase in stress hysteresis. With increasing annealing temperature at 30 min. annealing time, the length of the superelastic plateau increases.

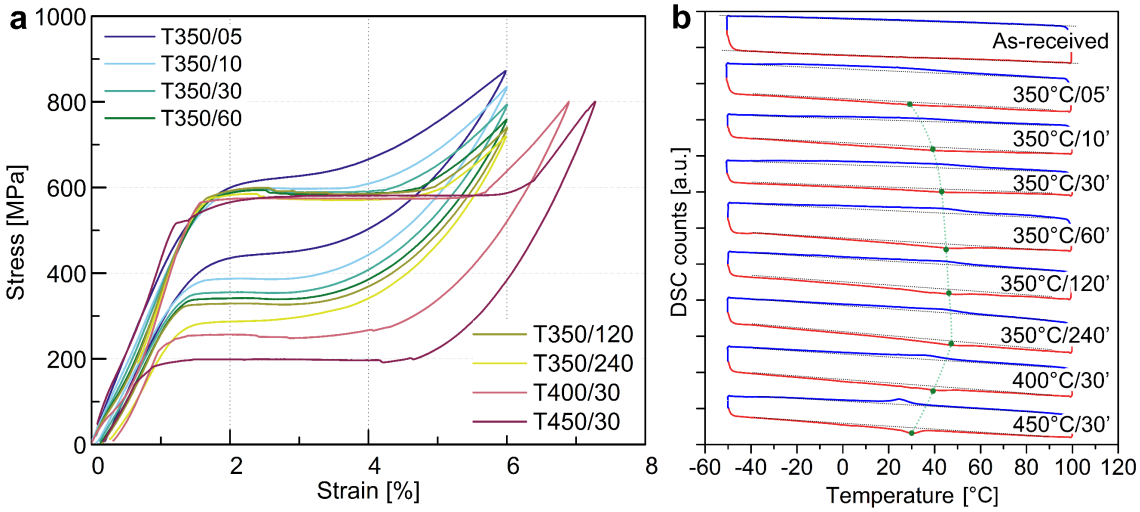

Figure 16: Stress-strain responses of NiTi#1 wire with different heat-treatments a) and the corresponding stress-free DSC curves for each heat-treatment in b).

Fig. 16b shows that DSC curves of the heat-treated NiTi #1 wires informing transformation temperatures at which martensitic transformations occur during stress-free cooling and heating. In order to demonstrate the effect of annealing time and annealing temperature, heat flow peaks due to reverse martensite to austenite transformation are highlighted by green dots. With the increasing annealing time at 350 °C, the peaks are shifting to the higher transformation temperature, together with the narrowing of the peaks. With an increase in annealing temperature, the transformation temperatures drop, peaks become narrower, and their intensity is higher. This pattern can be related to the stress-strain curves in Fig. 16a. The results indicate that the material annealed for a longer time and/or at a higher temperature contains less internal stress and fewer lattice defects.

Moreover, it is well known that families of coherent Ni_4Ti_3 precipitates are introduced by annealing at temperatures 300-400 °C, which results in intermediate R-phase appearing during thermal and mechanical cycles. Small Ni_4Ti_3 precipitates, which remain coherent with the austenite matrix, generate local stress fields which facilitate B2→R transformation and strengthen the NiTi grains against plastic deformation. Simultaneously, Ni-rich Ni_4Ti_3 precipitates cause decrease of Ni content in the matrix which shifts the martensitic transformation to higher temperatures.

Alternatively, NiTi #1 wires were heat treated by a short pulse of controlled electric power utilizing in-house designed and built deformation rig MITTER. The rig was equipped with Peltier's furnace for precise control of the environment temperature surrounding the samples. The special electronics allow sending the controlled short

electric power pulse to the NiTi wire, as a result of which the wire is heated up to desired maximum temperature in the order of milliseconds. The cold work microstructure is recovered/recrystallized during the short heating pulse. The electric resistance of the wire evaluated during the pulse provides important information about the recovery/recrystallization processes during the heat treatment [92]. The same equipment was used to perform shape-setting experiments on already annealed NiTi wires [100].

When doing the electric power pulse heat treatment, the wire is first mounted into the stainless-steel capillaries defining the length of the sample, then to the rig. The initial length and electrical resistance of the wire at a controlled temperature are evaluated, the wire is preloaded to a desired tensile stress and the wire length is constrained. Following that, the wire is subjected to a controlled electric power pulse. Two parameters of the power pulse (power, P, and time, t) are enough to characterize the heat-treatment the wire was exposed to. For better clarity, the used values of electric power are normalized on the 100 mm length of the wire. During our tests, we use the same power pulse and varied the pulse time to obtain NiTi wires with different microstructures [92,101,103]. The notation can be reduced from (Power/Time/Length) only to “Time” because Power = 125W and Length = 100 mm remain constant for all tests. Therefore, the notation of pulse treatment (PT) consists only of time in ms, such as PT 14 ms for wire heat treated by electric pulse 150W for 14 milliseconds. Desired functional and material properties of the NiTi wires can be achieved by the electric power pulse treatment in a highly reproducible way [99].

5 Localized tensile deformation of NiTi on multiple scales

As mentioned in Chapter 2, NiTi shape memory alloys display localization of deformation from the nanoscale to the macroscale. On the nanoscale, this applies to any SMA, since stress-induced martensite transformation proceeds via nucleation and growth of interfaces. On the mesoscale of grains in NiTi polycrystals, this is currently the subject of intensive research in the field using advanced EBSD and SEM-DIC methods. Some results will be shown in Chapter 5.4.

Strain localization on the macroscale is a unique property of NiTi, which affects dramatically its functionality and performance in cyclic mechanical and thermomechanical loads, particularly its resistance to fatigue damage and failure. Therefore, I have paid special attention to the macroscopic strain localization in all experiments in this work. I have developed the 1D-DIC method which can be used to follow strain localization patterns during tensile deformation of NiTi wires as thin as 20 μm. Results of experiments focusing on strain localization phenomena on monotonic loads are reported in this chapter 5. Strain localization phenomena in cyclic mechanical and thermomechanical loads are dealt with in Chapter 6.

5.1 Effect of test temperature on strain localization in tension

Fig. 17a,b shows stress-strain responses recorded in tensile tests on 16 ms superelastic NiTi #1 wires at constant temperatures of 20-400 °C till fracture. Tensile deformation in the transformation range, in which stress-induced martensitic transformation takes place, is localized in Lüders band fronts propagating at constant stress along the length of the wire (Fig. 18). The length of the stress plateau (plateau strain) and thus corresponds to strain localized within the propagating fronts (Fig. 17a). Interestingly, the macroscopic strain localization is observed in a wide range of test temperatures up to the highest test temperature 400 °C. The strain localized within the Lüders band front (plateau strain) depends on the test temperature (Fig. 17c). A maximum plateau strain of 16 ms NiTi wire is observed at the test temperature of 120 °C. NiTi wires having different virgin austenitic microstructures (13ms, 18ms) display similar

temperature dependencies of plateau strain, but maxima appear at different temperatures. Elongation till fracture depends on the test temperature as well (Fig. 17d).

Maximum plateau strains reaching up to 15 % of strain are far larger than the crystallographic limit given by the transformation strain of martensite variant optimally oriented to tensile deformation (~ 11 %). This means, that the deformation of the wire in tensile tests showing large plateau strains cannot be due to B2→B19' transformation only. The observation of long plateaus (Fig. 17c) in certain temperature ranges was explained based on the results of the combination of systematic tensile testing and TEM observation of lattice defects in deformed wires in the article [99]. The observation of long plateaus was ascribed to the fact that the stress-induced martensite in these temperature ranges undergoes (20-1) deformation twinning.

1D-DIC maps showing the temporal evolution of redistribution of local strains during tensile tests at various temperatures (Fig. 18) evidence propagation of Lüders band front up to 70 °C (Fig. 18a-c), even if the transformation plateau strain significantly increases with increasing temperature. In the tensile test at 90 °C, in which maximum plateau strain is observed, transformation stress approaches the yield stress σ^Y for plastic deformation at which deformation twinning in stress-induced martensite massively proceeds.

However, it remained unclear how the wires may display localized macroscopic deformation in tensile tests performed at temperatures as high as 400 °C, at which plastic deformation dominates. Localized deformation is observed in tensile tests at temperatures 120 °C – 250 °C (Fig. 18d-g). However, there are multiple Lüders bands moving one after the other along the wire (Fig. 19). This implies that the wire microstructure created by the passage of the Lüders band front deforms via localized deformation again. This is only possible if the wire remains partially austenitic at the end of the first transformation plateau, which was confirmed by x-ray diffraction [99,103].

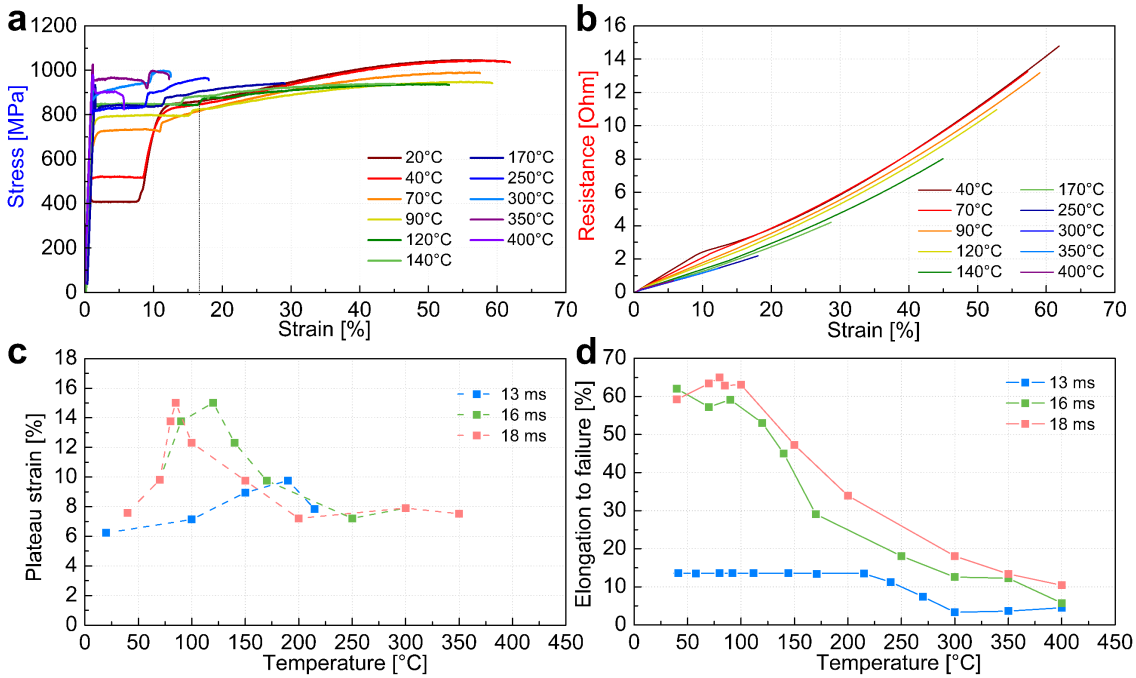

Figure 17: Stress-strain response of NiTi#1 100 µm PT for 16 ms tested in tensile loading until failure at 20, 40, 70, 90, 120, 140, 170, 250, 300, 350, and 400°C in a) and the corresponding evolution of resistance in b). Schematic comparison of strain evolution in the same wire with different heat-treatment in c) and d).

As the temperature increases above 120 °C, the plateau strain decreases, though it still reaches ~ 10 % in the tensile test at 250 °C (Fig. 18g). However, the ductility decreases at the same time (Fig. 17d) which is due to strain localization in a neck within the Lüders band (Fig. 18g-i). One might observe that propagation of the second plateau is already highly localized (Fig. 18h) and large plastic deformation (above 30 %) accumulates within the band upon further loading because of which the band cannot propagate through the whole sample. This is a kind of mix mode involving both Lüders band and necking.

Although we were not able to rationalize the mechanism of the localized tensile deformation of NiTi at high temperatures based on the results of 1D-DIC observations, these experiments turned out to be very important in its research. They brought the following new information:

1. Localized tensile deformation of NiTi is not only due to stress-induced martensitic transformation but occurs also if this is accompanied by plastic deformation.
2. Multiple Lüders band fronts propagating one after the other appear in tensile tests at high temperatures.
3. Ductility at high temperatures is limited by necking within the Lüders band.

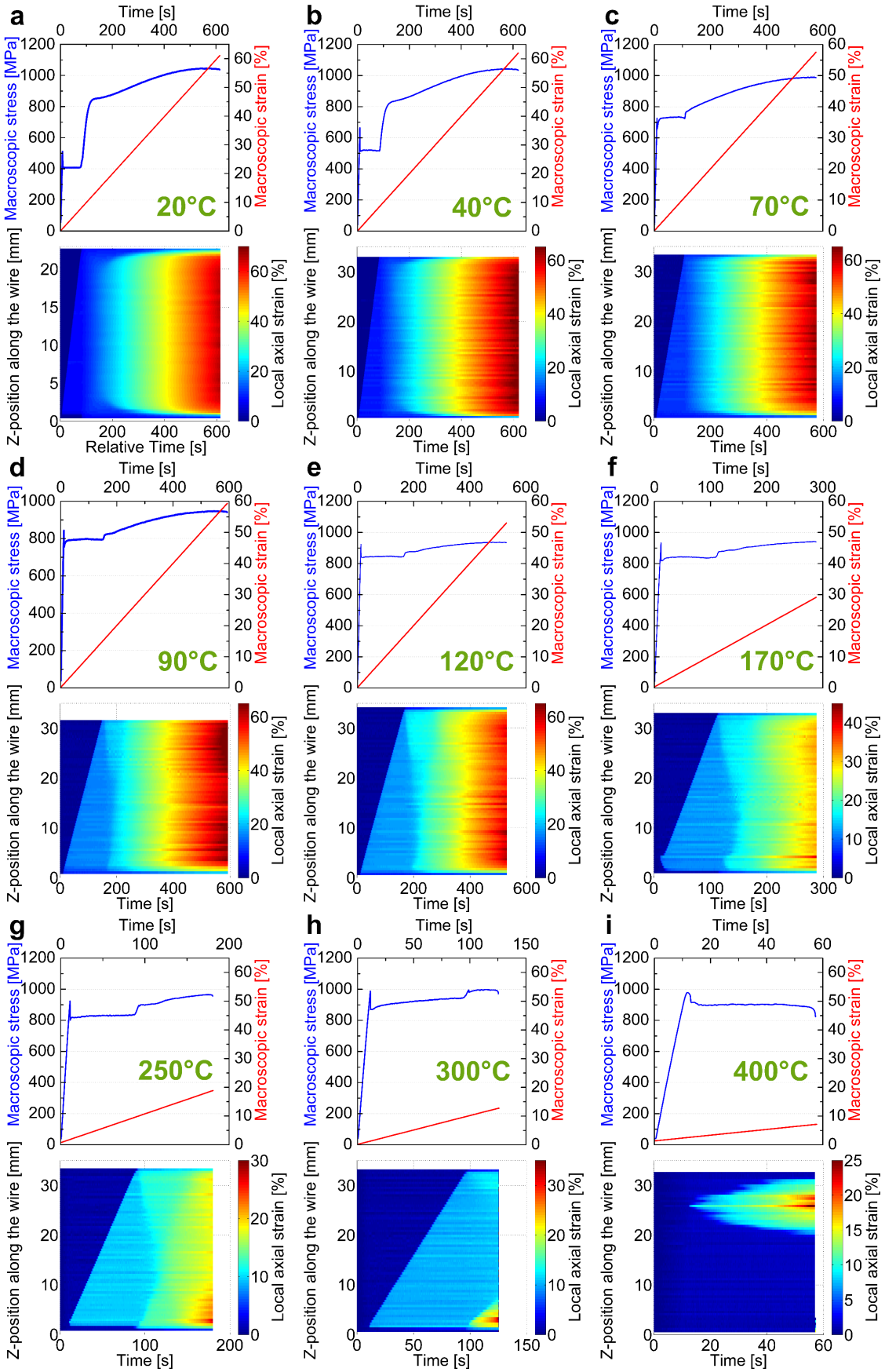

Figure 18: Local DIC strain maps of NiTi#1 100 µm wires pulse treatment for 16 ms tested at 20, 40, 70, 90, 120, 170, 250, 300, and 400 °C in monotonic loading till failure in a) - i), respectively.

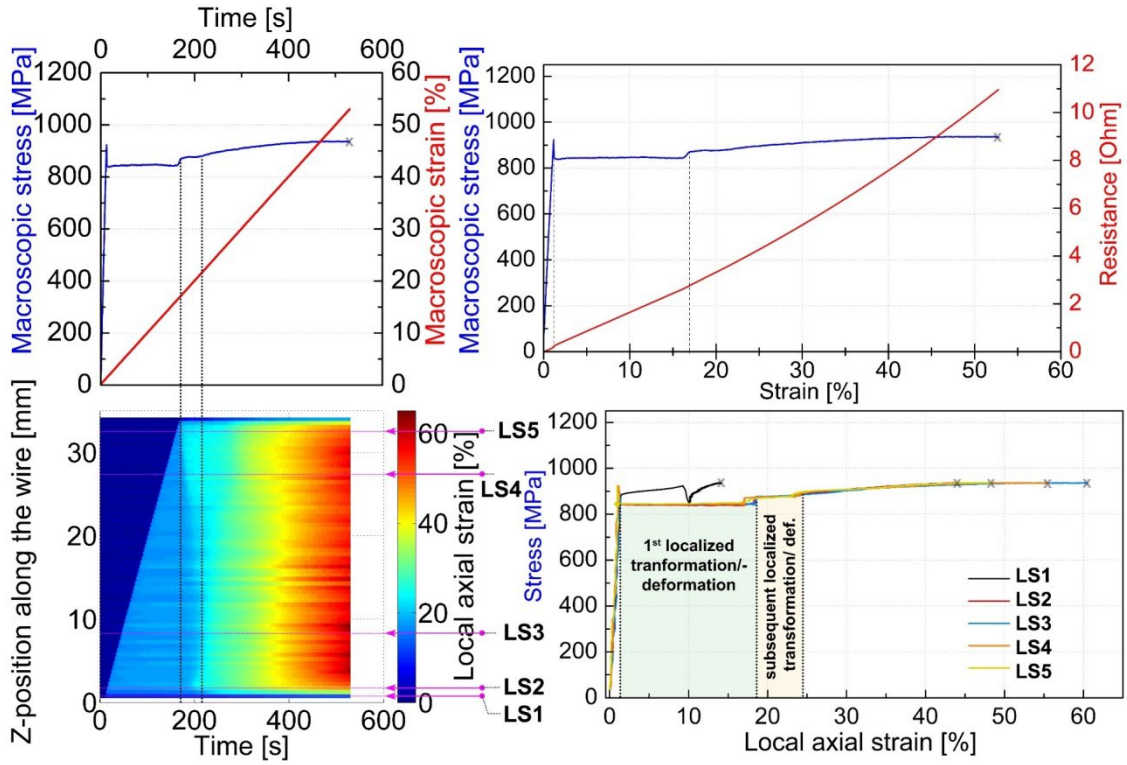

Figure 19: Schematic of the effect of localization and propagation of interfaces in the PT 16 ms NiTi#1 100 µm wire, with plotted local responses showing different material responses across the gauge length of the specimen LS1 – LS5 during monotonic loading in tension till failure.

5.2 Effect of strain rate on strain localization in tension

It is very well known that the strain rate sensitivity of the deformation mechanism significantly affects the ability of the material to resist strain localization in tension (e.g., the role of strain rate in superelasticity). It has been already briefly mentioned in section 2 that, although the stress-induced martensitic transformation is strain rate insensitive, the generation of latent heat during the superelastic deformation under limited heat exchange with an environment at high strain rates, may bring about strain rate effects indirectly. Moreover, if plastic deformation accompanies stress-induced martensitic transformation in tensile tests at high temperatures, strain rate insensitivity of NiTi deformation cannot be guaranteed, since dislocation slip might be involved.

Two experiments on NiTi#1 wire given the same heat treatment of 450°C/30' were performed by tensile tests at 35 °C temperature at two strain rates 0.002 s^{-1} and 0.08 s^{-1} (Fig. 20). Temporal evolution of local strains was evaluated by the 1D-DIC method. While the two Lüders bands nucleated at the stainless-steel capillaries and propagated towards the center in the test performed with a low strain rate, multiple Lüders bands nucleated along the length of the wire and propagated on a short distance in the high strain

rate test. Let us point out, nucleation sites are not spread only along the length of the wire, but also in time.

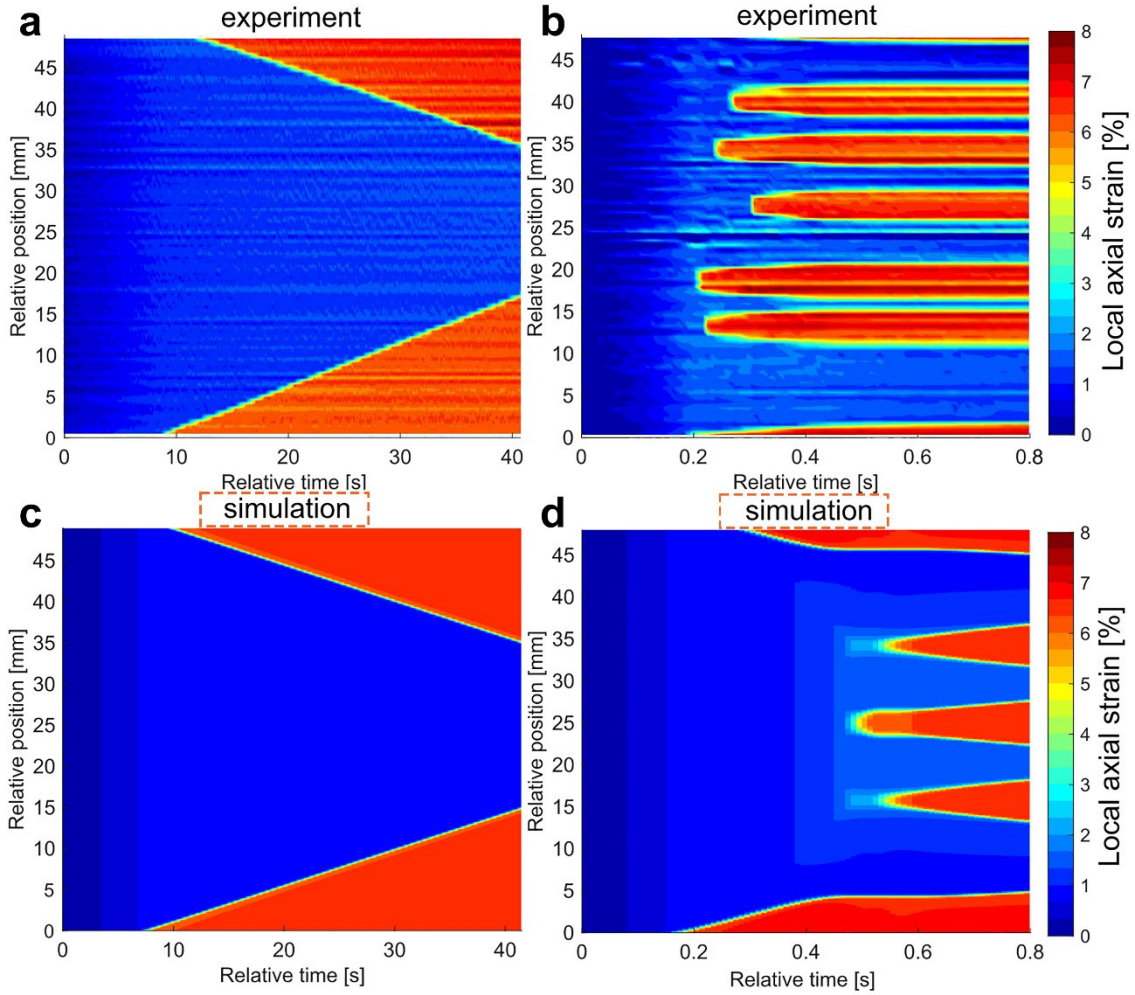

Figure 20: Local strain maps of loading of NiTi#1 wire to 4 % at 35 °C with 0.002 s^{-1} in a) and 0.08 s^{-1} b), and corresponding thermodynamical constitutive model fit shown in c) and d). Adopted from [104].

The results in Fig. 20a, b demonstrate a strong effect of strain rate of macroscopic strain localization in the tensile test. The observed change in strain localization pattern with increasing strain rate originates from adiabatic conditions due to latent heat generation by the fast-propagating Lüders band front in high strain rate tests. It was simulated by the SMA model taking into account these phenomena in [104]. The results of these simulations (Fig. 20c, d) agree reasonably well with the experiment.

Macroscopic strain localization of NiTi in tension, as dealt with so far (Figs. 17-20), is a phenomenon originating from the strain softening constitutive behavior of NiTi. When analyzing it, one has to be very careful, since other external factors may bring strain localization. For example, i) microstructure gradient along the length of the wire, ii) length of the wire, ii) temperature gradient along the length of the wire, or iii) strain gradients in case of complex shape set NiTi wire parts (Fig. 21).

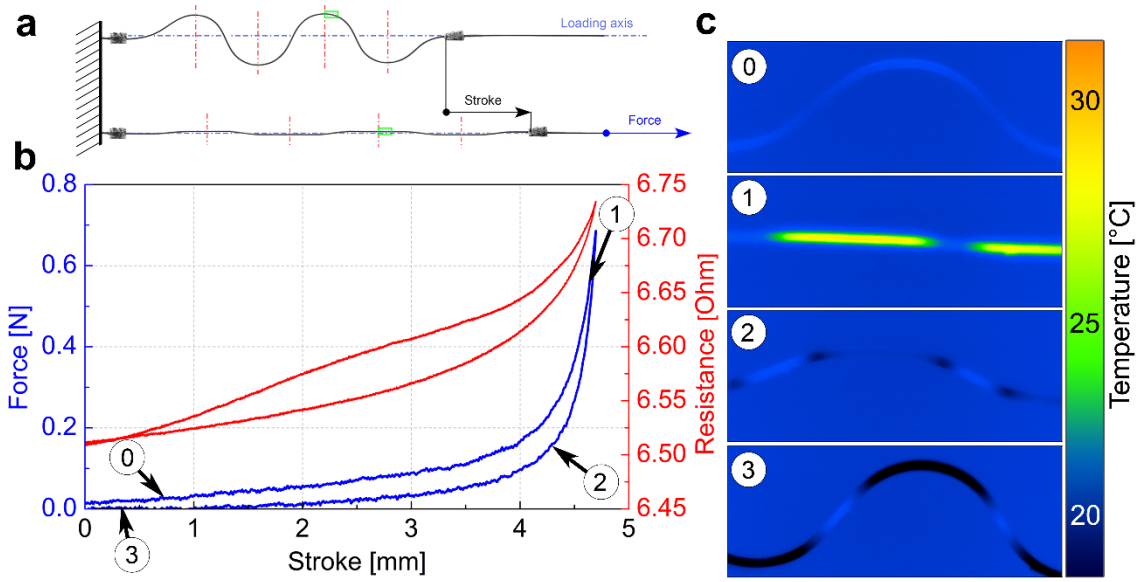

Figure 21: The macroscopic stress-strain curves recorded during tensile tests in tension at 20 °C in a), with inset corresponding to the correlation of pulse time with grain size. b) stress-strain curve of 12 ms wire and c) stress-strain curve of 18 ms NiTi wire with local axial tensile strain along the wire length [107].

5.3 Strain localization during monotonic tensile loading up to fracture

The experiments, the results of which were reported in Chapters 5.1 and 5.2, focused on strain localization of NiTi wires which deformed via stress-induced martensitic transformation. However, it has been known in the literature that strain localizes in moving Lüders band fronts also if NiTi deforms via B2→R-phase transformation and/or via martensite reorientation. Only plastic deformation of martensite was thought to be homogeneous in the literature.

On the other hand, there were those observations of mix mode strain localizations in which plastic deformation is involved (Fig. 18h, i) and also the necking during the plastic deformation, which suggested that even plastic deformation of martensite may proceed in a localized manner. Therefore, we decided to investigate the strain localization phenomena in NiTi without limiting ourselves to the propagation of Lüders band fronts and stress-induced martensitic transformation but consider also necking and plastic deformation of martensite. The results of this research are reported in this chapter.

5.3.1 Experimental background

Plastic deformation of NiTi wires received much less attention compared to superelastic deformation because of two reasons. First and most important is the

attractivity of superelastic or shape memory functional behavior due to martensitic transformation. A second, more practical reason, is that the high-quality superelastic NiTi wires frequently fracture in tensile tests before they start to deform plastically at ~13-15 % strain.

The in-situ 1D-DIC method was applied to investigate the homogeneity of tensile deformation of polycrystalline NiTi samples (NiTi#1, 50.9Ni-49.1Ti at. %, 40.8 % cold work, d= 100 μm, length ~ 23 mm). After heat treatment by a short electric power pulse, these NiTi wires display B2→B19' transformation. We used short pulse heat treatment with parameters of 125W normalized on 100 mm for different pulse times in milliseconds. In this way, we obtained a set of NiTi wires having different microstructures (grain size) and tensile stress-strain responses (Fig. 22a). Majority of experiments were performed on 125W/14ms wires, having defect-free grain size of 215 nm (Fig. 22a). Transformation temperatures of this 14 ms NiTi wire were determined by DSC as A_f= -4, A_s= -37, R_f= -43, R_s= -5, M_f= -109 and M_s= -86 °C. Tensile tests were performed at a constant temperature using in-house designed and built thermomechanical tester (-40 °C up to 600 °C) with electrically isolated grips, enabling in-situ measurements of electric resistance changes during thermomechanical loads. All strains are average macroscopic axial strains. On the other hand, the local engineering axial strains and strain rates along the gauge length are referred to as local strain and local strain rates, respectively.

Tensile testing was performed as follows: The wire sample was permanently gripped into two stainless steel capillaries before it was clamped in the tester grips. The tensile tests were performed at a constant macroscopic strain rate of 0.001 s^{-1} in the range of 10 – 400 °C. The evolution of local axial strains during the test was measured by the 1D-DIC method [105,106]. TEM lamellas were prepared from deformed wires using a FIB-SEM microscope with a Ga ion source. Microstructures in deformed NiTi wires were analyzed by TEM operated at 200 keV using a double tilt sample holder using Selected Area Electron Diffraction (SAED) in the dark field (DF) imaging called (SAED-DF method) [60,98].

5.3.2 Localized deformation of superelastic NiTi wires during tensile testing

Fig. 22a shows stress-strain tensile curves recorded in tensile tests at 20 °C until fracture on NiTi wires heat-treated 125W/0-20 ms. While the cold-worked NiTi wire (0 ms) displays elastic deformation up to ~2 GPa, increasing the pulse time up to 7 ms results in increasing the tensile strain (~ 10 %) as the stress-induced martensitic transformation

during tensile deformation becomes gradually enabled. Starting from ~ 8 ms, localized deformation due to the propagation of martensite band fronts leading to the stress plateau is observed (Fig. 22b, c). NiTi 8-20 ms display localized deformation with stress plateaus, for which the stress decreases, and strain increases with increasing pulse time.

Since 0-14 ms NiTi wires (grain size < 250 nm) fractured at ~ 13-15 % strain (Fig. 22a, b), plastic deformation could be investigated only on NiTi wires 14-20ms (grain size ≥ 250 nm) which deformed plastically up to 55-65 % strain (Fig. 22a, c). Yield stress σ^Y for plastic deformation of martensite decreased with increasing grain size. Based on these results, we decided to investigate the tensile deformation of the 14 ms NiTi wire with grain size 215 nm in detail. We wanted to learn why the ductility varies so drastically with the virgin austenitic microstructure of the wire.

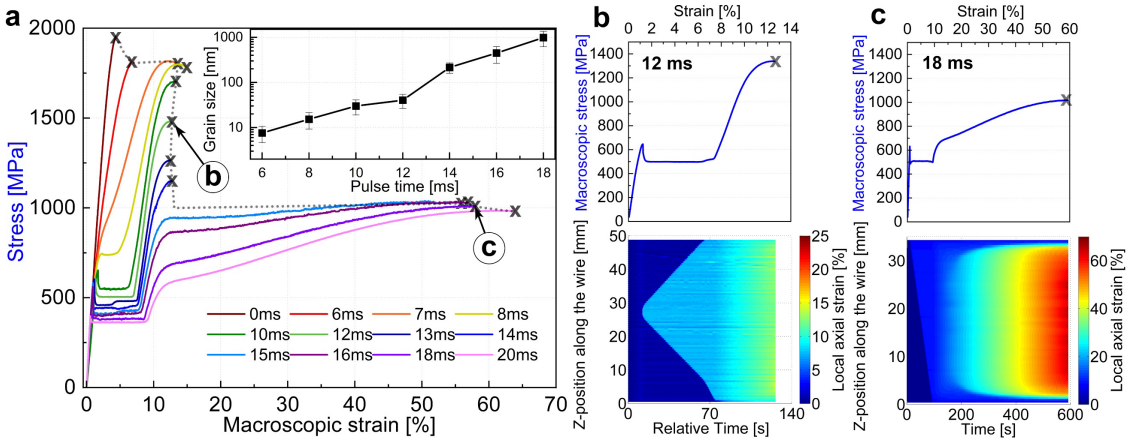

Figure 22: The macroscopic stress-strain curves recorded during tensile tests in tension at 20 °C in a), with inset corresponding to the correlation of pulse time with grain size. b) stress-strain curve of 12 ms wire and c) stress-strain curve of 18 ms NiTi wire with local axial tensile strain along the wire length [107].

Localized superelastic deformation of 14 ms NiTi wire with negligible unrecovered strain during loading-unloading in tensile test at 20 °C is shown in Fig. 23a. When deformed further up to the yield stress, the wire fractures at 13 % strain (Fig. 23b). However, it is not brittle fracture, the wire undergoes extremely fast necking which was on the 14 ms wire registered by the 1D-DIC method (in case of tensile tests on NiTi wires with smaller grain size, despite using high frame rates > 120 s^{-1}, detecting such ultra-fast necking was not possible). This means that large plastic deformation within the neck volume occurred extremely fast. Looking at the fractured wire (Fig. 23c), it is evident that the wire fractured after large, localized plastic deformation within the neck.

Moreover, NiTi wires with ≥ 250 nm grain size also fracture via necking, but much later in the test (>50 % strain). In this case, however, there was no observable stress

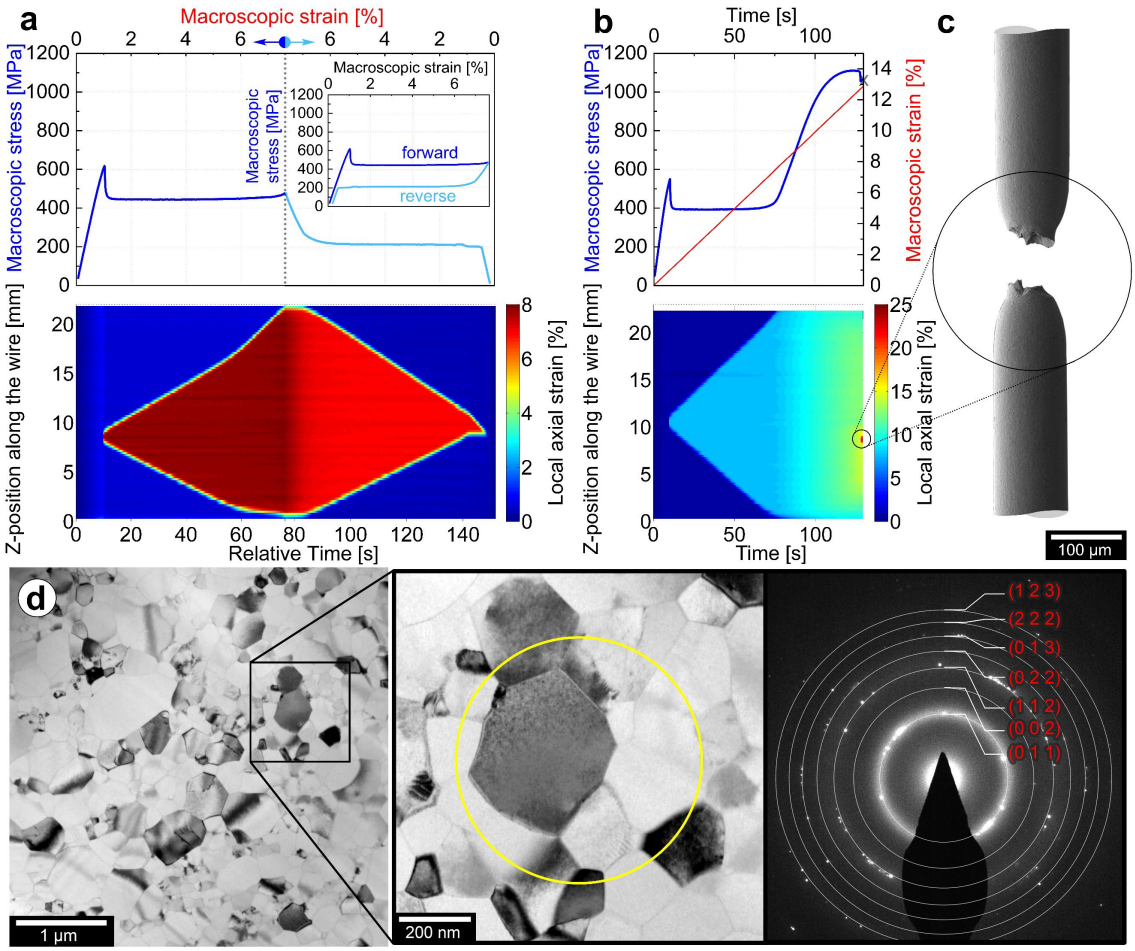

Figure 23: The macroscopic stress-strain curve during the superelastic cycle at 20 °C in a), monotonic tensile loading of 14 ms wire until failure, b) stress-strain curve of 12 ms wire and c) detail of neck after fracture, d) TEM bright field image of 14 ms microstructure with diffraction pattern from the denoted SAED area [107].

drop on the macroscopic stress-strain curve and strain localization was observable by 1D-DIC easily before to the fracture.

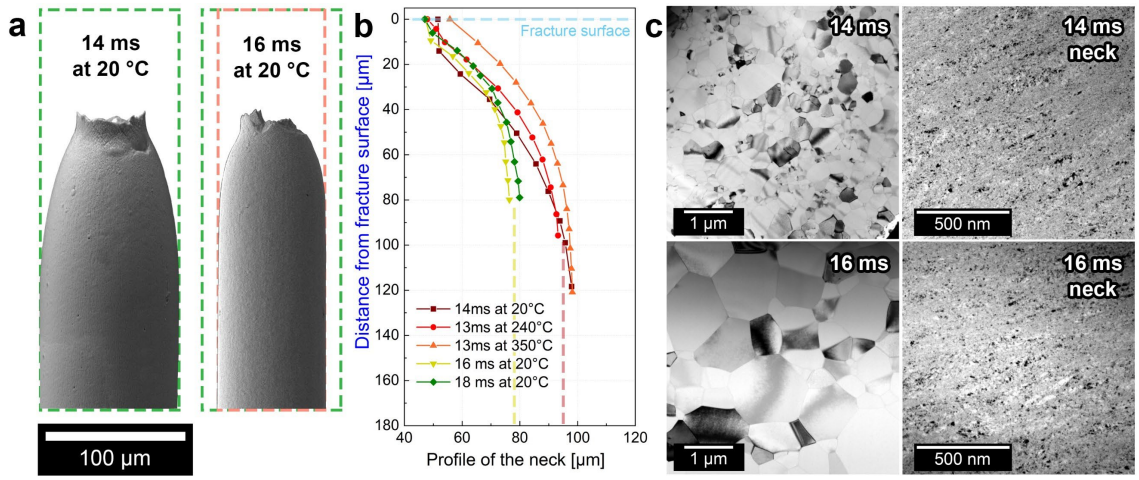

Figure 24: The comparison of fractured necks of 14 ms and 16 ms wires at 20 °C in a), randomly selected side profiles of the necks for different pulse treatments at various temperatures in b). TEM bright field micrographs before and after fracture in the neck area of 14 ms and 16 ms.

It was concluded that the sharp change from the low to high ductility of superelastic NiTi wires is due to the fulfillment of conditions for macroscopic instability of tensile deformation and necking given by Considère's criterion (Eq.3) [108].

$$\sigma = \frac{d\sigma}{d\varepsilon}(1+\varepsilon)\,, \tag{3}$$

Let us point out, that all NiTi wires fractured by necking regardless of the heat treatment applied, but it seems that even in a wide range of pulse treatments and temperatures, at which the material was deformed, the wires ultimately fractured at the reduction of the cross-section to 50 μm ±8 % (Fig. 24).

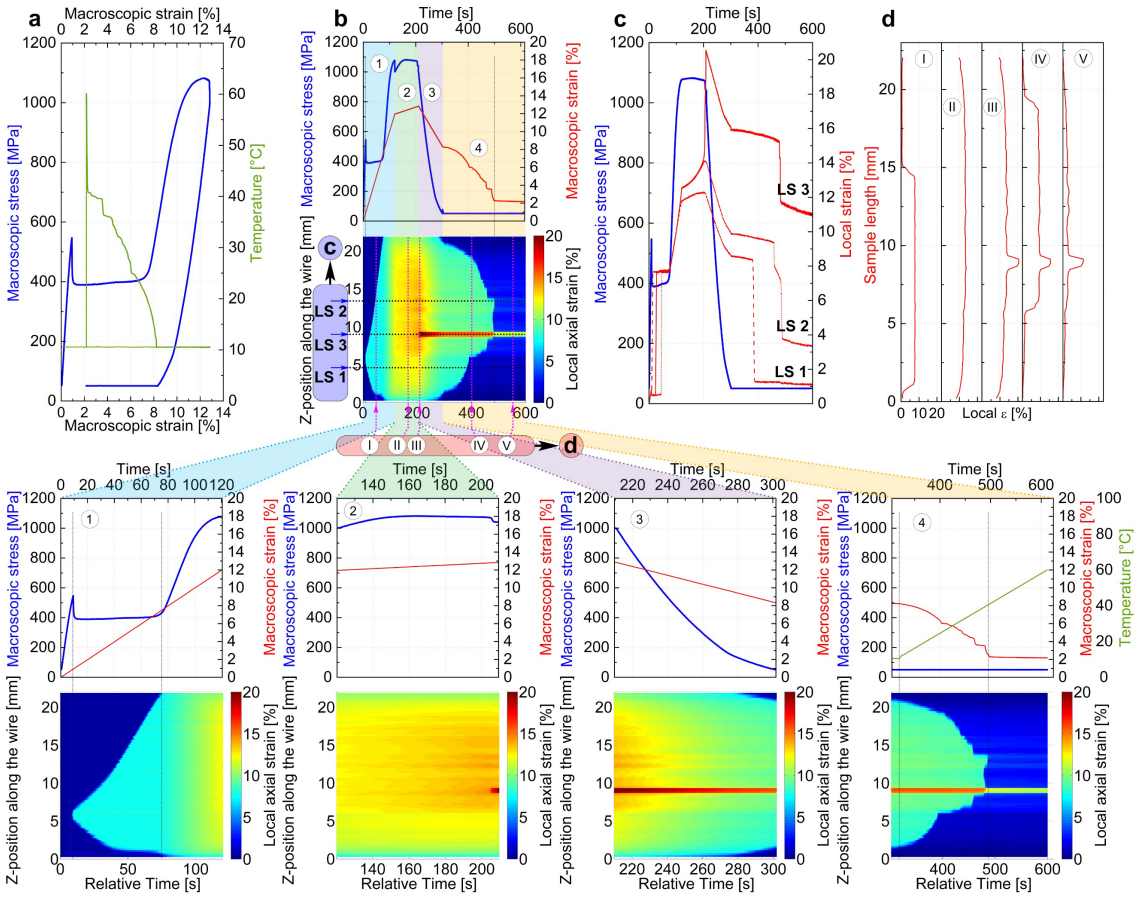

Figure 25: The tensile test of 14 ms NiTi wire in tension at 10 °C until neck forms, unloaded and heated up to 60 °C at 25 MPa a), b) 1D-DIC recording of local axial strain, c) evolution of macroscopic and local strains in points LS1, LS2 and LS3 (defined with blue arrows in b, d) 1D-DIC records in time intervals I-V (defined by pink arrows in b) [107].

The experiment in Fig. 23 was performed again at a slightly lower temperature 10 °C to investigate the strain localization in the neck in detail. Tensile deformation was stopped right after necking started (there is a stress drop ~50 MPa in which the neck was nucleated), but before the wire fractured. Then, the wire was then unloaded to 20 MPa and heated up at constant stress up to 60 °C to evaluate the strain recovery upon heating (Fig. 25a).

Temporal evolution of local strains was evaluated during the tensile test involving: 1) tensile deformation up to 12 %, 2) slower loading until the neck is formed, 3) unloading to 25 MPa, 4) heating to 60 °C at constant stress 25 MPa (Fig. 25b). The wire deformed homogeneously up to ~15 % strain at z-positions 6-18 mm until strain started to localize at z= 10 mm forming a neck in which local strain exceeded 20 %. Then, tensile loading was stopped. The reverse transformation occurred partially during the unloading, but mainly during the subsequent heating from 10 to 60 °C. Local strain responses from different places LS1-LS3 (Fig. 25c) show that the reverse transformation occurred in the whole gauge length including the neck and ~ 10 % strain was recovered. While local unrecovered strains in LS1 and LS2 locations were 1 % and 3.3 %, respectively, 11 % remained unrecovered within the neck in location LS3. The evolution of local strains during all five stages (Ⓘ– Ⓥ) of the test is shown in Fig. 25d.

5.3.3 Effect of temperature on the localized deformation

To evaluate the effect of temperature on the strain localization in tension, a series of tensile tests until fracture was performed on 14 ms NiTi wire within the temperature range 10 °C to 400 °C (Fig. 26). Localized deformation via stress-induced transformation was observed from 10 °C up to 350 °C (Fig. 26a, b). Moreover, the electrical resistance of the wire was recorded in-situ during the tests (Fig. 26a). The higher the electric resistance, the larger the volume fraction of martensite in the wire [103]. The upper-stress plateau (σ_p^{UP}) and ultimate tensile strength (σ_{UTS}) evolve with temperature, as shown in Fig. 26b. The temperature dependence of strains localized within the moving Lüders band fronts and upper transformation plateau (ε_p^{UP}) is shown in Fig. 26c, d.

Fig. 27 presents 1D-DIC records of the temporal evolution of local strains in tensile tests at selected temperatures. Stress-strain response in the tensile test at 20 °C (Fig. 27a), corresponds to the standard response of superelastic NiTi wire. When the yield stress for plastic deformation is reached, strain localizes in the neck and wire fracture ~13-15 % strain. In the tensile tests at higher temperatures 60-80 °C (Fig. 27b, c), the upper plateau stress increases with increasing temperature. When the yield stress for plastic deformation is reached, a second plateau is observed, and strain localizes into macroscopic deformation band fronts propagating along the wire. This strain localization, however, is very different. The wire is already martensitic and the localized strain within the propagating band is 43 % (Fig. 27b).

The second plateau is associated with the plastic deformation of martensite via a peculiar deformation mechanism [107] involving the combination of coordinated dislocation slip (kinking) and deformation twinning in martensite (called kwinking). Therefore, we use the term "kwink band fronts" when referring to the band fronts propagating in the second plateau [99,109].

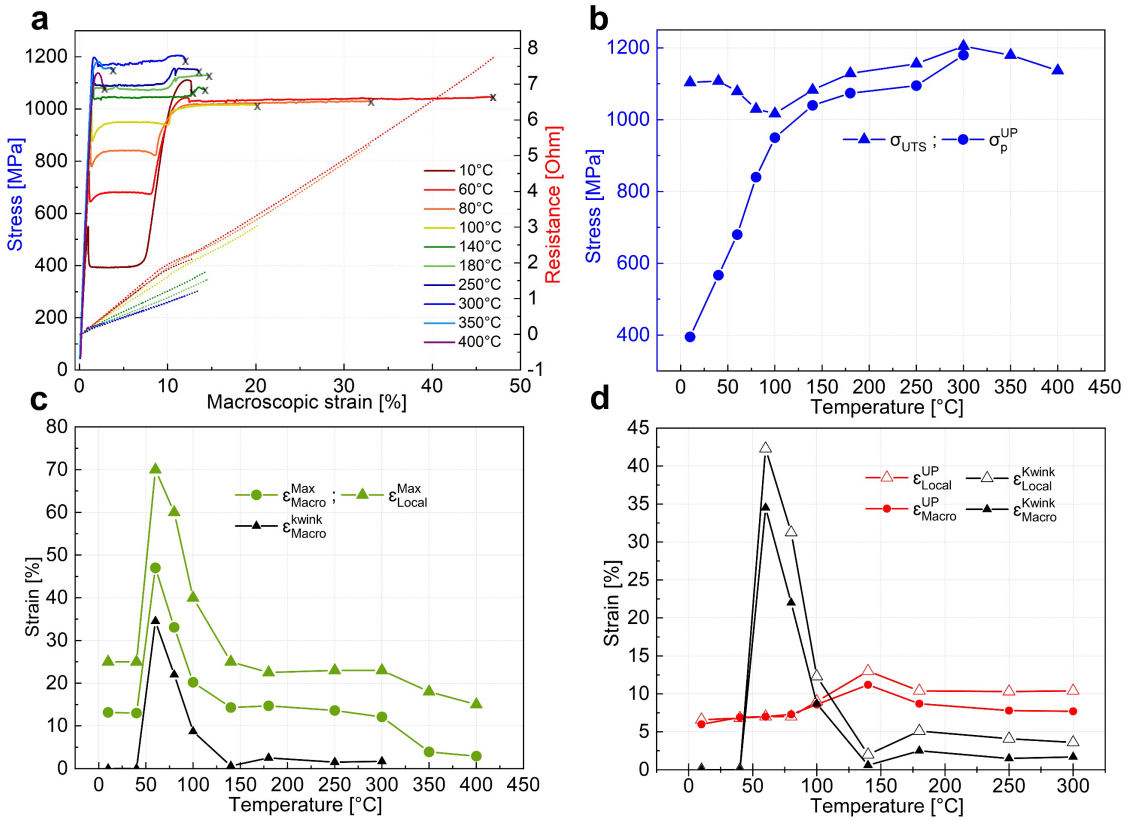

Figure 26: Stress-strain and electric resistivity-strain curves of 14 ms wire a), b) temperature dependence of upper plateau stress σ_p^{UP} and ultimate tensile strength σ_{UTS}, c) temperature dependence of maximum strain $\varepsilon_{Macro}^{Max}$, maximum local strain $\varepsilon_{Local}^{Max}$, maximum localized macro strain within the kwink band $\varepsilon_{Macro}^{kwink}$, d) temperature dependence of upper plateau strain ε_{Macro}^{UP}, local upper plateau strain and maximum local strain by kwinking $\varepsilon_{Local}^{kwink}$ [107].

In tensile tests at higher temperatures of 100-300 °C (Figs. 26, 27d-g), the transformation plateau became unusually long (~15 % strain) due to the phenomenon discussed in Chapter 3.1. The wires fractured due to the strain localization in a neck forming just beyond the end of the transformation plateau at 10-20 % strain. In the tensile test at temperatures ≥300 °C, stress did not increase with increasing temperature anymore and ductility became low. This suggests that no stress-induced martensitic transformation occurred, and the wire was deformed by plastic deformation of austenite.

In contrast to a twin, which is a planar defect joining two of the same but differently oriented variants of B19' phase parts of the crystal, and it is created by simple shearing this defect is the main deformation mechanism in SMAs. On the other hand,

kink appears in layered media in long-period stacking order such as magnesium alloys, which is also a planar interface between two differently oriented lattices. These two lattices are not related by mirror reflection or by shear, but they are related to rotation, and in the kinking, this rotation is provided to this interface by the presence of dislocation pile-ups similar to the low-angle boundary. If these two effects merge, they formed the kwink effect, which describes two lattices creating microstructure similar to the twins, with the different interface created by dislocation kinking, resulting in NiTi B19' plastic deformation forming (20-1) plastic twins by "kwinking" [109].

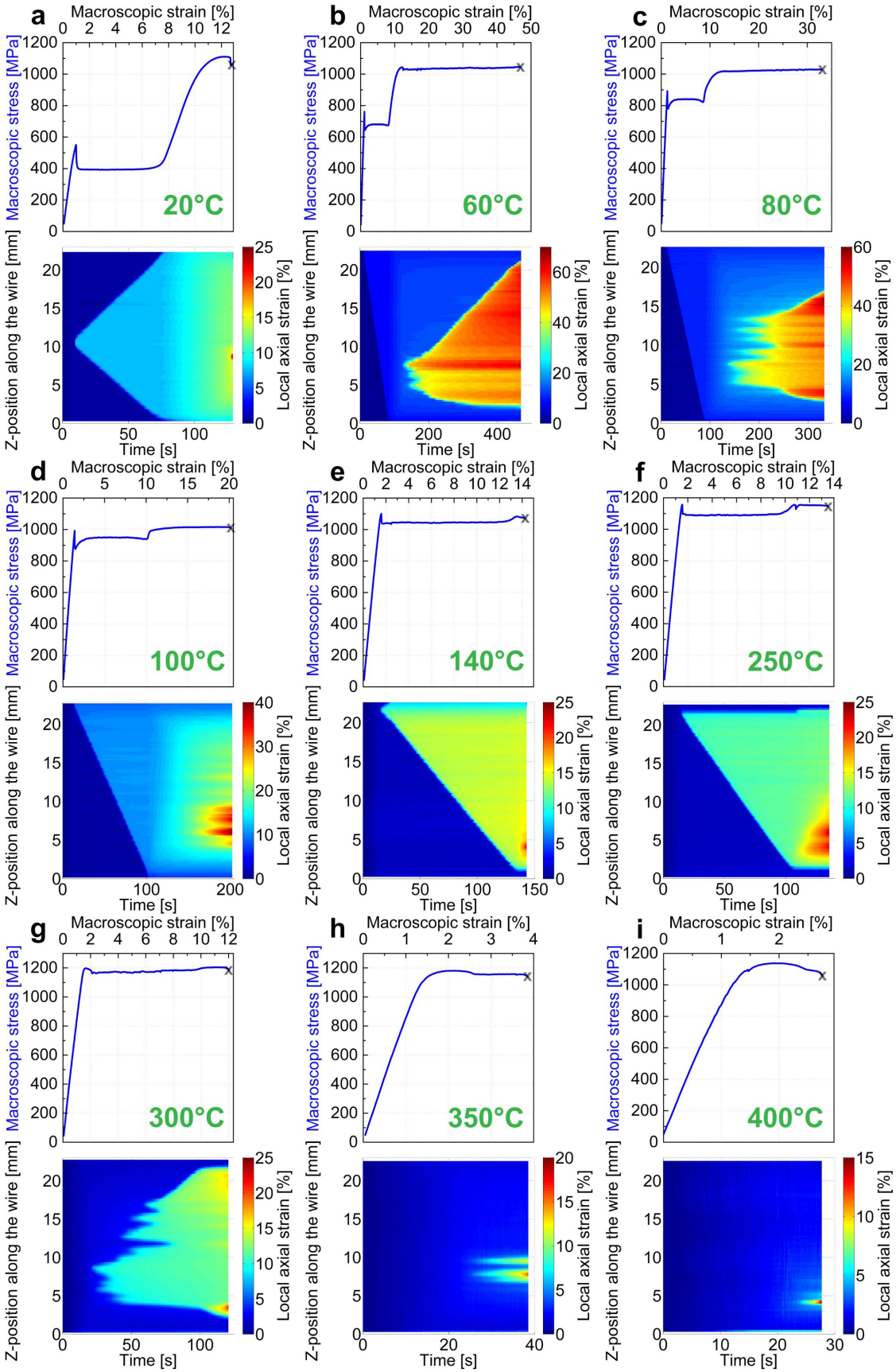

Figure 27: Recording of the evolution of local axial strain by DIC during tensile tests until fracture of 14 ms NiTi wire at temperatures 20, 60, 80, 100, 140, 250, 300, 350, and 400 °C [107].

5.3.4 Localized deformation of martensite via kwinking

The observation of localized deformation of NiTi in tension by macroscopic kwink band fronts in which extremely large strain is localized (Fig. 27b, c) is new in the field and very interesting. Therefore, we decided to investigate it further, but instead of repeating the test until failure, we unloaded the wire at 30 % strain and heated it at constant stress 25 MPa up to 150 °C (Fig. 28). The reverse transformation proceeds partially on unloading and partially on heating. On unloading, strain is recovered via martensitic transformation proceeding in a localized manner in locations, where the kwink band did not propagate, and homogeneously within the kwink band. The strain recovery upon unloading and heating was ~ 10 % in the whole gauge length, however,

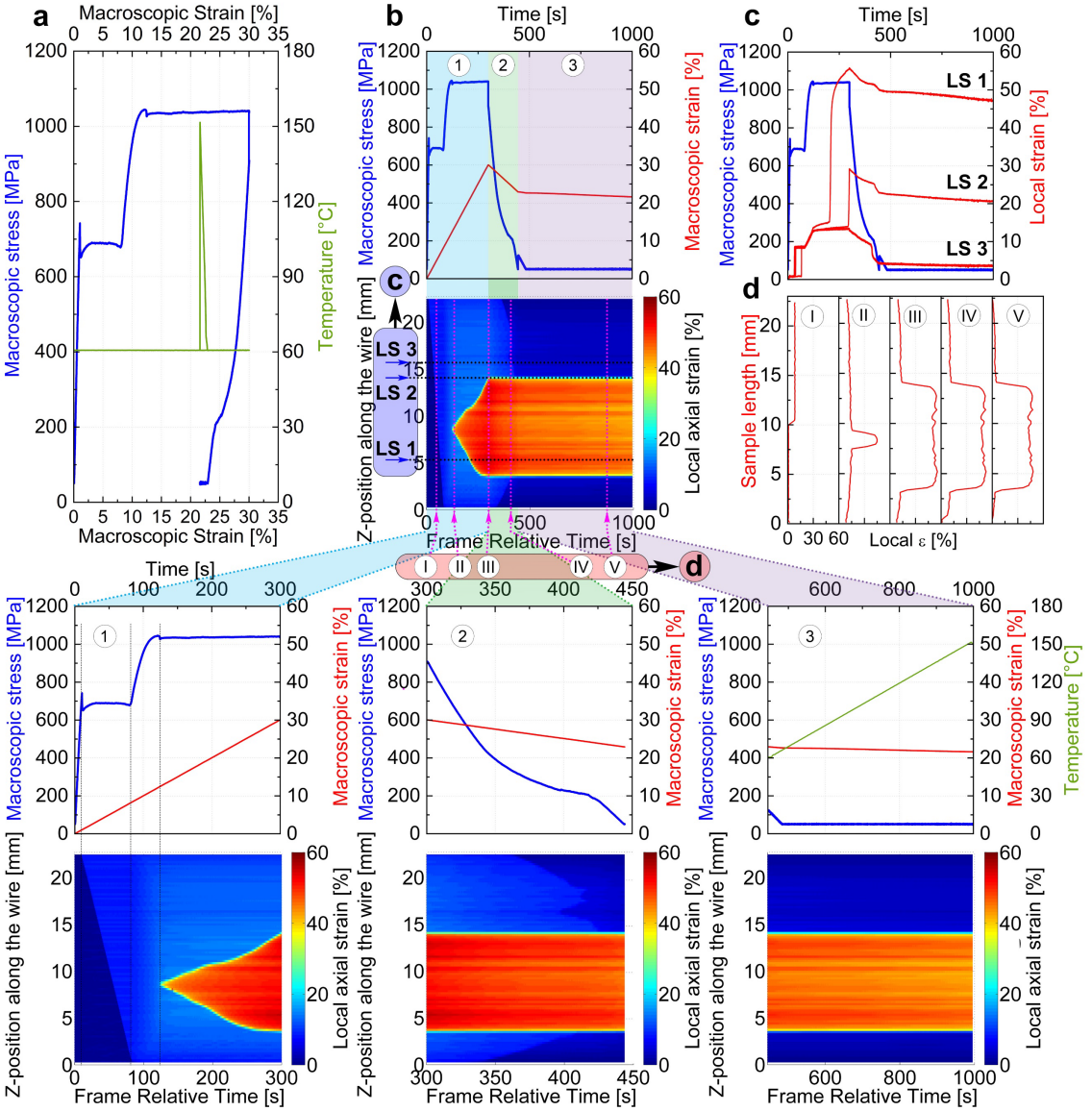

Figure 28: The tensile test of 14 ms NiTi wire in tension at 60 °C until the kwink band fronts propagate to 30 % of macro strain, unloaded and heated up to 150 °C at 25 MPa a), b) 1D-DIC recording of local axial strain, c) evolution of macroscopic and local strains in points LS1, LS2 and LS3 (defined with blue arrows in b, d) 1D-DIC records in time intervals I-V (defined by pink arrows in b) [107].

the unrecovered strains within the kwink band and out of it were very different (Fig. 28c). The strain recovery upon heating was homogeneous in the whole gauge length.

5.3.5 TEM characterization of localized deformation of superelastic NiTi wires

To obtain supplemental information on the deformation mechanism activated within the neck and kwink band fronts, TEM lamellae were cut from the deformed and heated wire (Fig. 26, Figs. 29-32) and lattice defects in deformed wires were investigated by TEM.

As concerns the neck, one lamella was cut from the part out of the neck area (A), and three from within the neck area in regions (B, C, D) as shown in the schematic figure in (Fig. 29b). It was found that the deformed and heated wire is austenitic everywhere out of the neck (Fig. 29A). The lattice defects in austenite (Fig. 29A-D) are relicts of the plastic deformation process activated in martensite, which remained in the austenitic microstructure after reverse transformation, unloading, and heating. Out of the neck (Fig. 29A), the microstructure contained isolated deformation bands and slip dislocations in some grains. Within the neck (Fig. 29B, C, D), the density of the defects (slip dislocations and deformation bands) increased from the edge of the neck towards its center (B→D).

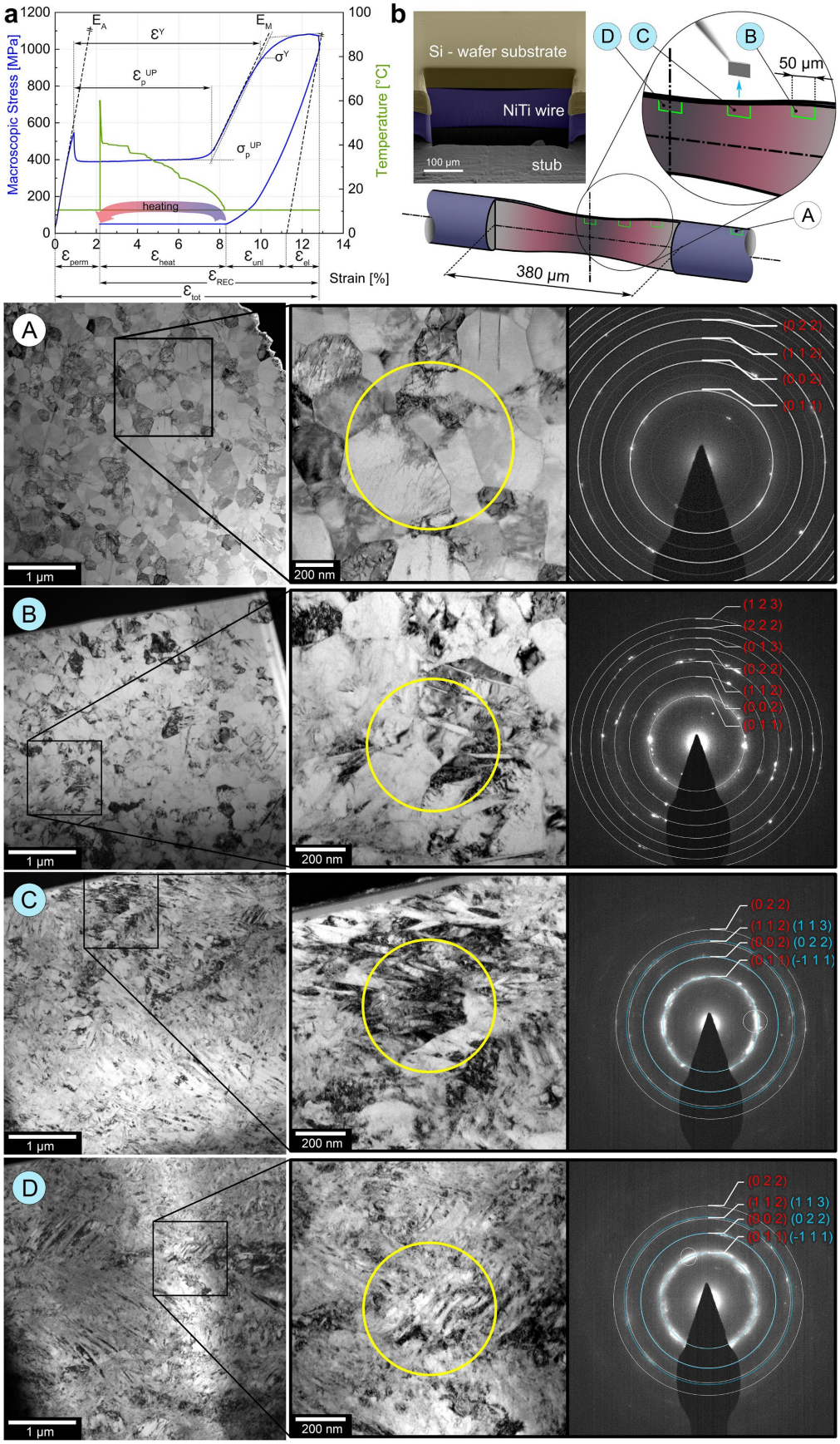

Figure 29: TEM bright field images and SAED patterns of the microstructure from 14 ms NiTi wire deformed beyond the onset of necking at 10 °C, unloaded and heated (same sample as in Fig. 25) a). We prepared the lamellae in the SEM-FIB by Ga source from outside (A) and within the neck (B, C, D) as shown in b) [107].

As concerns the kwink band front (Fig. 28), TEM lamellae were cut within the kwink band and outside of it as shown in Fig. 30. It appeared that the material was only slightly plastically deformed out of the band. This is supported by the observation of lattice defects in the microstructure observed in the lamella from outside the kwink band (A). On the other hand, very large plastic deformation must have occurred within the kwink band (B) (Fig. 30). This large plastic deformation must have occurred within the propagating Lüders band front.

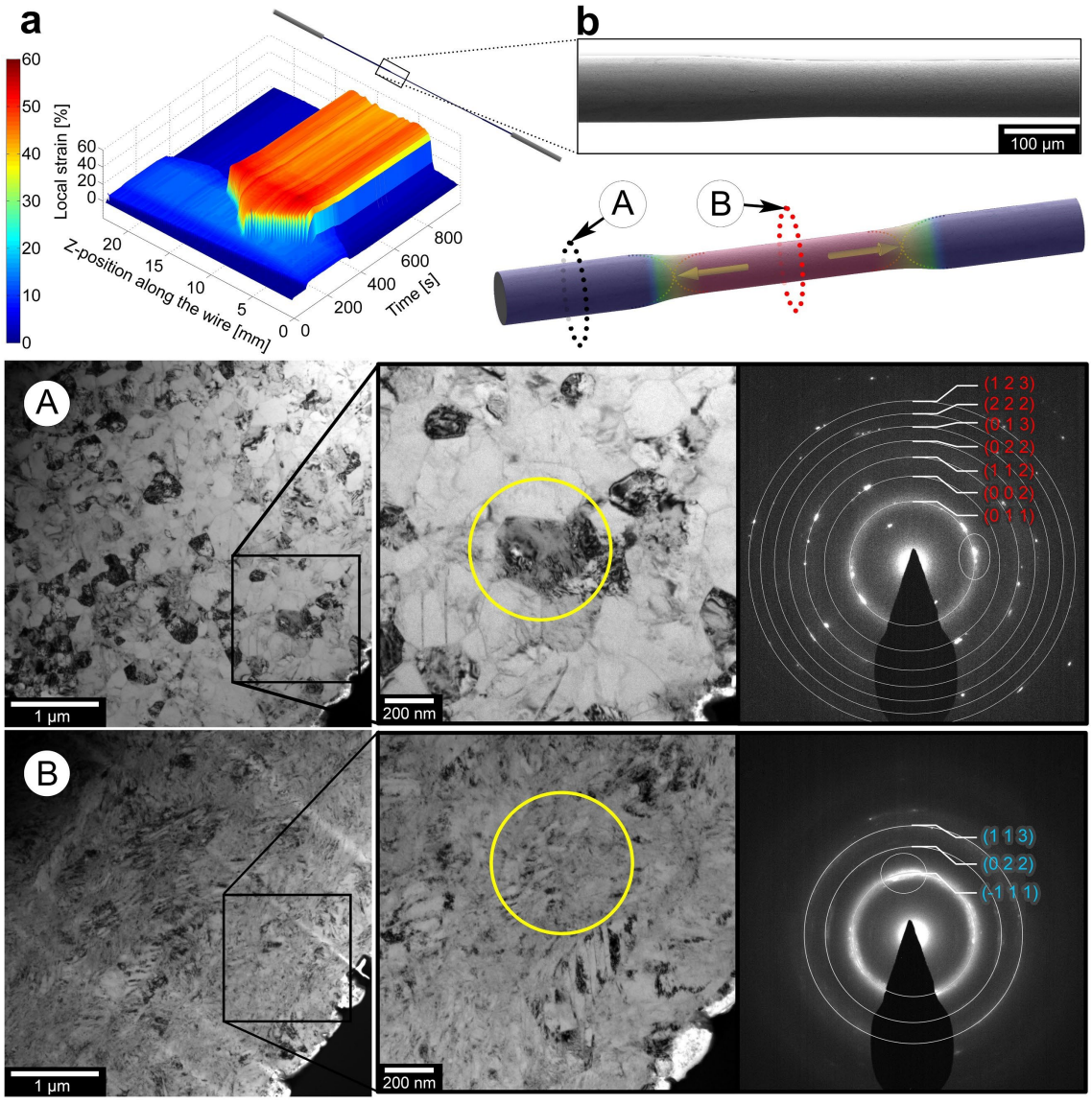

Figure 30: TEM bright field images and SAED patterns of the microstructure from 14 ms NiTi wire deformed up to 30 % strain via propagation of kwink band fronts at 60 °C unloaded and heated (same sample as in Fig. 28). a) 3D presentation of the 1D-DIC record, b) SEM image of kwink band front. Microstructure outside the (A) and inside (B) the kwink band front [107].

However, it is difficult to learn anything about the deformation mechanism acting within the kwink band front just from the bright field TEM images in Fig. 30. Therefore, we analyzed the microstructures within a single grain outside (Fig. 31) and inside (Fig.

32) of the kwink band by the SAED-DF method in TEM. Microstructure out of the kwink band (Fig. 31) contains few deformation bands in wedge arrangement and slip dislocations. The lamella was tilted so that the selected grain was oriented into [1-10] low index zone (Fig. 31b). The grain became dark in the BF image because whole grain volume diffracts electrons within the primary beam. It was found that the diffraction pattern taken from the two SAED areas denoted in (Fig. 31b) correspond to three differently oriented overlapping austenite patterns, all oriented within the [1-10] low index zone (Fig. 31c, d). One pattern corresponds to the B2 austenite matrix (red) and two to {114} austenite twins. In addition, a single martensite diffraction pattern in <010> zone (Fig. 31g, h) originates from few residual martensite plates (magenta) in the microstructure. Selected grain was reconstructed (Fig. 31l) using the analysis of DF images using reflections from each individual lattice (Fig. 31e, f, i, j). The SAED-DF

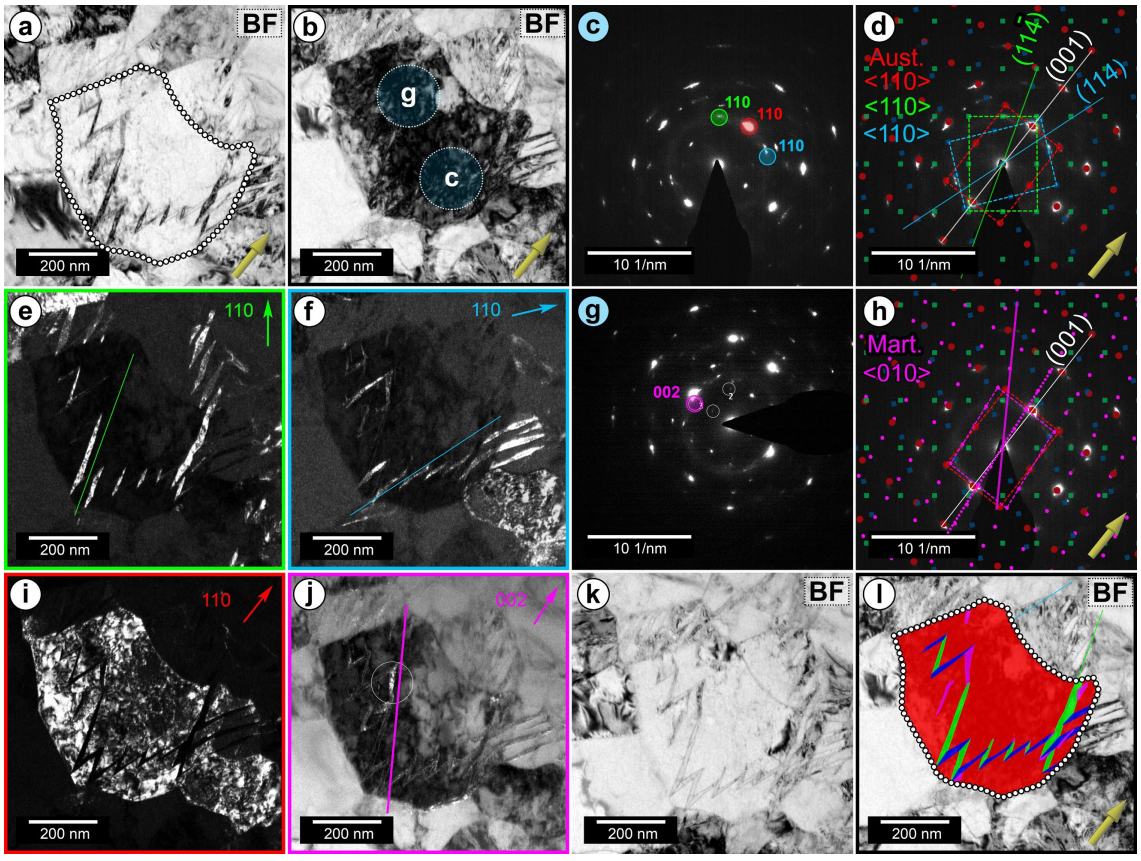

Figure 31: TEM SAED-DF analysis of the microstructure from 14 ms NiTi wire deformed up to 30% strain – outside of propagating kwink band fronts at 60 °C unloaded and heated (same sample as in Figs. 28, 30). a) grain filled with few thin bands, b) tilted lamella into [1-10]A low index zone and diffraction pattern c) was taken from SAED area denoted as (c) in b). Based on the analysis of DF images in (e, f, i), the diffraction pattern corresponds to the three austenite reciprocal lattices in [1-10]A zone colored in d) consists of the parent B2 austenite lattice (red), and two {114} austenite twins (blue & green). The diffraction pattern taken from SAED area (g) in b) is shown in (g, h). It shows additional martensite reciprocal lattices in <010>M zone corresponding to the small volume of martensite relics along the interfaces between the B2 matrix and twins j). The reconstruction of the selected grain in l) built from an austenite matrix, two austenitic twins, and residual martensite. The yellow arrows stand for the orientation of the wire axis [107].

method enables the reconstruction of austenite and martensite variant microstructure in grains of plastically deformed NiTi wires [99,103,110].

The microstructure observed inside the kwink band (Fig. 30B and 32a) contains a mixture of crystalline and nearly amorphous lattices and a high density of deformation bands. The individual grains in the TEM lamella display a ring diffraction pattern suggesting the presence of a very fragmented structure within the kwink band, in which individual grains are difficult to resolve. Nevertheless, a few small grains containing a high density of thin bands and crystalline diffraction patterns were found in the lamella. One such grain was oriented in the [1-10] low index zone (Fig. 32a, b) and analyzed by the SAED-DF method. It was found that the observed {114} austenite twins are not continuous bands, anymore, but mutually interconnected and fragmented bands. The microstructure contains a significant amount of martensite phase, seemingly belonging to a single martensite lattice orientation (Fig. 32h, i). Reconstruction of such heavily deformed microstructure (Fig. 32j) is problematic due to its refinement by the kwinking and high density of lattice defects [109,110].

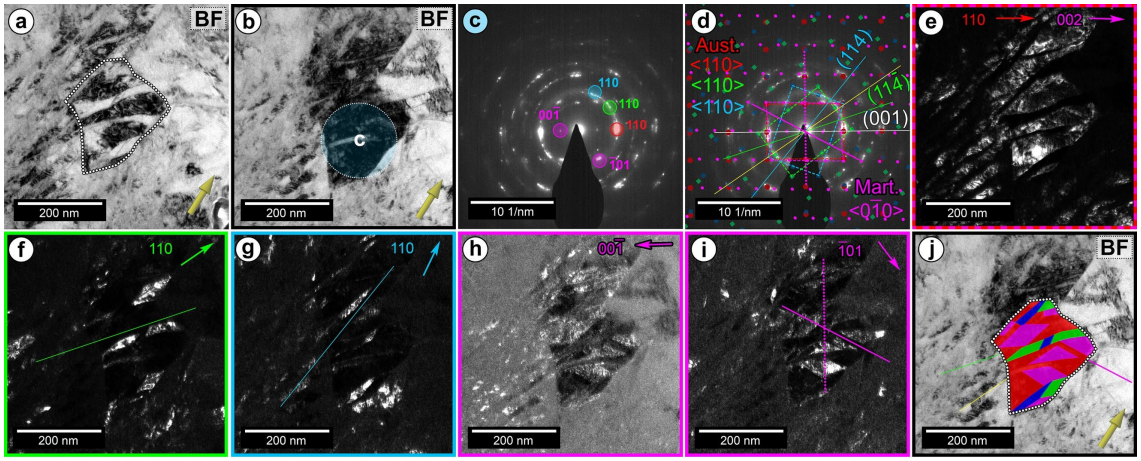

Figure 32: TEM SAED-DF analysis of the microstructure from 14 ms NiTi wire deformed up to 30 % strain – inside of propagating kwink band fronts at 60 °C unloaded and heated (same sample as in Figs. 28, 30). A small grain displaying crystalline diffraction in a) surrounded by nearly amorphous microstructure. b) Lamella was tilted into [1-10]A low index zone and diffraction pattern c) was taken from the SAED area denoted as (c) in b). The diffraction pattern was associated with the austenite lattice (red), two {114} austenite twins (blue & green), and residual martensite within the <010>M zone. Reconstruction of the microstructure j) via DF image analysis (e, f, g, h, i), was difficult since it consists of highly fragmented thin austenite and martensite bands. The yellow arrow corresponds to the wire axis [107].

5.3.6 Microstructure dependence of kwink band front propagation

Whether tensile strain will be localized in necks and the wire will fracture at 13-15 % strain or it will deform homogeneously depends not only on the wire microstructure

(Fig. 22a) but also on the test temperature. In addition, under special circumstances, tensile strain can also be localized in kwink band fronts (Figs. 25, 27).

In order to further investigate the temperature and microstructure conditions under which the strain localization in kwink band fronts is observed, tensile tests were performed on 14, 14.2, 14.4, and 14.6 ms NiTi wires at temperatures 0, 20, 40, 60 °C (Fig. 33). It was found that the kwink band front propagation is observed only for specific combinations of temperature and microstructure (pulse time) (Fig. 34).

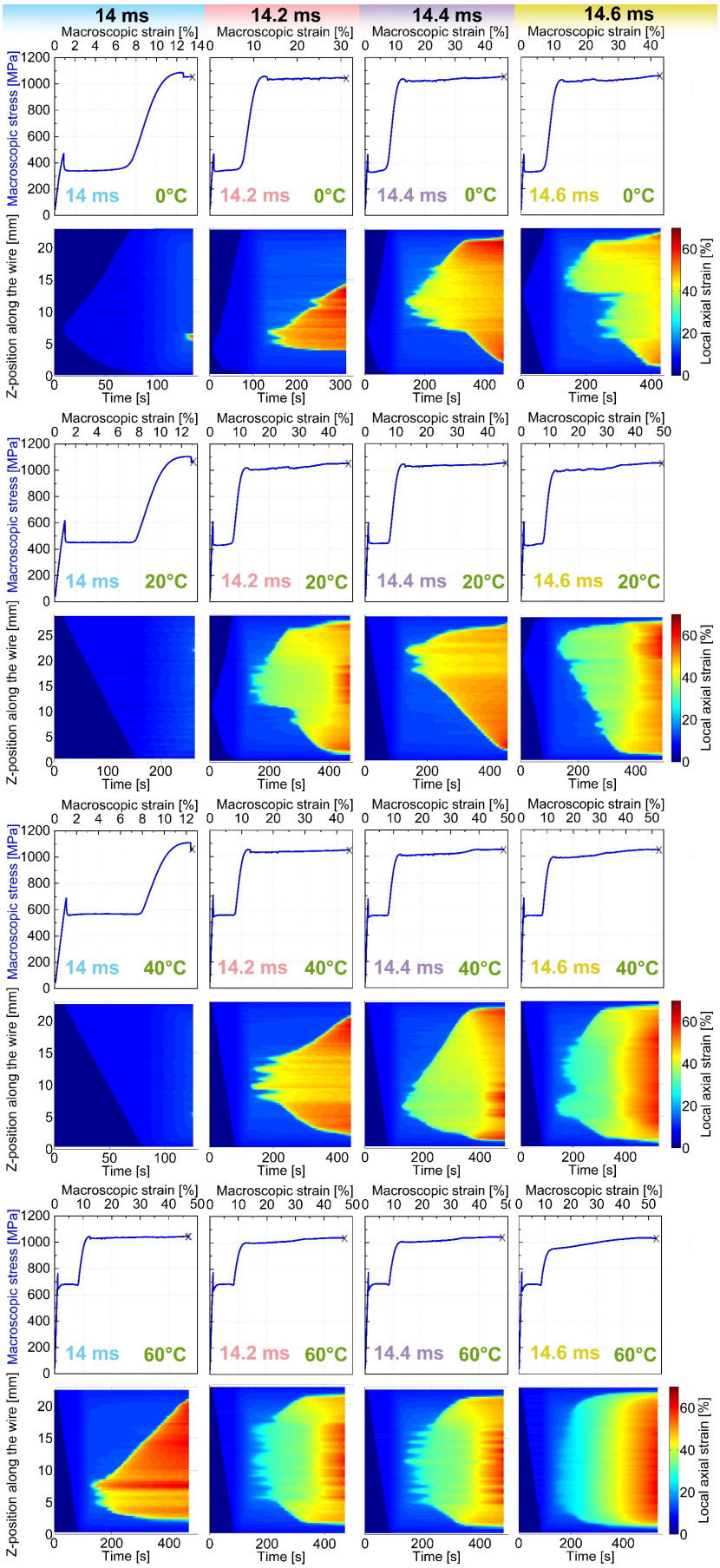

Figure 33: 1D-DIC recording of local axial strain from tensile tests until fracture on NiTi wires with 14,14.2,14.4, and 14.6 ms microstructures deformed at various temperatures 0, 20, 40, 60 °C [107].

5.3.7 Discussion

Results of systematic investigations of localized tensile deformation of superelastic NiTi wires presented in Chapters 5.3.1-5.3.6 revealed two important phenomena. First is that high-quality medical grades NiTi wires having nanocrystalline microstructure tend to fracture just beyond the yield stress at ~13-15 % strain due to localized deformation and necking. Second is that NiTi wire can deform plastically in a localized manner via propagation of kwink band fronts under specific temperature and microstructure conditions.

Strain localization and necking at ~13-15 % is a consequence of the instability of tensile deformation of martensite by kwinking, the conditions for which are expressed by Considère's criterion. The reason for strain localization in the neck is that the material deforming by kwinking displays a very low strain hardening rate at very high stresses. A few related observations shall be pointed out in this respect: i) yield stress sharply decreases with the increasing grain size of the austenitic microstructure (Fig. 22) as well as with increasing test temperature (Fig. 17), ii) strain hardening rate increases with increasing strain in the range 15-30 % in case of NiTi wires with medium grains size (14-15ms wires), iii) strain hardening rate increases with increasing grain size as well as with increasing test temperature, iv) necking proceeds very fast (Fig. 23) because kwinking deformation is nearly strain rate insensitive.

The observations (i-iv) are all inherent characteristics of the kwinking deformation. Yield stress and strain hardening rate (depending on the austenitic microstructure and test temperature) control the stability of tensile deformation. Conventionally, Considère's criterion is used to determine the strain at which the strain localization in the neck appears. Since the strain hardening rate of conventional metals continuously decreases with increasing strain, conventional metals frequently undergo necking before failure. In the case of NiTi wires with small grains size (NiTi wires < 14 ms) strain hardening rate is relatively low until fracture and given the high yield stress, this leads to necking and fracture at 13-15 % strain (Fig. 26). In the case of NiTi wires with medium grains size (14-15ms wires) strain hardening rate is constant after the onset of yielding over a stress plateau (its length changes with temperature and microstructure) and later increases with increasing strain. Because of that, localization of tensile

deformation into moving kwink band fronts becomes possible and preferable over necking (Fig. 28).

In addition, the strain rate sensitivity of the deformation mechanism likely plays an important role. When plastically deforming material is strain-rate sensitive, a considerable delay in necking occurs. When plastically deforming material is strain rate insensitive, as NiTi martensite deforming via kwinking, strain localization via necking or Lüders band front propagation is preferred. The lack of experimental observation of necks in tensile tests on nanocrystalline NiTi wires by 1D-DIC is simply due to the extremely high strain rate within the growing neck since kwinking deformation is nearly strain rate insensitive.

Strain localization patterns recorded in tensile tests on NiTi wires with slightly different microstructures within the range of 14-15 ms at different temperatures (Fig. 33) provide detailed information on the strain localization behavior under critical conditions, at which necking changes into kwink band front propagation. Whether plastic deformation by kwinking will be localized in a neck leading to wire fracture at ~13-15 % strain or in mobile deformation band fronts enabling large plastic deformation up to ~60 % strain, depends on the constitutive stress-strain behavior of NiTi via kwinking.

The most interesting phenomenon is the large plastic deformation of martensite proceeding within the moving kwink band fronts, in which strain as large as 40 % is localized. Observation of {114} austenite twins within the band microstructure proves that the martensite deforms within the moving fronts by kwinking. Specific yield stress and strain hardening rate, which depend on the test temperature and wire microstructure, are required for the kwink band front propagation mode.

The mechanism which controls the magnitude of strain localized within the propagating band front (length of the stress plateau) is proposed as follows. Assume that the 14 ms NiTi wire is capable of deforming at room temperature at roughly constant stress beyond the onset of plastic deformation (the material displays a stress-strain response similar to that of 15 ms wire). In other words, we assume that the strain hardening rate is constant beyond the onset of plastic deformation and further increases later. The length of this stress plateau defines the amount of plastic strain to be potentially

localized within the moving kwink band front. Very important is the increase of the strain hardening rate beyond the end of this plateau. If this is absent, the wire fractures via necking at 13-15 % strain, which is what happens in tensile tests on 14 ms NiTi wire at test temperatures lower than 50 °C or in NiTi wires with smaller grain sizes.

The observation of 40 % strain localized within the kwink band front moving under 1 GPa engineering stress (14 ms wire, 60 °C temperature in Fig. 33) means that the microstructure within the kwink band has to resist 1500 MPa stress due to the change of the cross-section of the wire at 50 % total strain. This is indeed the case, notice that while the kwink band front moves in this test, the wire does not deform within the kwink band. Nevertheless, when the kwink band extends over the whole length of the wire, stress further increases and wire fractures since the stress of 1500 MPa approaches the maximum true stress the strengthened material can withstand without additional strain localization and necking.

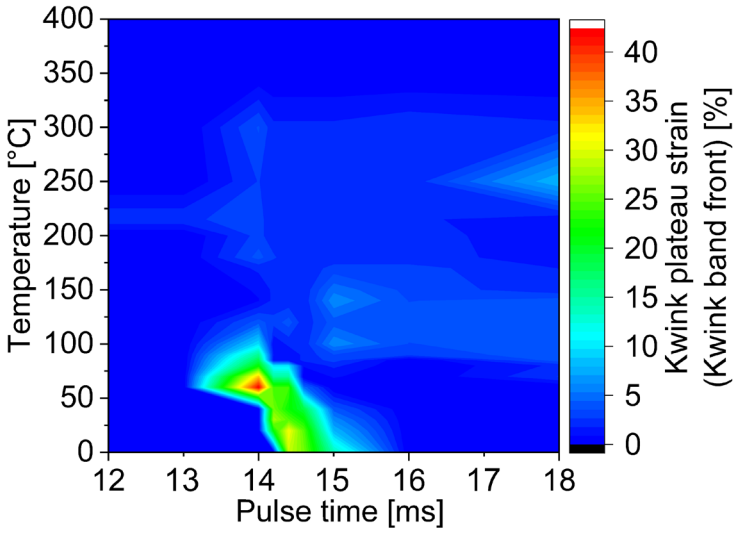

Figure 34: The map with localized strain within the moving kwink band front in dependence on NiTi wire microstructure created by joule heating (grain size/pulse time) and test temperature.

However, strain localized within the band can be much smaller than 40 %. It depends on the wire microstructure and test temperature (Fig. 33). The wire deforms homogeneously after the kwink band extends over the whole length of the wire. Fig. 34 shows strains localized with the moving band fronts in dependence on the test temperature and wire microstructure evaluated from tests in Fig. 33 and some additional tensile tests. Strain-maxima form a band in temperature-microstructure space, which probably continues towards larger grain size and lower temperature. Chen et al. [111] observed localized deformation in $Ni_{47}Ti_{49}Nb_2Fe_2$ alloy in a tensile test at a low temperature (-50

°C) since that alloy had a microstructure with a larger grain size. On the other hand, observation of kwink band fronts in tensile test at temperatures above 100 °C is less likely, since kwinking deformation is suppressed at high temperatures.

Kwink band front propagation mode is observed in tensile tests only within a narrow temperature (~10-60 °C) and microstructure (grain size ~230 nm) interval (Fig. 34). Due to this narrow temperature-microstructure interval, kwink band front propagation mode can be easily overlooked. The kwink band front propagation mode was missed in our earlier work, since tensile tests on 14 ms NiTi wire were not performed at temperatures between 20 and 100 °C.

Very important for strain localization in kwink band fronts is also the already mentioned strain rate insensitivity of the kwinking deformation. As the kwink band front propagates along the wire in the tensile test on 14 ms NiTi wire at 20 °C, the local strain rate within the propagating kwink band front temporarily increases from the prescribed constant macroscopic strain rate 0.001 s^{-1} to the local strain rate 0.03 s^{-1} evaluated experimentally by the 1D-DIC method. If the stress required for kwinking would increase due to the increasing strain rate, the kwink band front would not propagate. While in the case of necking, the strain rate insensitivity of kwinking deformation leads to very fast neck growth (section 4.1), in the case of kwink band front propagation, it enables motion of fronts, in which very large strain (~40 %) is localized.

5.4 Strain localization on the macroscale and mesoscale

Macroscopic strain localization phenomena were discussed in Chapters 5.1-5.3. Strain localization plays also a very important role on the level of individual grains, as follows from the results of TEM analysis of lattice defects in deformed NiTi wires. Since I wanted to obtain experimental information on this mesoscale strain localization on the grain level, I decided to perform in-situ experiments during tensile tests on fully annealed dog-bone-shaped flat NiTi samples in SEM, using the EBSD technique (allows for analysis of the evolution of grain size, austenite/martensite phase composition, local crystallographic texture).

The microstructure of the fully annealed superelastic NiTi (56Ni-44Ti wt.%) is shown in Fig. 35a. The samples annealed at 600 °C for 15 min. display equiaxed grains

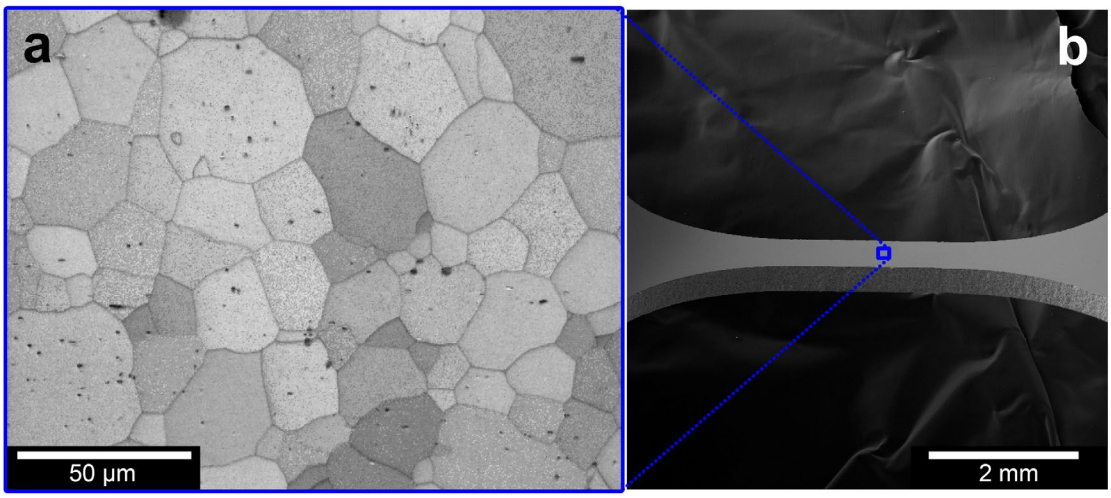

Figure 35: Micrograph of annealed and polished flat dog-bone superelastic NiTi sample with a grain size of ~ 24 µm a). The detail of the mounted flat dog-bone sample in the inclined jaws in the micro tester for in-situ testing.

~ 24 ± 13 µm in diameter. Transformation temperatures were determined by DSC as A_f= 0, A_s= -20, M_f= -110 and M_s= -87 °C.

Fig. 36, shows the tensile stress-strain curve from an in-situ experiment in SEM (TESCAN FERA 3) using a loading stage DEBEN In-situ Microtest installed in the sample chamber. A randomly selected area close to the central axis of the sample was selected as a reference (blue square). The first EBSD pattern (1) was collected at a small preload (20 MPa) only to assure that the sample is straight. After linear elastic loading in the B2 austenite, a newly nucleated macroscopic Lüders band front was nucleated out of this area. This area was marked as (2) corresponding to the onset of forward martensitic transformation on the macroscopic curve. The schematic points (1),(3),(4), and (5) in Fig. 36 represent stages of tensile loading during which the sample strain was fixed, and the deformation band patterns were evaluated (Fig. 37).

The obtained EBSD maps (Figs. 37a, b, c) show that the annealed sample at low prestress consists of $\langle 111 \rangle_{B2}$ fiber texture parallel to the loading axis and beside small defects and inclusions (TiC) only B2 austenite phase. In the Figs. 37c, the kernel average misorientation (KAM) maps illustrate low intergranular local misorientation gradients (< 0.25°) of the annealed microstructure. The macroscopic Lüders band front propagates towards the observation area and the grains start to deform via stress-induced B2→B19' transformation creating deformation bands stretching across the austenite grains (Fig. 37d, e, f). The KAM maps (Figs. 37d-l) reflect the intergranular heterogeneity of plastic deformation due to stress-induced transformation.

At fixed 5.4 % macro strain (3) in Fig. 37f, the area phase fraction reached ~ 3 % of martensite, with intergranular local misorientation ~0.74° for B19' and 0.25° for B2,

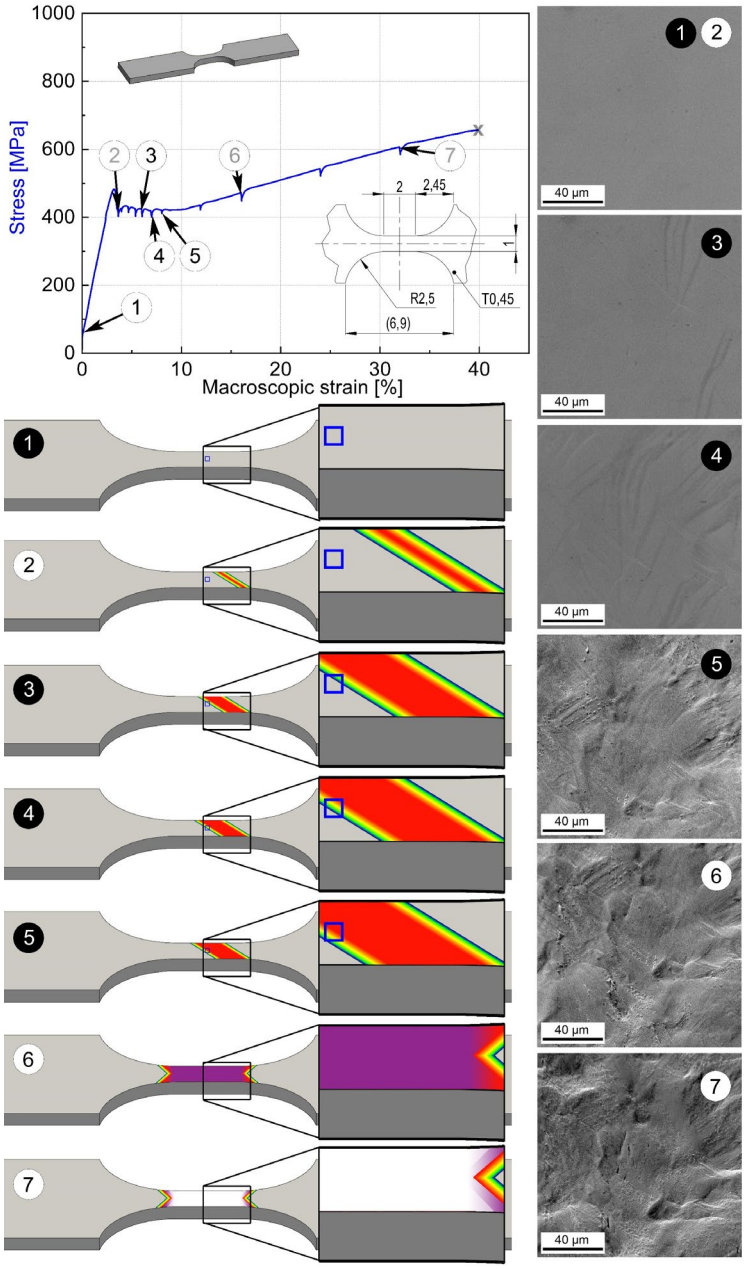

Figure 36: Micrograph of annealed flat dog-bone superelastic NiTi sample with a grain size of ~ 24 µm a). The detail of the mounted sample in the inclined jaws in the micro tester for in-situ testing. Points (1) to (7) correspond to the different prestrains resulting in different surface morphology as shown from SE images. The highlighted stages in black are discussed in detail (Fig. 37).

slightly higher ~0.3° only in near proximity of the martensite bands. At 6 % of macro strain (4) in Fig. 37i, the area phase fraction reached ~ 25.7 % of martensite, with intergranular local misorientation ~ 1.0° for B19' and 0.5° for B2. At 7 % of macro strain (5) in Fig. 37l, the area phase fraction reached ~ 78.5 % of martensite, with intergranular local misorientation ~ 1.1° for B19' and 0.8° for B2.

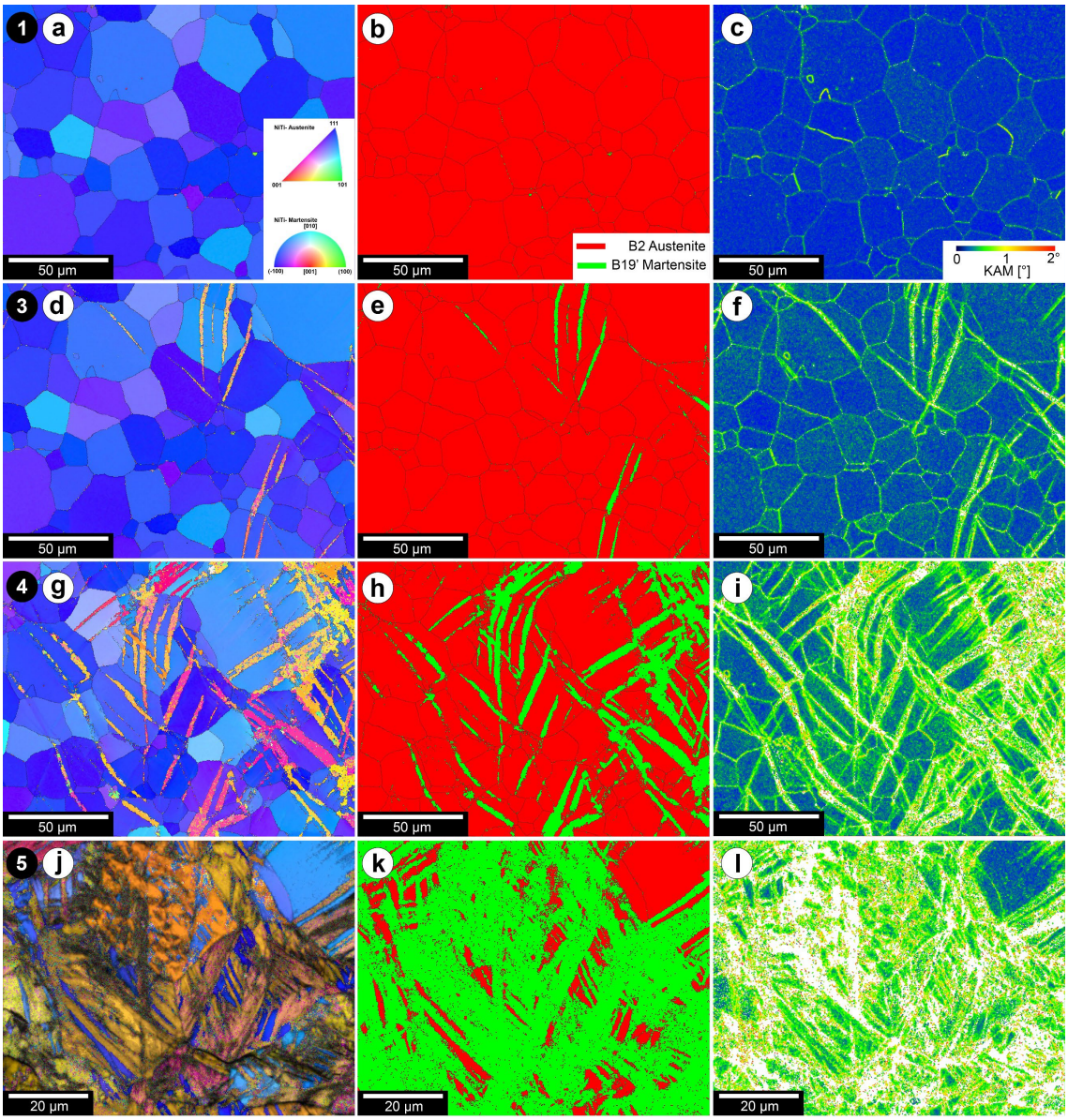

Figure 37: The microstructure represented during stress-induced transformation by inverse pole maps (a, d, g, j), The phase maps (b, e, h, k) where (B2- red, B19'- green) and KAM distribution for both phases (c, f, i, l). Microstructure before loading (1), represented by (a, b, c). Microstructure in front, during and after passing of Lüders band front in (3) in (d, e, f), (4) in (g, h, i), and (5) in (j, k, l), respectively.

The following conclusions were obtained from the in situ EBSD observation of stress-induced martensitic transformation:

1. After annealing at 600 °C, the microstructure contains B2 austenite grains with a strong fiber texture $\langle 111 \rangle_{B2}$ parallel to the loading axis and low KAM gradients (< 0.25°).
2. Macroscopic Lüders band front propagating through the flat dog-bone superelastic NiTi sample with grain size ~ 24 µm is formed by localized deformation bands of B19' martensite.

3. The stress-induced martensitic transformation during monotonic loading in tension results in high KAM values (≥ 1°) in the B19’ phase and at the interface between B2 and B19’ phases. In addition, the KAM values in B19’ bands are higher than in the other parts of the grains.
4. The large shape changes of the surface morphology and the fine microstructure formed by B19’ variants make it difficult to analyze by in-situ EBSD method due to the loss of data quality of the acquired patterns.

6 Fatigue of NiTi structures in tension

When dealing with the fatigue of shape memory alloys, we have to keep in mind two essential circumstances: 1) SMAs display recoverable strain of several percent (~5 % in case of NiTi polycrystal) due to martensitic transformation and 2) SMA behaviors are inherently thermomechanical. The former means that we aspire to develop engineering materials deformable for millions of cycles with ~5 % strain amplitude. The latter means that we cannot limit ourselves only to mechanical cycling at a constant temperature. Closed-loop thermomechanical loads in which all martensite introduced in the forward branch is recovered in the reverse branch have to be performed for a very large number of cycles. Since cyclic thermomechanical tests are difficult to perform, it has become a standard to perform cyclic superelastic and cyclic actuator tests. Although this is not the right approach to the thermomechanical fatigue of NiTi, it has become a standard.

As introduced in Chapter 5, since cyclic thermomechanical responses of SMAs are utilized in engineering applications and stress-strain-temperature responses evolve with the number of cycles, fatigue performance of NiTi SMAs is distinguished between functional fatigue (degradation of stress-strain-temperature responses upon cycling) and structural fatigue (number of cycles till failure). While the former is due to the accumulation of lattice defects and internal stresses generated by the martensitic transformation proceeding under stress [99,103], the latter is due to the accumulation of damage, crack initiation, and crack growth leading to fatigue fracture. It is known that functional and structural fatigues are related but it is not known how.

Like with conventional metals, there is high cycle and low cycle fatigue of NiTi, though with 5 % strain amplitude. Due to the use of NiTi in medical devices (stents), there is a requirement for fatigue performance exceeding 10 million tensile–tensile cycles until failure at body temperature 37 °C. The medical-grade NiTi wires were developed to meet this requirement. However, these tests involve only small strain amplitudes (< 1 %) and NiTi transforms only marginally in these high-cycle fatigue tests. As we aim for analysis of the fatigue of phase transforming NiTi, deformation at small amplitudes will not be the main interest in this work. What is low cycle fatigue in case of NiTi is not very clear because the aspiration is to achieve millions of cycles with strain amplitude ~5 %.

Martensitic NiTi can be used as a damping element working in cyclic tension–compression or cyclic +/- torsion modes. Martensitic NiTi shows excellent fatigue

performance in such tests reaching millions of cycles till failure. However, since the deformation mechanism (twinning in martensite) is not martensitic transformation, fatigue of martensitic NiTi is not dealt with in this work.

The target of millions of (thermo)mechanical cycles with NiTi displaying martensitic transformation can be achieved with NiTi elements working in cyclic compression or torsion but not in cyclic tension, in which the number of cycles until failure hardly exceeds 5 000. However, most engineering applications of NiTi would benefit in wire in cyclic tension and can be utilized for a large number of cycles. This is the reason why I focused on the wire in cyclic tension in my work.

Millions of cycles until failure in cyclic tension were already achieved on NiTiCuCo thin films with specific chemical compositions (lattice parameters) [90,91]. However, this does not solve the problem, since these materials are not suitable for engineering applications. Millions of cycles with a strain amplitude of ~5 % need to be achieved on bulk NiTi samples produced in large quantities. This is the reason why I focused on commercially available NiTi wires in my work.

Millions of thermomechanical load cycles until failure were achieved in the case of thermal actuator cycles on bulk NiTi wires under low applied stress, but never in superelastic cycling in tension. The reason for that is still not clear. I will discuss actuator fatigue only briefly in Chapter 6.7.

It comes out from the brief discussion above that my research of NiTi fatigue was motivated by the goal to achieve millions of (thermo)mechanical loading cycles until failure with commercial medical and actuator NiTi wires in cyclic tensile-tensile tests with strain amplitude ~5 %. The results are reported in this chapter. In accord with the arguments presented above, I do not distinguish between functional and structural fatigue, as well as between low cycle and high cycle fatigue, but speak simply about “fatigue of NiTi in cyclic tension”.

6.1 Effect of strain (stress) mean and amplitude

A medical grade superelastic NiTi wire (diameter of 200 µm) in a cold worked state was heat treated in an environmental furnace at 450 °C for 30 min. The annealed wire shows a superelastic stress-strain response (Fig. 38a) with upper-stress plateau at 600 MPa, 6 % transformation strain, and 400 MPa stress hysteresis. Cyclic tension-tension tests until 250000 cycle or fracture were performed in 8 regions of interest (Fig.

38a) at a constant test temperature of 35 °C in position control with a strain rate of $\dot{\varepsilon} \leq 0.002\ s^{-1}$ (Table 3). The partial cycling tests were controlled by setting strain and stress ranges (highlighted with the blue and red triangles in Fig. 38b) in the tension-tension cyclic tests.

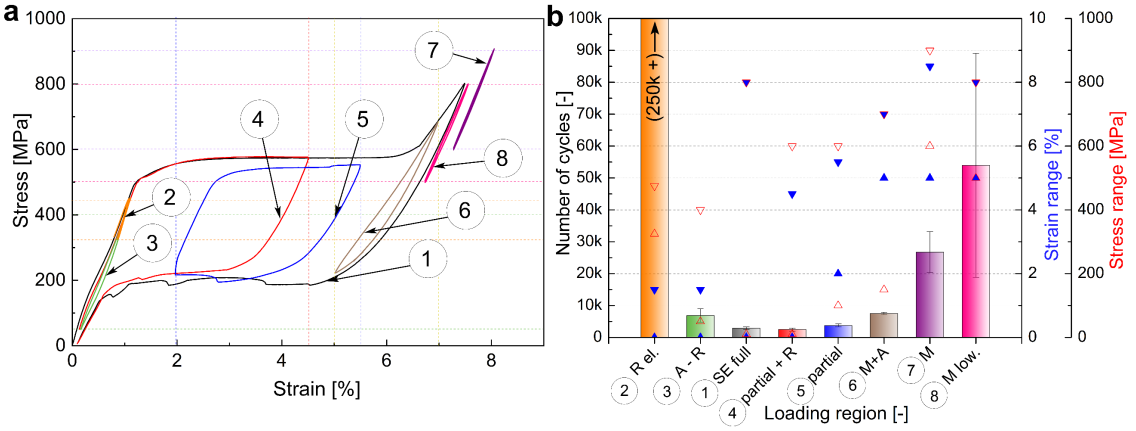

Figure 38: Schematic of pull-pull cycling limited in various stress and strain range. The loading ranges are divided and limited to eight regions within the full range of SE cycling shown in a) and the corresponding column graph with the numbers of cycles until failure for each constricted region in b). Each range window is also numbered and for better clarity are the specific cyclic conditions described in detail in Table 3.

Table 3: Table of different ranges of testing of SE NiTi# 1 wires in tension cycling at a constant temperature corresponding to the data plotted in Fig. 38.

Number [-]	Color [-]	Name [-]	Stress range [MPa]	Strain range [%]	~ Nc [-]
2	orange	Austenite el. + R-phase el.	325 to 475	0 to 1.5	250 000 +
3	green	Austenite + R-phase	50 to 400	0 to 1.5	6900
1	black	Full SE	10 to 800	0 to 8	2950
4	red	Partial + R-phase	10 to 600	0 to 4.5	2550
5	blue	Partial	100 to 600	2 to 5.5	3750
6	brown	Martensite + Austenite	150 to 750	5 to 7	7500
8	pink	Martensite el. low	600 to 900	5 to 8.5	54000
7	purple	Martensite el.	500 to 800	5 to 8	26750

The results can be summarized as follows:

1. The number of cycles till failure is highest in tests in which stress-induced martensitic transformation is avoided (2,7). Any transformation (B2→R, R→B19', B2→B19') taking place upon cycling significantly reduces fatigue performance.
2. If stress-induced martensitic transformation occurs upon cycling, strain amplitude does not affect too much the number of cycles until failure (1,4,5,6)

3. The number of cycles till failure is lowest in tests in which stress-induced martensitic transformation proceeds in a plateau (1,4,5)
4. High stresses or large strains do not necessarily result in worse fatigue performance, (2,3,7,8) In particular, a sample loaded cyclically around ~ 800 MPa in martensite sustains 10 times higher number of cycles than wire cycled around 200 MPa in R-phase (8 vs 3).

These results imply that the effects of mean strain, strain, or stress amplitude known from low cycle fatigue studies on conventional metals do not apply to NiTi SMAs. It is partially due to the unique deformation mechanism of NiTi and partially due to the strain localization phenomena. Overall, it comes out that it does not make much sense to investigate the fatigue of NiTi in partial cycles.

6.2 Effect of temperature and chemical composition

Based on the results presented in Chapter 6.1, I have decided to avoid partial cycling and perform cyclic superelastic tests by loading the wire in tension until the end of the stress plateau. In this way, the wire is forced to transform in a whole volume in the cyclic tensile test. The potential impact of localized deformation on the test results is thus minimized.

6.2.1 Effect of test temperature

Fig. 39 shows stress-strain curves evolving in cyclic superelastic tests on the same NiTi wire at various test temperatures -10, 10, 30, 50, 90, and 120 °C. The tests were performed in two regimes: a) strain limit (upper limit on maximum strain), and b) stress limit (upper limit on maximum stress). The experiments with the strain limit (Fig. 39a) regime were performed in such a way, that the end of the plateau strain in the first cycle was used as a strain limit for further cycling. The experiments with stress limit (Fig. 39b) were performed in position control with a limit on maximum stress. The wire samples were always heated above A_f before the cycling at the desired temperature and tensile cycling was performed at a constant strain rate of 0.002 s^{-1}. The evolution of residual strains accumulated upon cycling was evaluated and plotted for both types of cycling in dependence on cycle number (Fig. 39c).

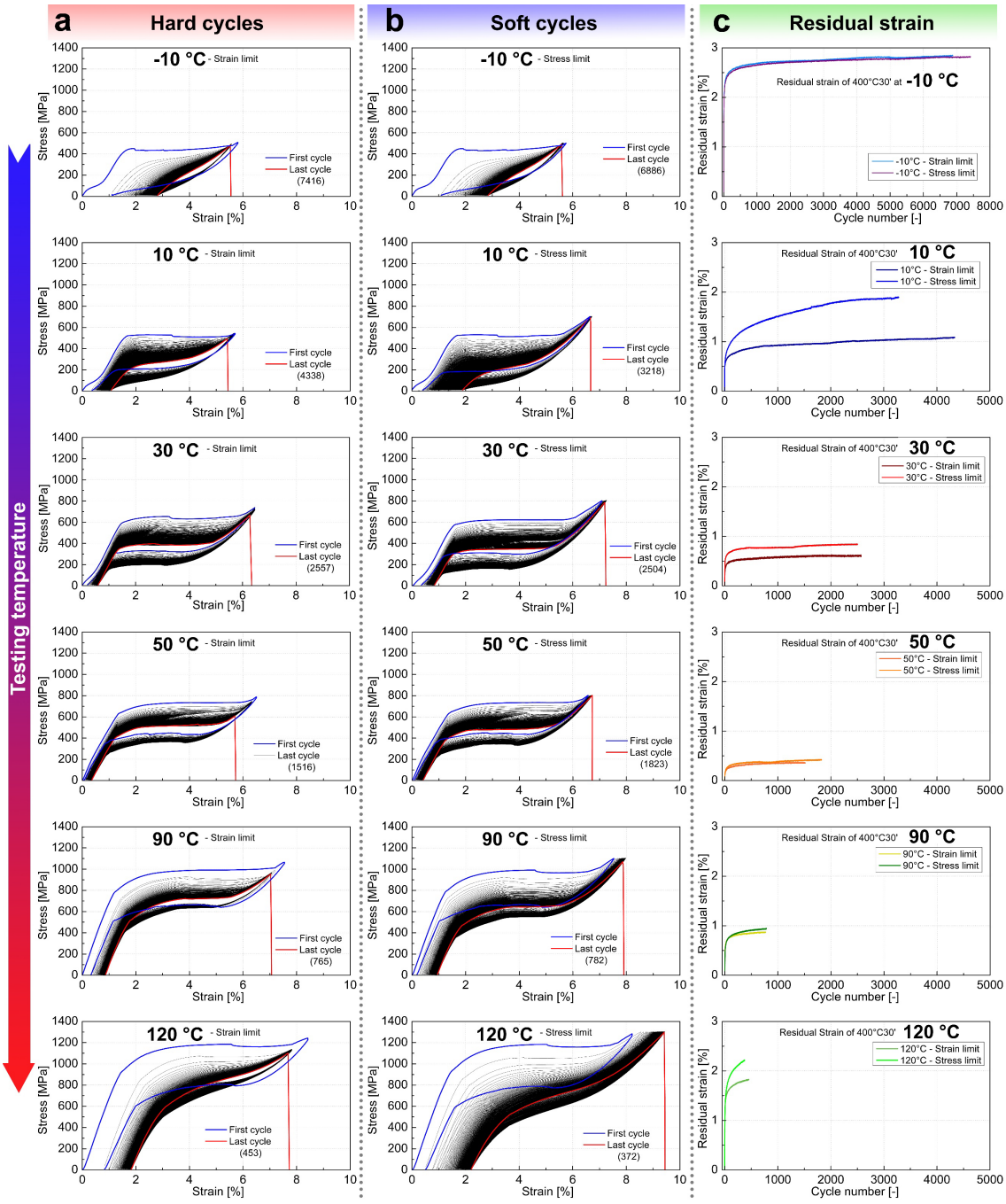

Figure 39: The influence of temperature on the fatigue performance of NiTi#1 wire cycled in tension in so-called hard cycles a), soft cycles in b), and the corresponding evolution of residual strain for types of cycling in c).

The results can be summarized as follows:

1. The number of cycles until failure decreases with increasing test temperature (plateau stress) regardless of the applied strain limit (hard cycles) or stress limit (soft cycles).
2. The number of cycles until failure does not correlate with the cyclic instability of stress-strain response and accumulated residual strain.

3. The reasons for cyclic instability of stress-strain response and accumulation of residual strain are different at low and high temperatures. While residual martensite accumulates at low temperatures, plastic deformation of martensite is responsible for large accumulated residual strain at high temperatures.
4. Regardless of the physical origin of the residual strain, the experimentally observed evolution of accumulated residual strain with the number of cycles till failure shows characteristic two-stage curves with sharp increase and saturation.
5. The cyclic stress-strain response of the wire depends also on the virgin austenitic microstructure of the wire, which was reported elsewhere [17,99]

6.2.2 Effect of chemical composition

In order to understand the effect of the chemical composition of NiTi wires on fatigue performance, NiTi wires with different chemical compositions were tested. First was superelastic NiTi wire (FWM NiTi#1 450°C/30'), which is austenitic at room temperature, and the second was Flexinol wire F90C, which is martensitic at room temperature. Both wires were 200 µm in diameter. Test temperatures were selected in such a way that the range of upper plateau stresses was comparable. For the martensitic wire, this implies superelastic cyclic testing at high temperatures above 100 °C, which is rather unusual. Tensile cycling was performed in position control at a constant strain rate

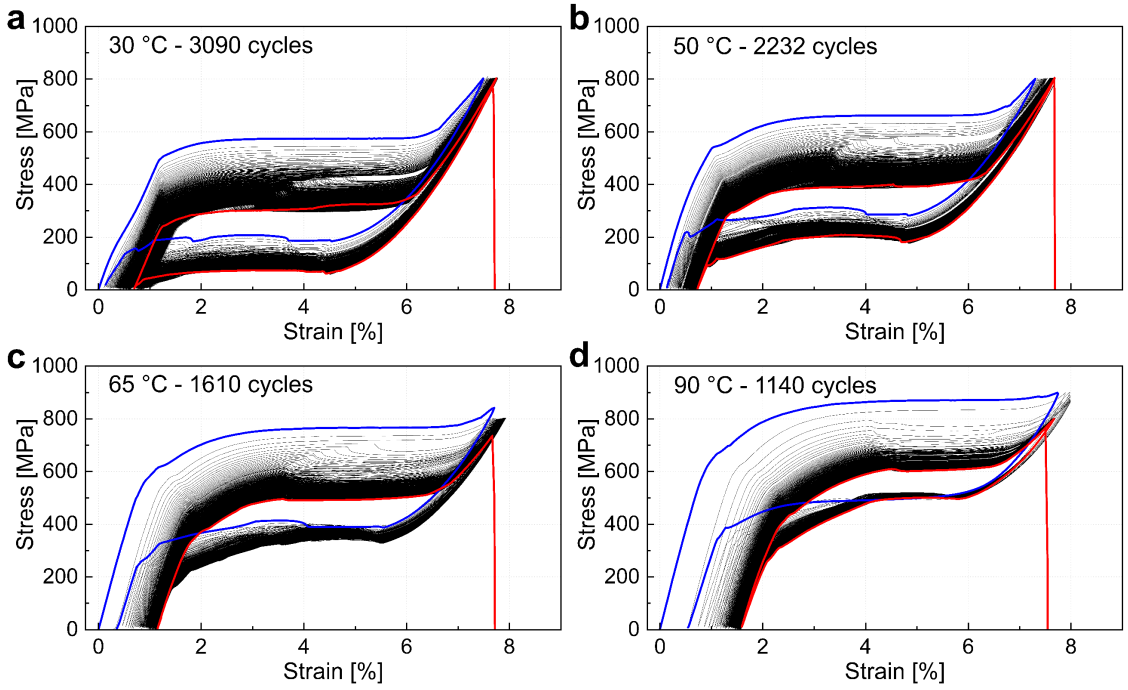

Figure 40: Superelastic cycling of NiTi#1 450°C/30' tested at 30, 50, 65, and 90 °C until failure in a), b), c), and d), respectively.

of 0.002s^{-1}. The results are shown in Fig. 40 (NiTi#1) and Fig. 41 (Flexinol F90C). The number of cycles till failure for both wires in dependence on test temperature is presented in Fig. 42.

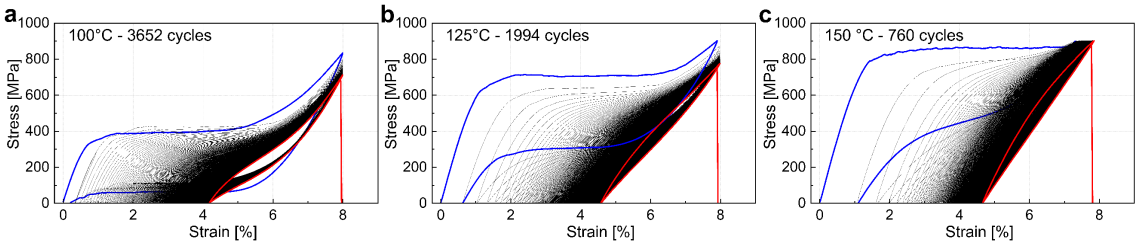

Figure 41: Superelastic cycling of Flexinol F90C at 100, 125, and 150 °C until failure in a), b), and c), respectively.

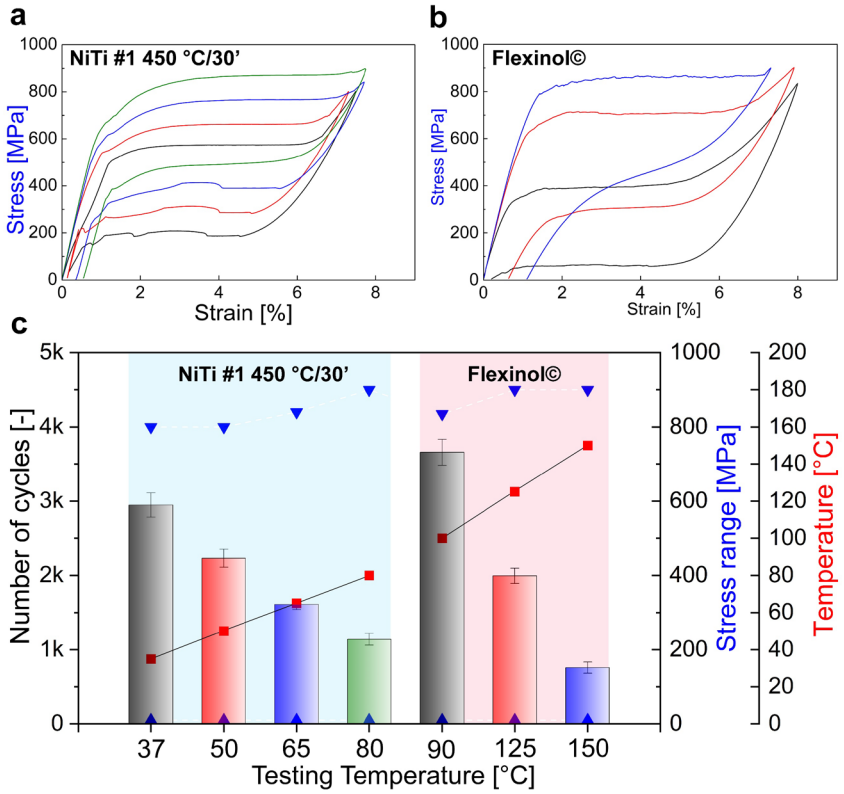

Figure 42: Effect of microstructure and chemical composition on the superelastic fatigue, represented by Ni-rich in a) and Ti-rich in b). Samples were cycled at progressively higher temperatures (above A_f), The corresponding evolution of the number of cycles until fracture on testing temperature for both compositions in c).

The results can be summarized as follows:

1. The number of cycles till failure correlates with plateau stress (the correlation with temperature is the only a consequence of the Clausius-Clapeyron equation).
2. Flexinol 90C wire display long fatigue life despite of the extreme instability of cyclic stress-strain response at high temperatures.

6.3 Effect of strain rate

Deformation via stress-induced martensitic transformation shall be insensitive to the strain rate. Nevertheless, experiments show that strain rate affects the cyclic superelastic response of NiTi SMA significantly. The strain rate sensitivity originates from latent heat generation/absorption and heat exchange with surrounding environment. NiTi wires cycled with high strain rates experience more adiabatic conditions compared to wires cycled with low strain rates. Consequently, the temperature of the wires oscillates upon cycling and the mean value increases with increasing strain rate [112]. The effect of strain rate is thus the same as the effect of test temperature dealt with in the previous chapter. We did not investigate the effect of strain rate systematically, nevertheless, Fig. 43 shows the results of the cyclic tensile test on NiTi wire annealed at 400 C for 30 min. at a constant temperature of 20 °C using two different strain rates with the same stress and strain limits.

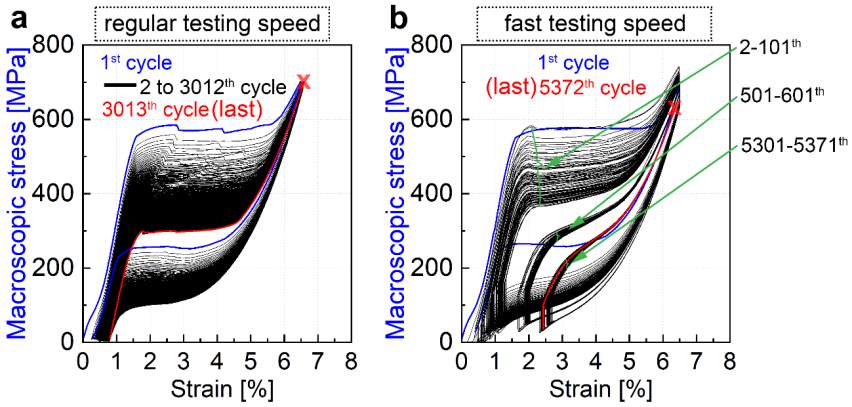

Figure 43: Effect of strain rate on the fatigue performance of NiTi SMAs for the strain rate values of 0.002 s^{-1} and 0.05 s^{-1} in a) and b), respectively. The last cycle is highlighted in red and the point of fracture by x.

The results can be summarized as follows:

1. Superelastic wire cycled at a constant room temperature of 20 °C using a low strain rate $\dot{\varepsilon} \leq 0.002\ s^{-1}$ displays a relatively low number of cycles until failure (~3000).
2. The wire cycled at a higher strain rate displayed higher instability of stress-strain response but a larger number of cycles until failure, most likely due to the gradual decrease of forward plateau stress upon cycling and consequent decrease of sample volume which undergoes a martensitic transformation.

6.4 Strain localization phenomena

As introduced in Chapter 5, NiTi wire deformed in tension tends to display localization of deformation in macroscopic Lüders band fronts moving along the length of the wire. This phenomenon affects the fatigue performance of NiTi in tension-tension partial cycling since the externally applied strain amplitude is multiplied by the strain localization phenomenon [55,106-108,111]. However, this is not the case in complete superelastic cycles. Whether strain localization affects the fatigue performance of NiTi in complete superelastic cycling, remains to be found out. Therefore, I paid special attention to the homogeneity/heterogeneity of tensile deformation in fatigue testing.

6.4.1 Strain localization in complete superelastic cycles

If strain localizes in macroscopic Lüders band fronts, we have to distinguish between nominal macroscopic strains and local strains. The nominal macroscopic stress-strain curves evolving during tensile cycling were recorded in fatigue tests (Fig. 44). Evolution of parameters introduced in Fig. 44a (residual strain (ε_{res}), upper plateau stress ($\sigma_{tr}^{A\to M}$) and lower plateau stress ($\sigma_{tr}^{M\to A}$), transformation hysteresis $\sigma_{hys} = \sigma_{tr}^{A\to M} - \sigma_{tr}^{M\to A}$) were evaluated and analyzed.

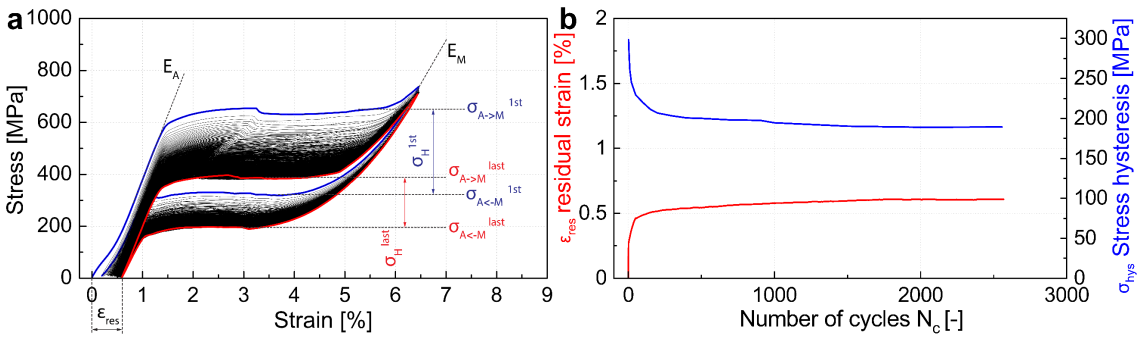

Figure 44: Schematic of SE cycling of NiTi#1 400°C/30' at 30 °C till failure with the evolution of hysteresis and plateau height. The blue corresponds to the first cycle and the red to the last 2557th cycle in a) and the evolution of the hysteresis and residual strain in b).

While the upper plateau stress $\sigma_{tr}^{A\to M}$ always decreases, lower plateau stress $\sigma_{tr}^{M\to A}$ may decrease, increase, or remain nearly constant, depending on the wire microstructure and test temperature, as shown in Fig. 40d. The decrease of upper plateau stress $\sigma_{tr}^{A\to M}$ upon cycling is due to plastic deformation accompanying stress-induced martensitic transformation leading to the build up of internal stress [20]. The evolution of lower plateau stress $\sigma_{tr}^{M\to A}$ is less understood, it is known to be linked to the evolution of residual strain ε_r, but the exact mechanisms are not very clear. Whether and how the observed

changes of stress-strain response are related to strain localization phenomena, microstructure evolution, and fatigue degradation remains to be investigated.

Tensile deformation of superelastically cycled NiTi depends on the virgin austenitic microstructure set by the cold work/heat treatment. Figs. 45a-h shows the temporal evolution of local strains (strain localization pattern) in a single superelastic cycle on 8 NiTi wires subjected to different heat treatments. Different heat treatments lead to different strain localization patterns. The samples heat treated at 350°C/05' and 10' (Fig. 45a-b) display a nearly homogeneous distribution of strain along the wire axis which corresponds to the lack of transformation plateau on the stress-strain curve. Heterogeneous strain distribution appears in the case of NiTi heat treated 350°C/30' (Fig. 45c) and the strain localization pattern gradually evolves with increasing heat treatment time (Fig. 45c-h). Let us point out that number of propagating fronts is at least twice as larger during reverse transformation than during the forward transformation.

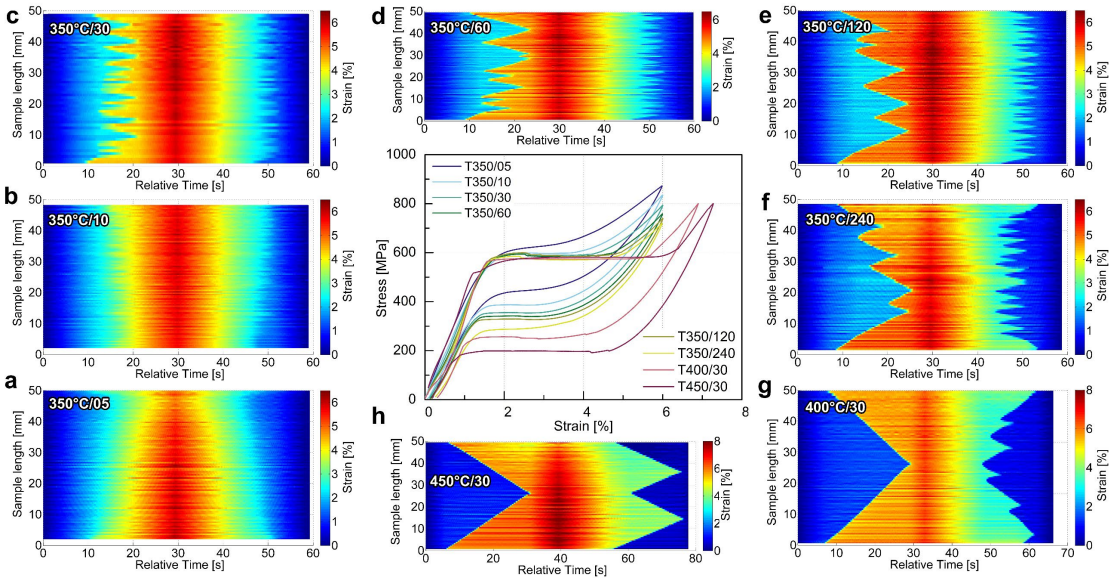

Figure 45: Schematic evolution of the localized response measured via DIC in NiTi#1 wires with different heat-treatments deformed at a constant temperature of 25 °C and strain rate of 0.002 s^{-1} in a-h) and in the corresponding stress-strain curves in middle.

It is obvious that strain localization is hindered by the lattice defects and internal stresses in samples heat treated at the lowest temperature/time (Fig. 45a-b). Since transformation strains are low and upper plateau stresses are high, these NiTi wires show poor fatigue performance. On the other hand, samples heat treated at 450°C/30' showing simple strain localization pattern display poor stability stress-strain curve evolving upon tensile cycling. Hence, fatigue experiments will be performed on NiTi wires given 400°C/30' heat-treatments or wires heat treated via a short electric power pulse [17,99].

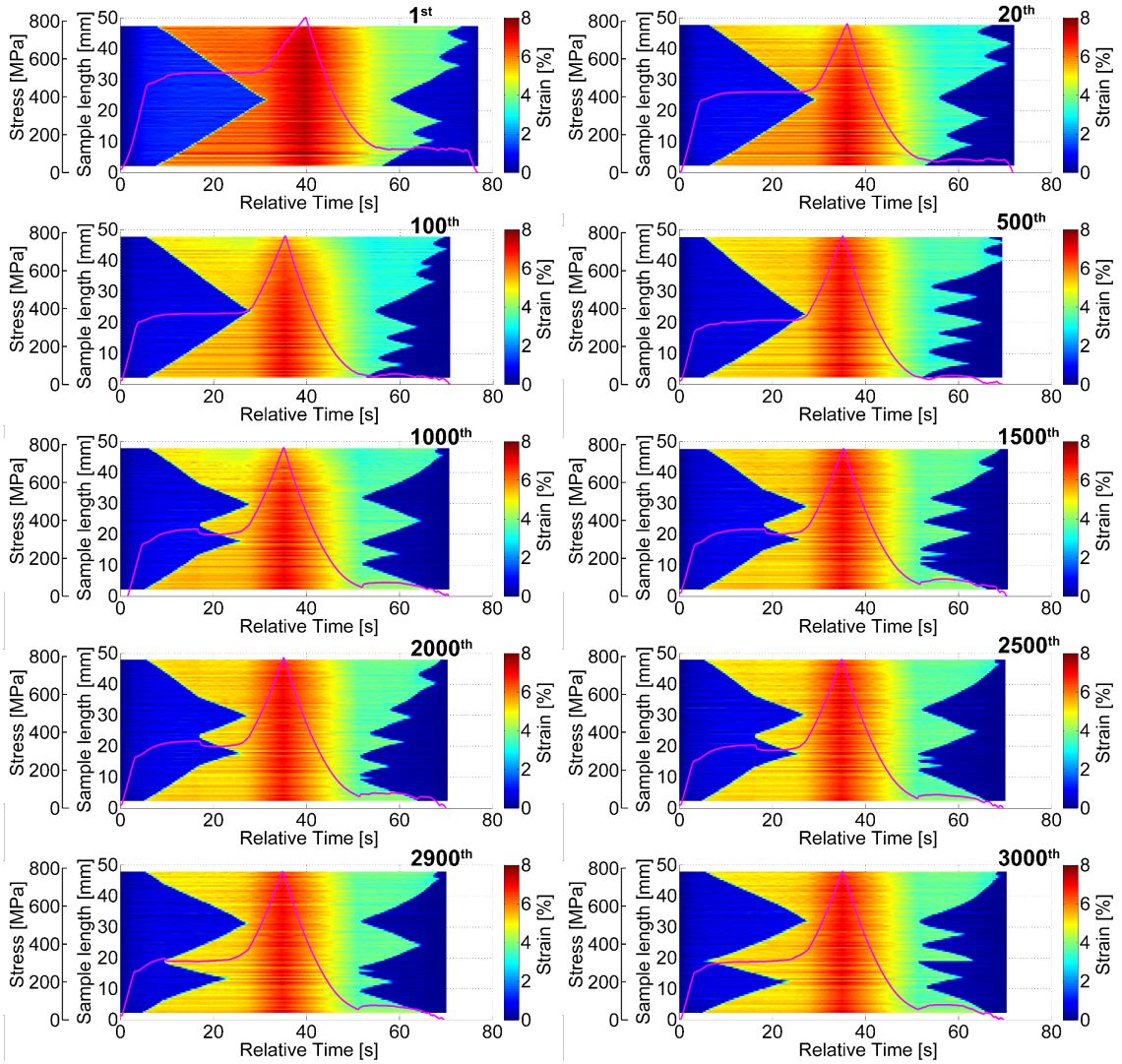

Figure 46: DIC strain maps of selected cycles during Full SE cycling of NiTi# 1 450°C/30' wire until fracture.

Fig. 46 documents how the strain localization pattern (NiTi#1, 450°C/30') evolves with an increasing number of cycles in a superelastic fatigue test. Stress-time curves are superimposed in pink color on the 1D-DIC record. Two Lüders band fronts nucleate in the capillaries and propagate toward the center of the wire where they meet. Strain localization pattern during the reverse unloading involves multiple Lüders band fronts. A decrease of transformation strain with the propagating front of about ~1 % is observed already after the 20th cycle. Transformation plateau stress decreases continuously upon cycling. This scenario persists up to around 1000 cycles when a new Lüders band front nucleates in the center of the wire. A stress drop accompanies the nucleation event. Upon further cycling, this new front nucleates earlier, otherwise the strain localization pattern remains approximately similar until fracture (around 2500 - 3000 cycles).

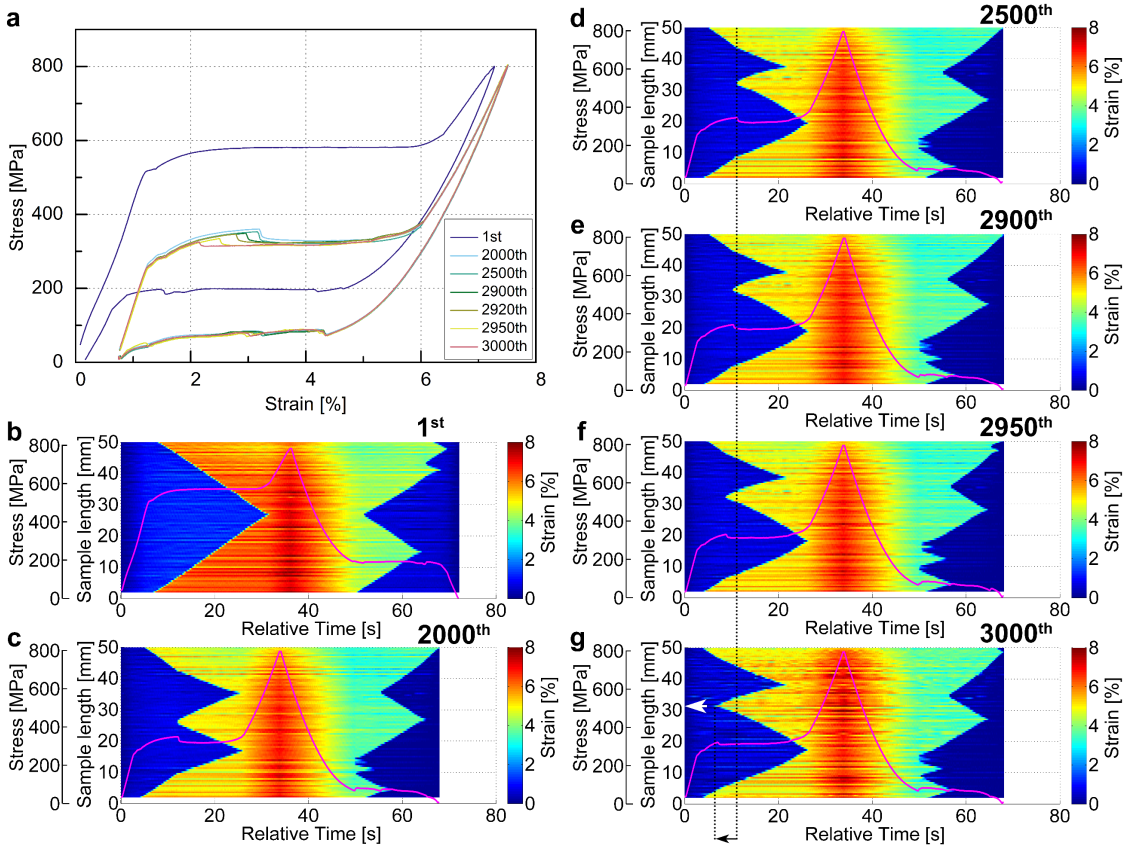

Figure 47: Full SE cycling of NiTi# 1 wire 450°C/30' with in-situ DIC tracking of local strains. In a) the selected stress-strain curves is plotted. In b)-g) the evolution of DIC maps is plotted, where the black and white arrow in g) highlights the evolution of the accelerated nucleation of the Lüders band.

The evolution of strain localization pattern upon tensile cycling reported in Fig. 46 invokes a question, of whether the observed change in strain localization pattern can be related to crack nucleation on the surface during the fatigue life. To answer this question, another cyclic tensile test was performed on the same NiTi#1 wire at a constant temperature of 35 °C (Fig. 47). Results are very similar, again new deformation band becomes nucleated around cycle 2000 in a location near the center of the wire and the nucleation starts earlier and earlier upon further cycling.

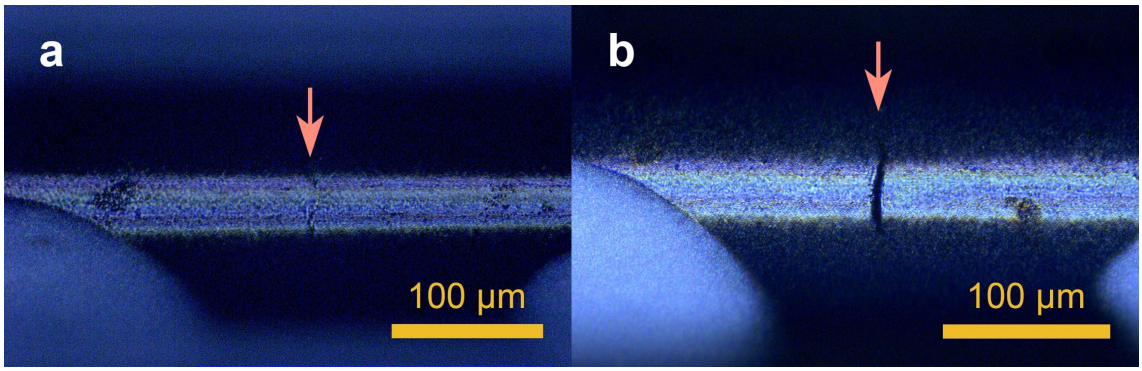

Figure 48: The light microscopy of NiTi# 1 wire 450°C/30' after superelastic cycling. The local area of interest investigated via DIC has shown the existence of propagating crack marked by the red arrow in close and open states in a) and b), respectively.

This observation was rationalized by assuming a new band front, which nucleated in the center of the wire, originates from a crack serving as a stress riser [55,129,130]. Therefore, tensile cycling was stopped after the 3000th cycle and the location of interest was observed in the light optical microscope (Fig. 48). Indeed, a small crack was located (Fig. 48a).

Then The specimen was shortened for in-situ SEM observation and cycled in tension using a micro tensile tester (DEBEN In-situ Microtest) till fatigue failure. The cycling was performed at a low strain rate of 0.0008 s^{-1} and the temperature at which the sample was cycled corresponds to the room temperature (air-conditioned at about 23 °C). As shown in Fig. 49a-d, the recorded crack propagation allowed us to evaluate the final stage of the crack propagation during the in-situ cycling (Fig.49e).

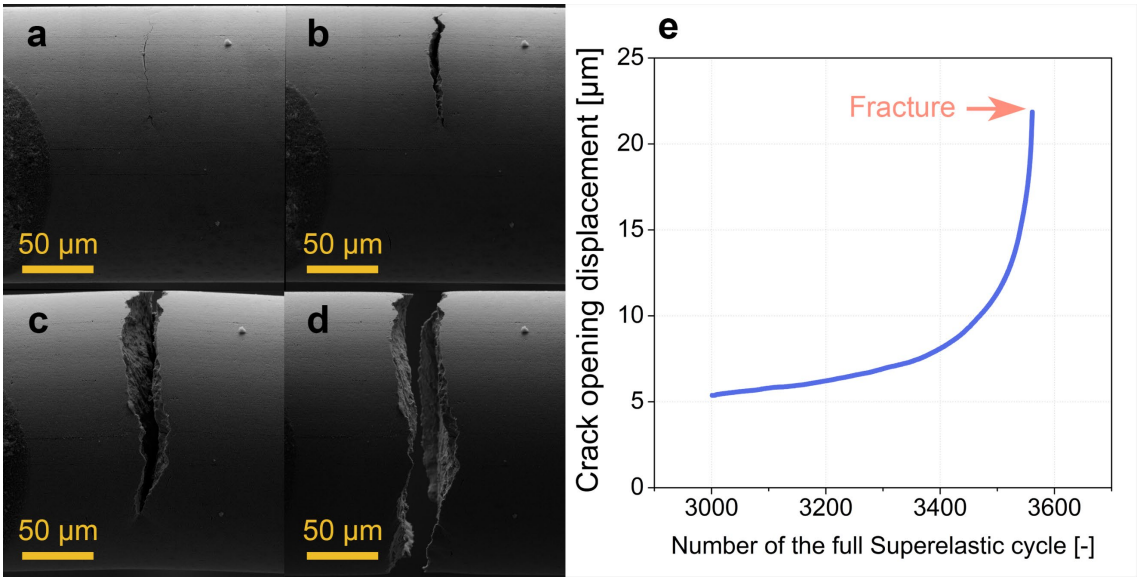

Figure 49: The crack detected via DIC due to the accelerated nucleation of the Lüders band on the NiTi wire after 3000 fatigue cycles in a), after loaded in the martensite in 3002 cycle in b), after cyclic loading in-situ in the SEM after additional 567 cycles in c), the sample fractured in fatigue after 3568 cycles in d) and the evolution of the crack opening during cycling is plotted in e).

Fractography analysis was performed on one of the fracture surfaces (Fig. 50). The crack initiation area was associated with a nonmetallic inclusion near the surface of the samples. It is not uncommon like in this case to observe the crevice, which remained after the inclusion falls off the sample. While the opening of the cracks of wire loaded in tension occurs in (mode I) loading conditions, some expected fracture surface features can be recognized. Fracture surface in the early stage of the crack propagation exhibit features of quasi-cleavage, highlighted in Fig. 50b. The propagation of fatigue crack is distinguishable via clear striations which are stable in earlier stages with relatively fine and uniformly distributed striations due to the slower crack growth and more pronounced and combined with dimples and tearing ridges in the later stage of the crack propagation

with the appearance of secondary cracking in Fig. 50c-d, respectively. Furthermore, it is possible to find inclusions in the matrix, especially in the dimple rupture formed by microvoid coalescence in Fig. 50e. It is worth mentioning that the existence of several macroscopic cracks on the same fracture surface shared with the magistral crack. In this case, at least five cracks were detected, and one of them is shown in Fig. 50f.

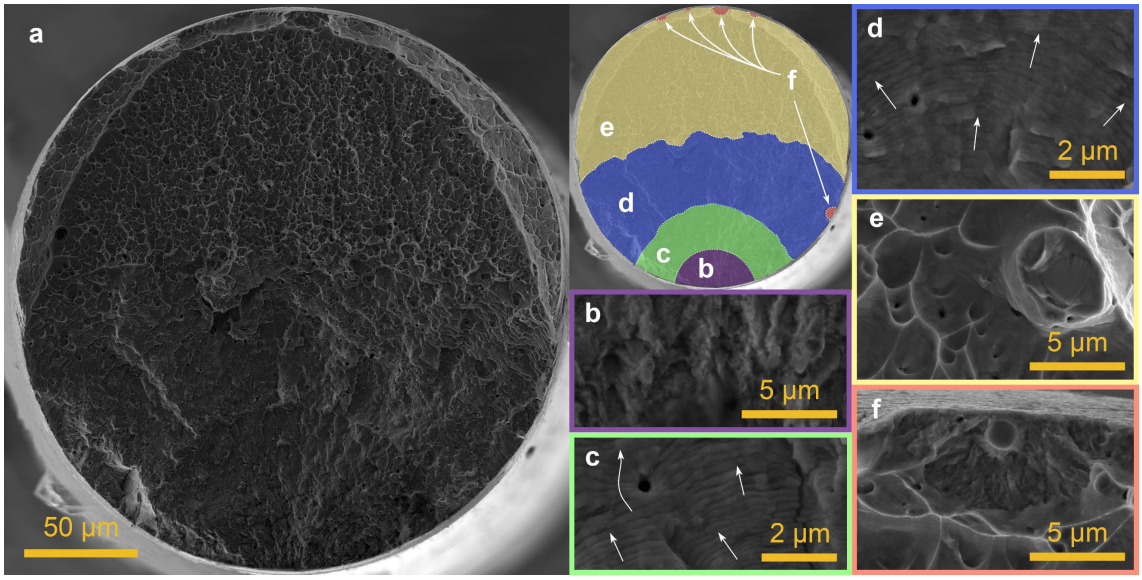

Figure 50: SEM image of the fracture surface of the NiTi#1 450°C/30' in a) complete area of the surface fracture of the wire with color highlighted areas with distinguishable areas with corresponding surface features in b) to f).

The following conclusions were obtained from the strain localization studies during the complete cyclic tensile test:

1. Tracking of the evolution of strain localization patterns upon tensile cycling via 1D-DIC can be used to detect crack nucleation sides and ultimately to predict where and when fatigue failure will take place.
2. Unpredictable strain localization patterns can be rationalized by assuming a random distribution of stress concentrators (nonmetallic inclusions) and temperature gradients in the tested wire.
3. Since the observed evolution of strain localization patterns during the fatigue life relates to functional degradation and damage accumulation, it might be utilized as a diagnostic method for failure detection and prediction (the location where the magistral crack leading to the fatal failure can be detected in about 75 % of fatigue life).

6.4.2 Strain localization in partial superelastic cycles

Results of partial superelastic fatigue cycling were already reported in section 4.2. It was found that smaller mean strain or strain (stress) amplitudes do not necessarily improve the fatigue life of NiTi wire samples loaded in cyclic tension. However, it was ascribed to strain localization phenomena and decided not to focus on partial cycles in fatigue studies. However, in this chapter focusing on strain localization phenomena, I will, for completeness, briefly report the results of dedicated investigations showing how strain localization affects the performance of superelastic NiTi#1 wires (450°C/30', d= 200 µm, 35 °C, strain rate 0.002 s^{-1}) subjected to partial superelastic fatigue tests in tension.

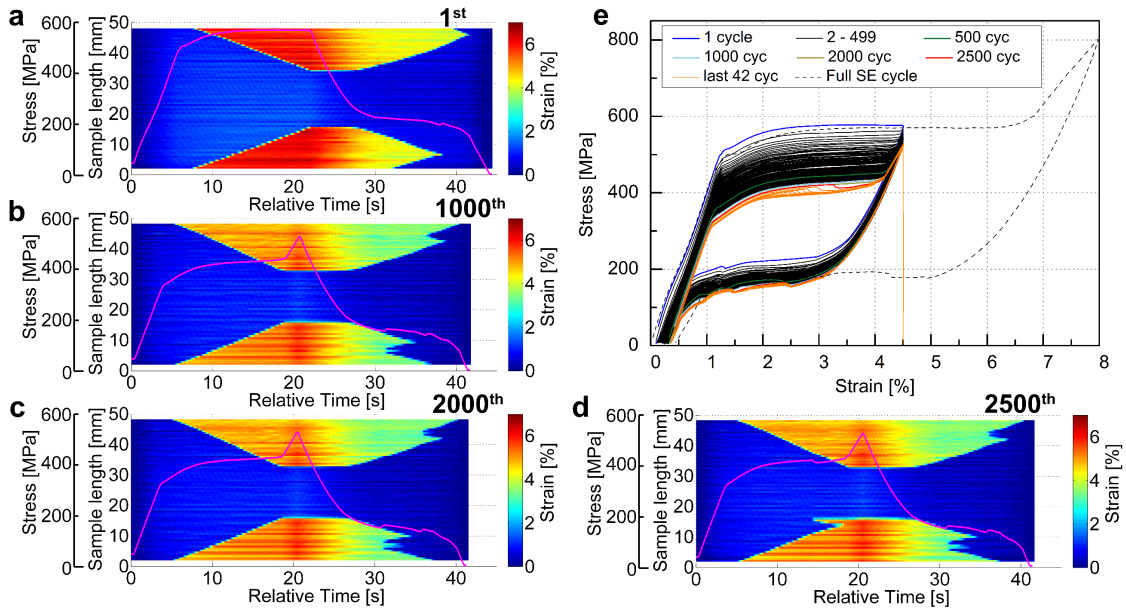

Figure 51: DIC observation of partial cycling of SE loaded wire in tension. DIC local strain maps in a) to d), in e) is the corresponding macroscopic stress-strain curves of testing.

Local strain maps presenting the evolution of strain localization patterns in the 1, 1000, 2000, and 2500 cycles are presented in Fig. 51a-d, and the corresponding macroscopic stress-strain curve in Fig. 51e. The crack nucleation site was detected at location z~ 15 mm before failure.

Fig. 52 presents the results of the 1D-DIC analysis of partial superelastic cycling. The wire was loaded up to 4.5 % strain (deformation was localized as in Fig. 51a) and then cycled in tension between 3.5 % and 4.5 % strain up to 6000 cycles. Figs. 52c, d, e show the evolution of strain localization patterns (blue color corresponds to 3.5 % strain) due to partial cycling. In the first cycle the wire deforms only around the location of the band front (Fig. 52c). However, upon further cycling this localization disappears and the wire deforms homogeneously everywhere. Following that, the wire was subjected to

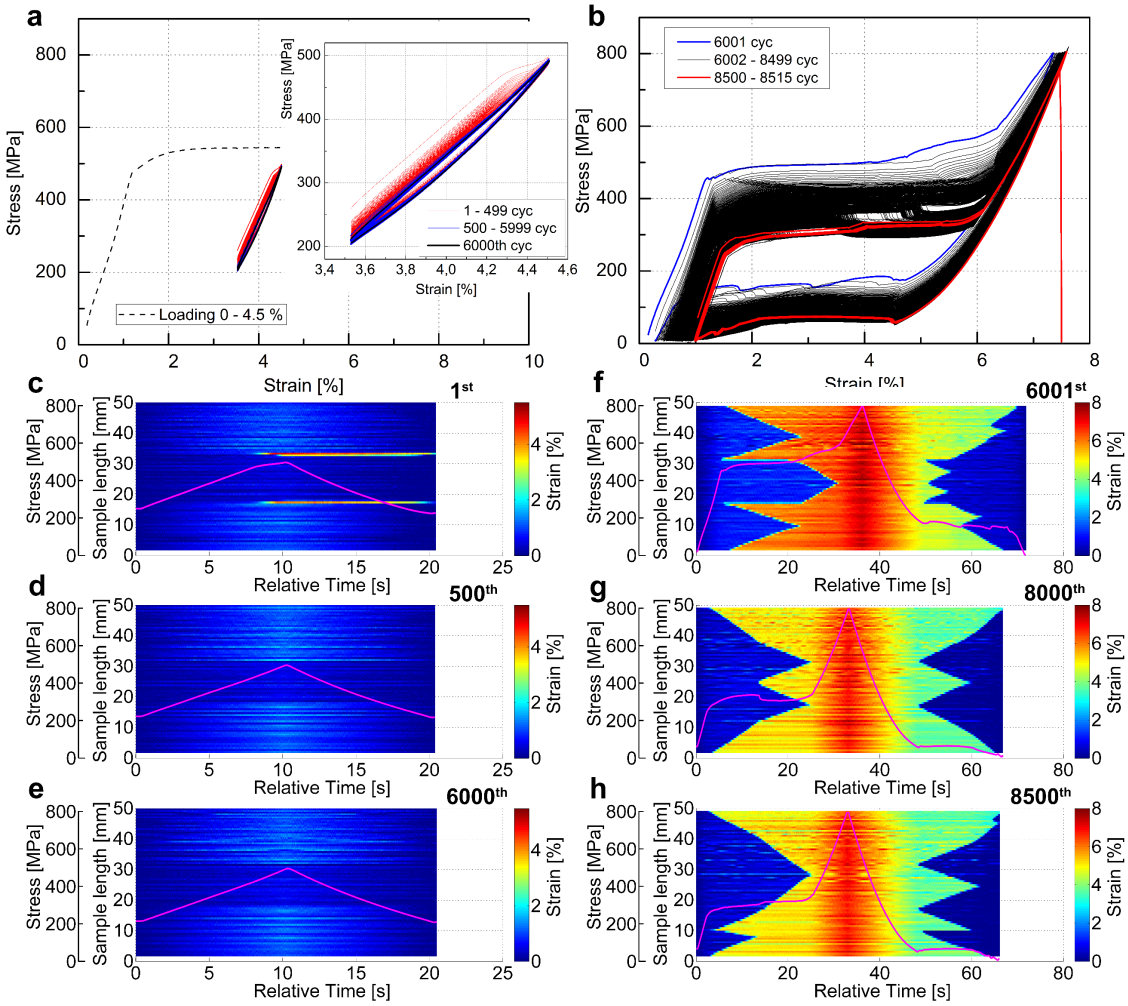

Figure 52: DIC observation of partial cycling of NiTi#1 450°C/30 wire in tension in limited partial strain between upper and lower plateau (a, c, d, e), and full cyclic loading and unloading in tension (20-800 MPa) after 6000 partial cycles in {b, f, g, h). The wire fractured after 8515 cycles (i.e., 2515 full superelastic cycles).

complete superelastic cycling (Fig. 52b). Despite 6000 cycles, "the wire did not forget" the locations where partial cycling started since the new band front nucleated exactly there (Fig. 52f). Upon further cycling up to 8500 cycles, however, these locations were forgotten, strain localization patterns evolve, and the wire finally fractures at location z-10mm (Fig. 52h), where band front nucleates in cycle 8500.

Another example of partial superelastic cycling is presented in Fig. 53. The test starts with loading the wire until the end of the stress plateau (Fig. 53a). Then, tensile cycling is performed in the strain range of 5-6 % up to cycle 499. Following that, the wire is unloaded and the 500th cycle is performed as a complete loading-unloading until the end of the stress plateau. The strain localization pattern (Fig. 53b) did not change from the first cycle.

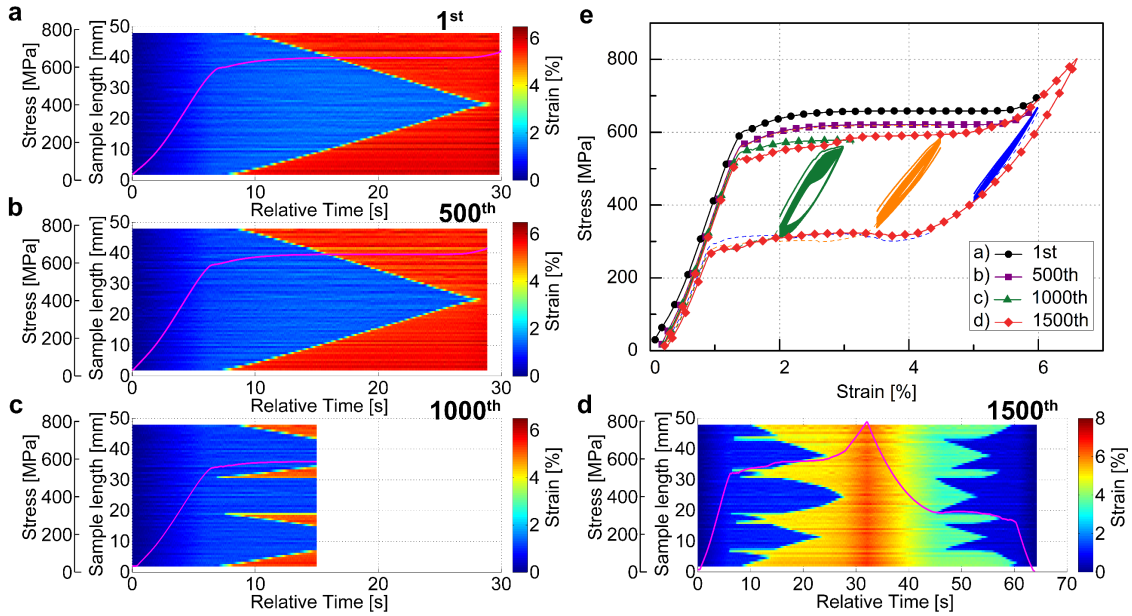

Figure 53: Schematic of affected localization via cycling at the SE plateau a) in strain range windows of 5-6 %, 3.5-4.5 %, and 2-3 %. The local strain maps represent the response after such constrained cycling (5-6 %) 500th in b), (3.5-4.5 %) 1000th c), and full SE cycle after (2-3 %) 1500th cycle in d).

The following conclusions were obtained from the strain localization studies during partial cyclic tensile tests:

1. In the case of partial superelastic cycles, the material deforms (transforms) only in locations of the wire, where Lüders band fronts move upon tensile cycling (Fig. 51).
2. Plastic deformation accompanying stress-induced martensitic transformation in locations, where the Lüders band front move, generates lattice defects and internal stress in the wire microstructure which evolves upon cycling, while locations where the band fronts do not move remain unaffected. Because transformation plateau stress decreases upon cycling, strain tends to remain localized in locations, where the Lüders band front moves (Fig. 51).
3. Strain localization phenomena drastically affect the performance of superelastic NiTi wires in partial superelastic cyclic tests. Depending on the mean strain and strain amplitude, the externally imposed strain either delocalizes (Fig. 52c, d, e) or remains localized (Fig. 53c, d, e) during the partial superelastic cycling. Of course, this significantly affects fatigue lifetime since the local strain amplitude is ~1 % in the former case and ~6 % in the latter case.

6.4.3 Strain localization in superelastic cyclic tests with overloading

Experimental results reported in Chapters 6.4.1 and 6.4.2 demonstrate the impact of strain localization phenomena on NiTi fatigue. Key problem is that localized strain tends to be locked in locations where Lüders band fronts move upon tensile cycling which leads to acceleration of the accumulation of damage (nucleation and growth of cracks) in those locations where local strain amplitudes are significantly larger that the externally imposed strain amplitudes.

While searching for a possible strategy how to suppress this effect of strain localization, we decided to try to modify the microstructure in locations where Lüders band fronts move by overloading the wire up to larger strain (stress) periodically during the tensile cycling. There are three important parameters of the overloading cycles: i) frequency of overloading cycles, ii) maximum and minimum (stress) strain reached during the overloading, and iii) the number of elastic cycles in an overloaded state.

Figure 54 shows the results of the strategy which finally turned out to be successful. A partial superelastic fatigue test was performed as follows: 1) the wire was

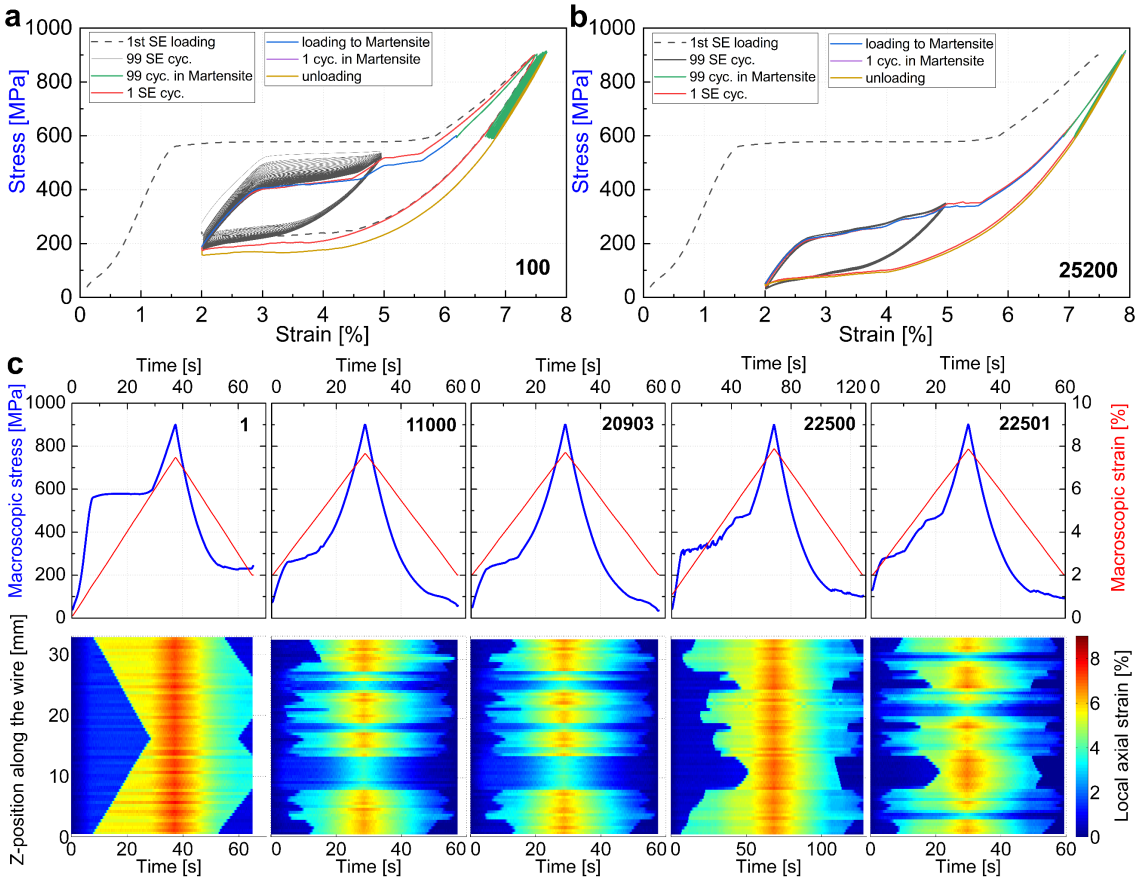

Figure 54: Effect of overloading cycles in martensite on the fatigue of superelastic NiTi#1 400°C/30'. The evolution of the first 100th partial cycles in a), the response after 25200 partial cycles and 25200 overloading cycles in b), and the evolution of local axial strain during selected cycles in c) at constant temperature 20 °C and strain rate 0.002 s^{-1}.

subjected to 99 cycles between 2-5 % of strain, 2) overloaded to 900MPa 3) subjected 100th cycles between 600-900 MPa (elastic loading of martensite) 4) unloading back to the lower strain limit to the reverse transformation plateau and 5) subjected to 99 cycles between 2-5 % of strain again. In a such way, the cycling was repeated until the fracture. Partial superelastic fatigue test by tensile cycling between 2-5 % strain continuously until fracture was performed for comparison. The experiments were performed on NiTi#1 400°C/30' wire at a constant temperature of 20 °C using a constant strain rate 0.002 s^{-1}.

While the number of cycles until fracture in continuous cycling was ~ 3000 cycles, the wire tested with periodic overloading in martensite fractured at 23660 cycles (Fig.55). This is a very significant improvement, which shall be confirmed statistically and the origin of which shall be explained. If confirmed, the phenomenon may be easily used in engineering applications to improve the fatigue lifetime of NiTi components.

In my opinion, the physical origin behind this improvement is based on an assumption that periodic overloading of the cycled wire in a fully martensitic state at large stress results in plastic deformation around crack tips (stress concentrators in fully martensitic wire). The selective plastic deformation of the material surrounding crack tips will cause crack blunting and slow down their growth during subsequent tensile cycling.

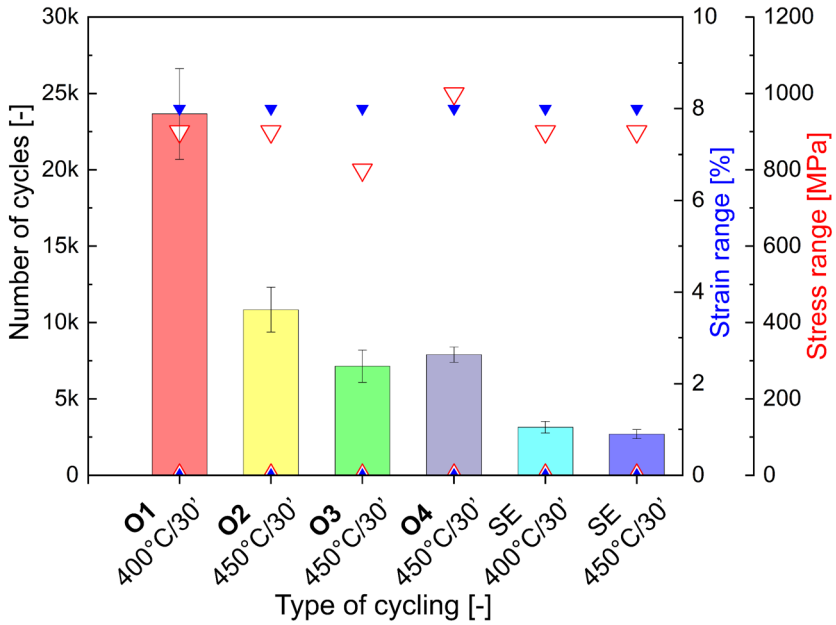

Figure 55: Number of partial superelastic cycles until failure of superelastic NiTi#1 400°C/30' and 450°C/30' during tensile cyclic loading-unloading at constant temperature 20 °C (O1-O4) and without applied overloading cycles in martensite.

The following conclusions were obtained from the investigation of the effect of overloading on the fatigue of NiTi:

1. Periodic overloading of superelastically cycled NiTi wire may result in a significant increase in fatigue life.
2. There are multiple characteristics of overloading the impact on which fatigue life must be investigated including maximum stress(strain), number of overloading cycles, mean strain and amplitude of overloading cycles, and frequency of overloading.
3. The parameters of overloading cycles have to be adjusted based on the virgin annealing microstructure of the wire.

6.5 Fatigue of superelastic NiTi wires in tension with adaptive limits

The experiments reported in the previous chapter were performed on superelastic NiTi #1 wires heat treated in an environmental furnace because this is a standard method applied in the field to heat treat NiTi. However, I also use NiTi wires prepared by heat treatment of the same cold-drawn wires by a short pulse of electric power (see Chapter 4). The advantage of the Joule heating method is that NiTi wires with desired microstructure and functional properties can be prepared and used as model materials to investigate the effect of microstructure in NiTi experiments (see e.g., Chapter 5.3). These wires have slightly different microstructures than wire heat treated in the electrical furnace (small, recrystallized grains without lattice defects, no Ti_3Ni_4 precipitates).

As an example, Fig. 56 shows the results of the 1D-DIC analysis of the cyclic superelastic fatigue test on 14 ms NiTi wire cycled in tension at 20 °C until failure in the 11870^{th} cycle. The wire was cycled between 20 MPa and 7.6 % of strain. The stress-strain curves evolve dramatically upon cycling (Fig. 56a), transformation plateau stress decreases (Fig. 56d), residual strain accumulates, and stress hysteresis reduces from 250 to 100 MPa. The plot of accumulated residual strain in dependence on the number of cycles (Fig. 56b), shows that most of the residual strain accumulates in the first 200 cycles. The strain localization pattern does not evolve upon cycling (Fig. 56c), only the value of the strain localized within the moving Lüders band front decreases, which is in accord with the gradual shortening of the length of the stress plateau (Fig. 56e).

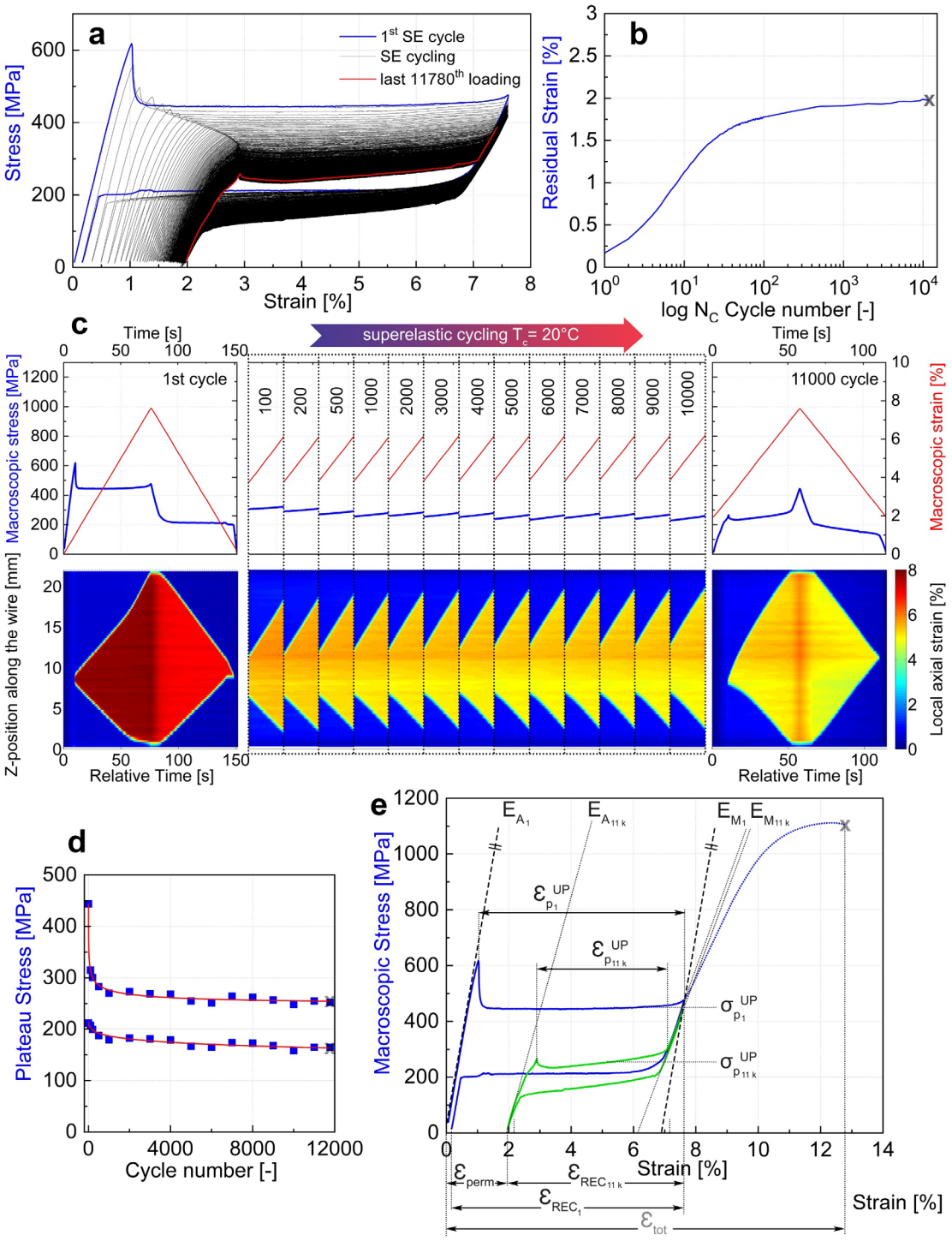

Figure 56: The macroscopic stress-strain curves during superelastic cyclic loading-unloading in tension at 20 °C util failure during 11781 loading in a), b) evolution of residual strain on the number of cycles, c) 1D-DIC record of the testing, the cut-out parts follow the evolution of the local strain on the upper plateau, d) The evolution of forward and reverse transformation plateau during cyclic loading-unloading until failure, e) the stress-strain curves in first and 11000 cycles with the evolution of upper plateau strain ε_p^{UP}, the difference of elastic modulus before and after cyclic loading-unloading for the B2 and B19' phases and decrease of transformation plateau σ_p^{UP}. The fracture is marked by x.

The idea explored in the research reported in this chapter is based on the finding that the stress, at which forward and reverse martensitic transformation proceeds might affect the type and density of lattice defects, accumulated residual strain, and ultimately

the number of cycles till failure. If this is true, NiTi wire cycled in tension under low plateau stress shall display enhanced fatigue lifetime. The easiest way how to decrease plateau stress is to decrease test temperature. However, the wide stress hysteresis of NiTi #1 wire (250 MPa) does not allow to decrease the test temperature below 0 °C (stress-strain response will become irreversible on loading-unloading). Another option is to perform a tensile test with an adaptive upper-stress limit, as shown in Figs. 57, 58.

In order to explore this idea, tensile tests were performed with adaptive upper strain limit at two test temperatures: 20 °C (Fig. 57) and 10 °C (Fig. 58). In contrast to the test in Fig. 80, tensile cycling was performed between of 20 MPa and the end of the upper plateau stress in such a way that the upper strain (stress) limit was gradually adjusted so that the wire deformed cyclically only up to the end of the stress plateau. The strain localization pattern was evaluated by DIC after the number of cycles denoted in Figs. 57a, 58a. The results are shown in Fig. 59.

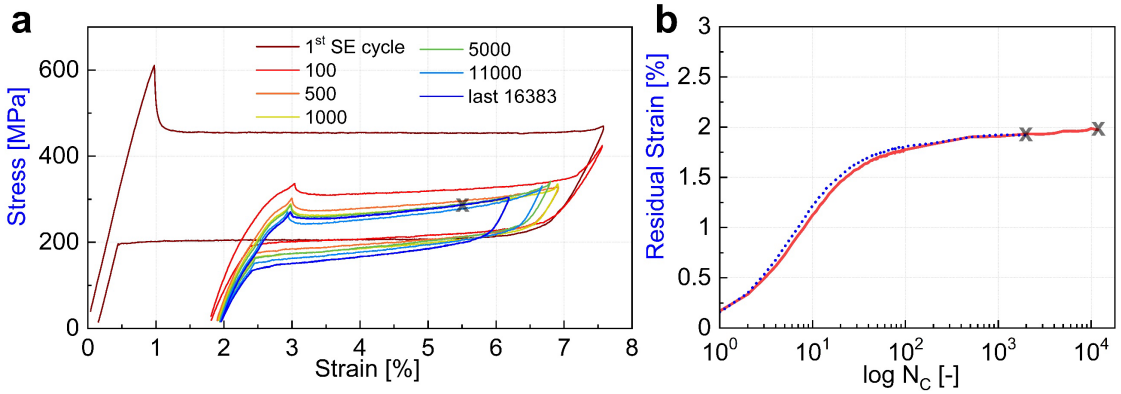

Figure 57: The selected macroscopic stress-strain curves during superelastic cyclic loading-unloading in tension at 20 °C util failure with adaptive maximum stress and strain in a), b) evolution of residual strain on the number of cycles with adaptive maximum stress and strain limits (red) and with fixed strain limits (blue). The fracture is marked by x.

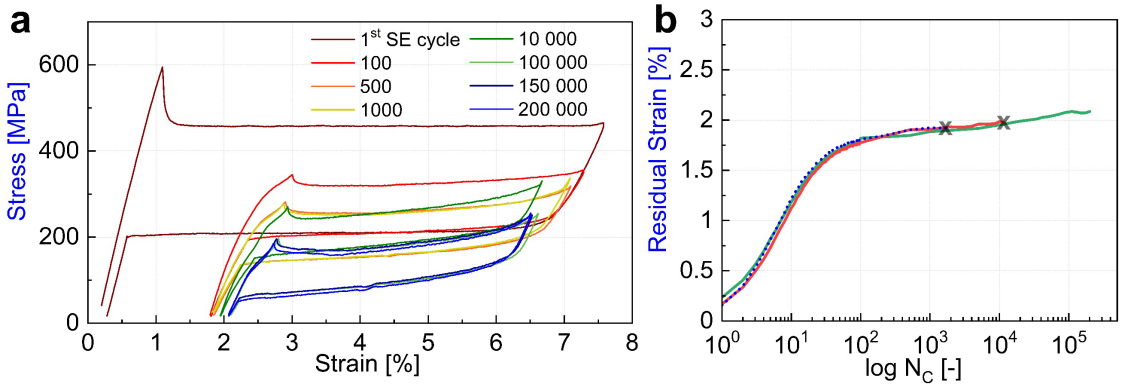

Figure 58: The selected macroscopic stress-strain curves during superelastic cyclic loading-unloading in tension at 10 °C with adaptive maximum stress and strain in a), b) evolution of residual strain on the number of cycles with adaptive maximum stress and strain limits (red) and with fixed strain limits (blue) at 20 °C and at 10 °C (green). The cyclic deformation was stopped by the operator after 200 000 loading-unloading cycles.

It is found that the application of adaptive test control resulted in an increase of the number of cycles until failure from 11000 (Fig. 56) to 16383 (Fig. 57), which is ~39 % increase in lifetime. This was promising, but not really a breakthrough. Breakthrough was achieved in the test with adaptive control performed at a lower temperature of 10 °C (Fig. 58), in which the wire did not fracture up to 200000 cycles. This is probably due to the fact that, the martensitic transformation proceeds at stresses for most of its fatigue life, which are significantly lower (~ 300 MPa at 20 °C and 200 MPa at 10 °C).

Strain localization pattern evolving during the tensile test at 10 °C in denoted cycles (Fig. 59) shows marginal changes between 100-10000 cycles. It remains almost unchanged between 100000 and 200000 cycles. Similarly, the stress-strain curve changed only marginally (except for the decrease of transformation stresses between 100000 and 150000). This can be taken as evidence for negligible accumulation of lattice defects and marginal accumulation of damage on the surface during tensile cycling.

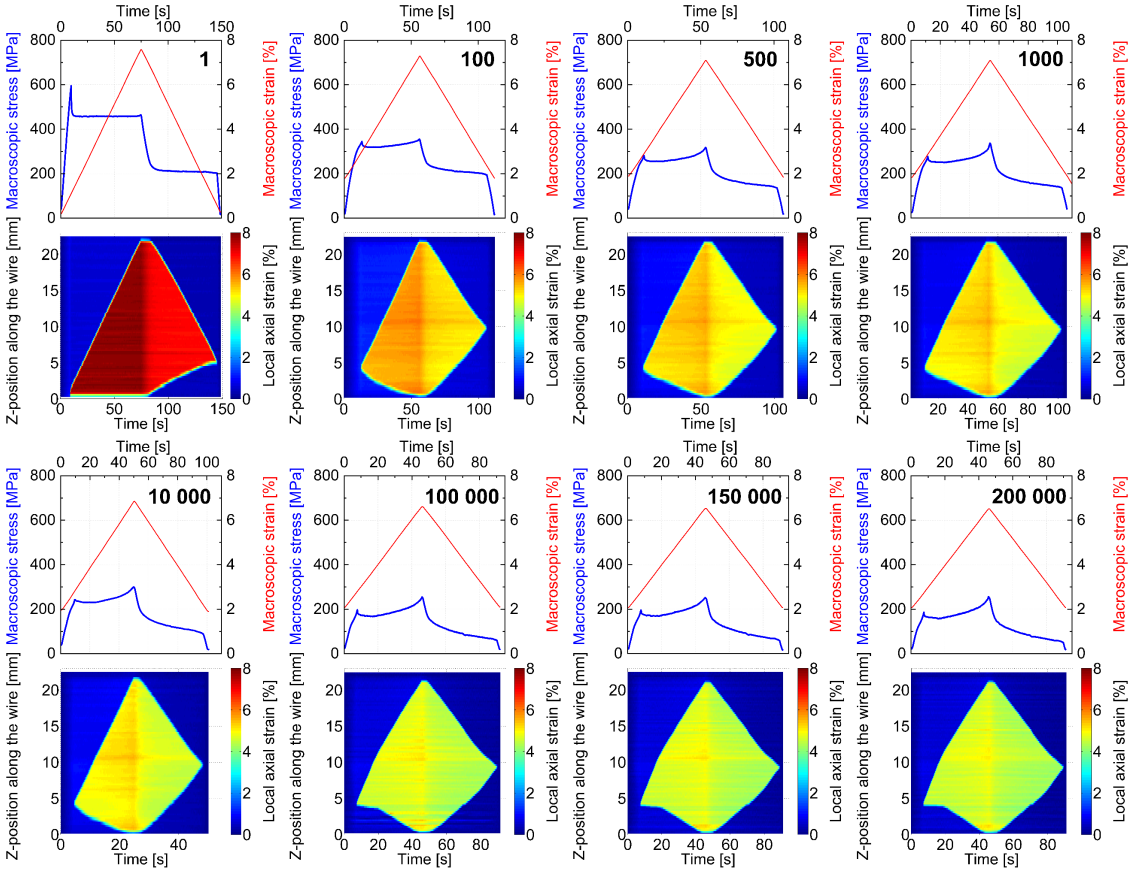

Figure 59: The 1D-DIC record of local axial strain for cycles 1, 100, 500, 1000, 10 000, 100 000, 150 000, and 200 000 during superelastic cyclic loading-unloading in tension at 10 °C with adaptive maximum limits in strain (stress). The test was stopped after 200 000 cycles by the operator.

To obtain supplemental information on lattice defects generated by the cyclic martensitic transformation in tensile tests at temperatures 20 °C and 10 °C, TEM lamellae were cut from deformed wires. In the case of the wire deformed at 20°C, one lamella was

cut from the middle part of the fractured wire (Fig. 60a, b, c), and a second lamella from close proximity (~ 100 µm) of the fracture surface (Fig. 60d, e, f). In the case of the wire deformed at 10°C, one lamella was cut from the middle part of the fractured wire (Fig. 61a, b, c).

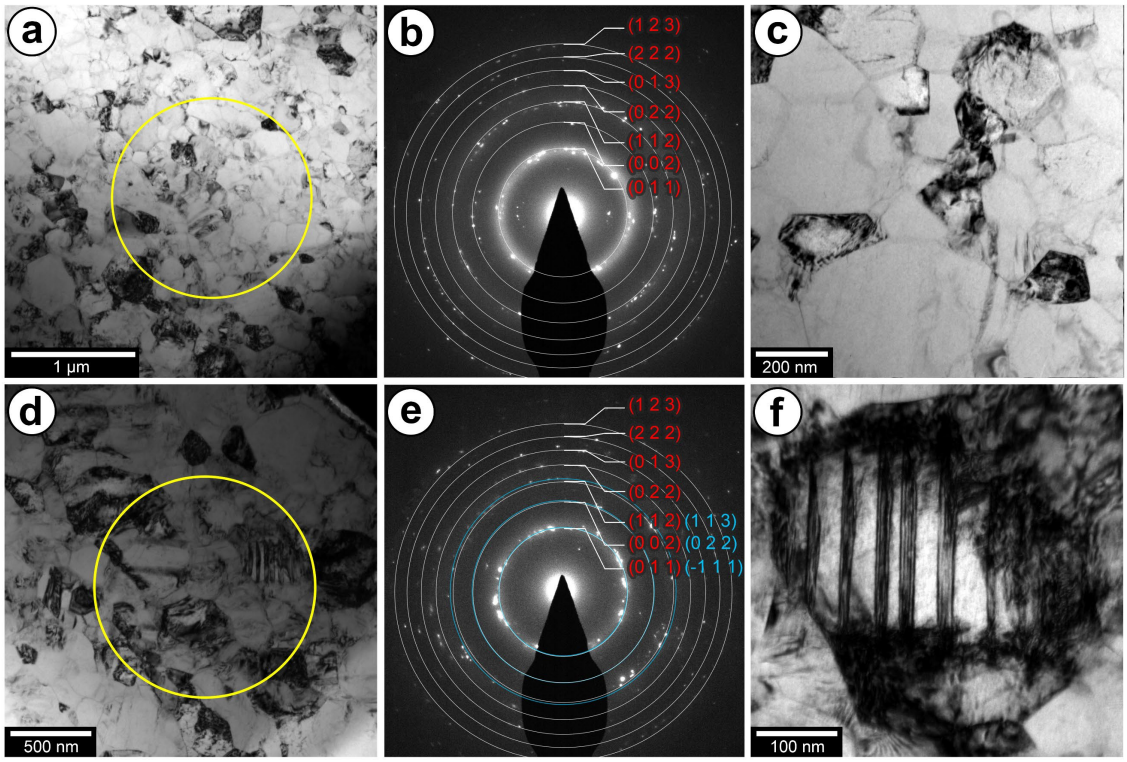

Figure 60: TEM bright field images of 14 ms superelastic NiTi wire cycled in tension at 20 °C with adaptive limits in maximum stress and strain after the fracture. TEM lamella from the fractured sample (same as in Fig. 57), far from the fracture surface (a, b, c) and close to the fracture surface (d, e, f). b) and e) represents diffraction pattern from the denoted SAED area in a) and d).

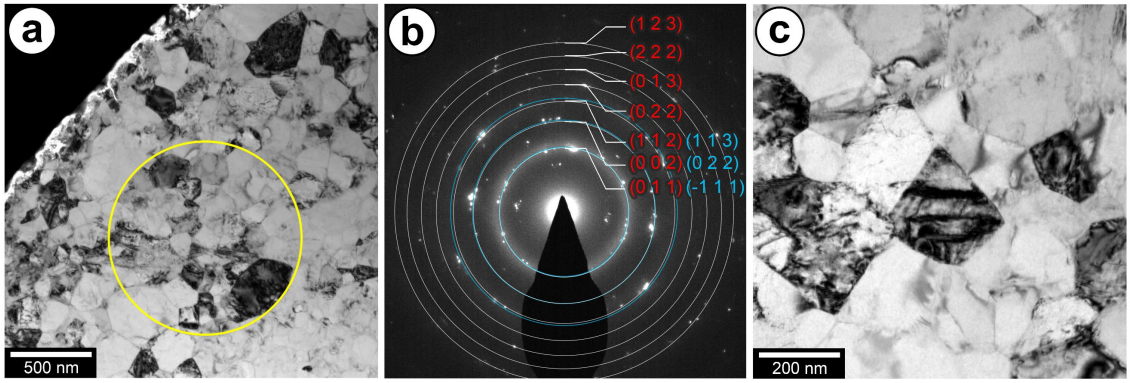

Figure 61: TEM bright field images of 14 ms superelastic NiTi wire cycled in tension at 10 °C with adaptive limits in maximum strain (stress). TEM lamellae from the cycled sample after 200000th superelastic cycles (same as in Figs. 58, 59). b) represents the diffraction pattern from the denoted SAED area in a). In c) one of the uncommon grains consisting of deformation twins.

It was found that, far from the fracture surface (Fig. 60a-c, 61c), the deformed wire was austenitic with a relatively low density of lattice defects. The observed lattice defects are relicts of the plastic deformation accompanying the cyclic forward and reverse martensitic transformation which remained in the austenitic microstructure [99,110].

These are mostly slip dislocations and rarely isolated deformation bands. Closer to the fracture surface, the microstructure contained a significantly higher density of slip dislocations and deformation bands in some grains.

6.6 Fatigue of superelastic NiTi flat dog-bone sheets

6.6.1 In-situ 2D-DIC experiments on NiTi flat dog-bone

Up to now, the application of the 1D-DIC method to evaluate strain localization pattern – time evolution of spatially localized axial strains - during tensile tests on NiTi wires was widely discussed. The 1D-DIC method is appropriate for NiTi wires since the cone-shaped Lüders band front in the case of NiTi wire [20] is observed on the surface as a temper propagating along the length of the wire during the tensile tests. In the case of flat NiTi ribbons or sheets, however, Lüders band front takes the form of a plate inclined to the load axis. Because of that, it is advantageous to follow the evolution of all three in-plane strain components on the flat surface by the 2D-DIC method, which is much more common in the literature. Such studies were frequently performed in the literature in the last 20 years [113-118] probably because they provide attractive results in pictures and new videos. I did also such experiments as well, but since flat samples are not suitable for fatigue tests, the results are not included in this thesis. The experiments reported below focus on the application of the 2D-DIC method to analyze the effects of stress concentrators on the cyclic tensile deformation of flat superelastic ribbons.

Superelastic NiTi flat samples were laser cut from 100 μm thin superelastic NiTi sheet into the shape of a dog bone. All samples had the same microstructure (i.e., the same cold work/heat treatment performed by the supplier) with a grain size of ~ 22 μm. The transformation temperatures in stress-free conditions were determined by DSC as A_f= 1, A_s= -13, M_f= -96, and M_s= -75 °C. The samples were deformed in cyclic tension at room temperature.

When strain and strain rate is referred to in the following text, it is the average macroscopic axial tensile strain evaluated by the position sensor of the tensile tester. On the other hand, local axial strains, and strain rates along the gauge length (axial strain components) evaluated by the 2D-DIC method are referred to as local strain and local strain rates, respectively. The sensitivity with which the local strain is evaluated may slightly vary based on the used hardware and used patterning of the surface.

6.6.2 Uniaxial cycling of superelastic NiTi flat dog-bone

The Superelastic stress-strain curve of NiTi flat samples at room temperature (Fig. 62a) displays similar transformation strains but lower transformation plateau stress than the NiTi #1 wire used in previous experiments. Upon tensile cycling till the end of the plateau, the transformation strain decreased from ~ 6.3 % in the first cycle to ~ 4.4 % in the 400th cycle.

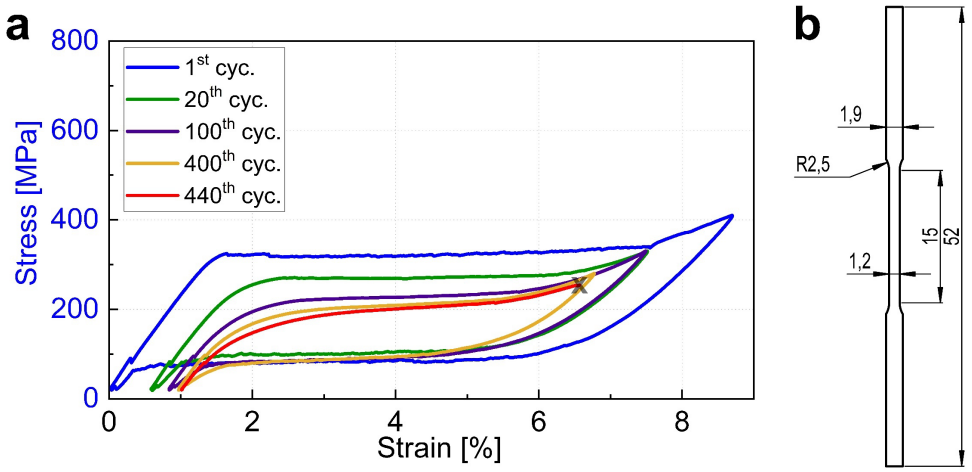

Figure 62: The macroscopic stress-strain curves during uniaxial cyclic loading-unloading in tension at 20 °C and strain rate of 0.001 s^{-1} till failure in a). In b) detailed drawing of laser cut shape of the sample from 100 µm thick SE NiTi sheet. The fracture occurred during loading in the 440th cycle and is marked by X.

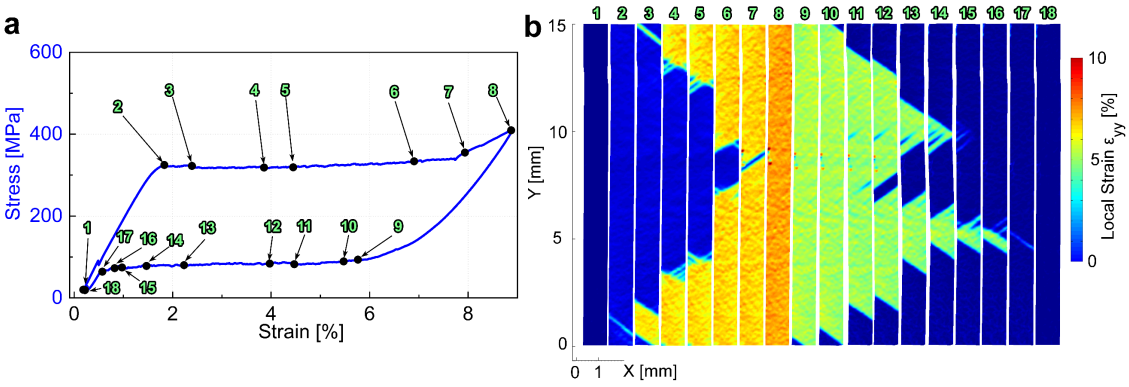

Figure 63: The macroscopic stress-strain curves during first SE loading-unloading in tension at 20 °C in a), with selected points on the macroscopic stress-strain curve corresponding to the local strain full-field DIC maps in b).

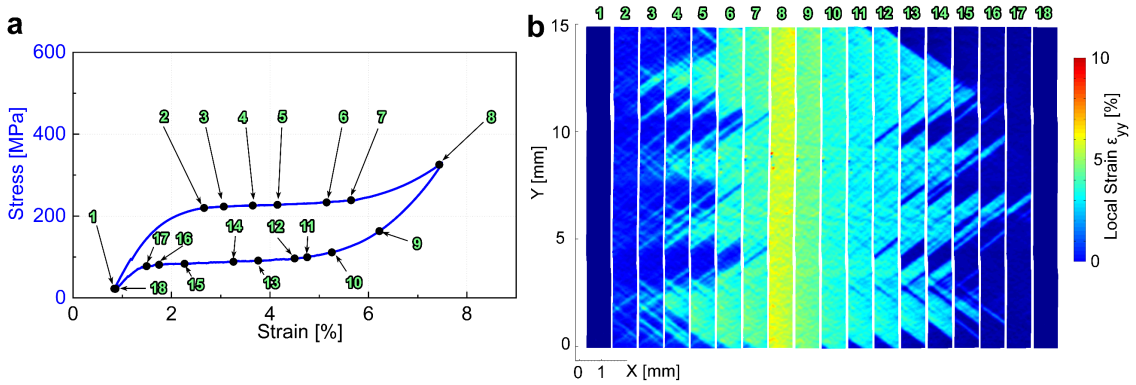

Figure 64: The macroscopic stress-strain curves during 100th SE loading-unloading in tension at 20 °C in a), with selected points on the macroscopic stress-strain curve corresponding to the local strain full-field DIC maps in b).

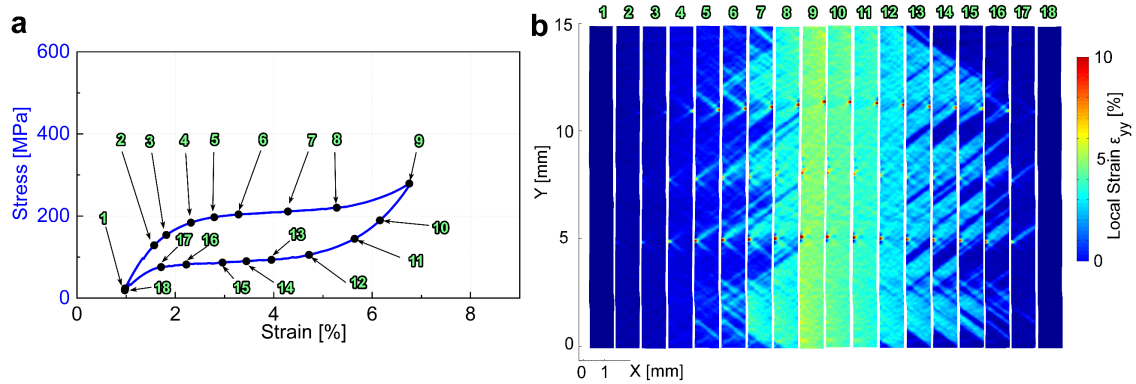

Figure 65: The macroscopic stress-strain curves during 400th SE loading-unloading in tension at 20 °C in a), with selected points on the macroscopic stress-strain curve corresponding to the local strain full-field DIC maps in b).

Strain localization patterns evolving in the 1st, 100th, and 400th tensile cycles are shown in Fig. 63,64,65, respectively. In the first tensile cycle (Fig. 63), Lüders band fronts nucleate as thin plates near the grips at the yield stress and grow towards the center upon tensile loading until they merge at the end of the transformation plateau in strain state 7, which is similar to the strain localization pattern of the NiTi #1 wire. Reverse transformation on unloading starts by nucleation of Lüders band front at the grips and their propagation towards the center. Strain localization patterns during the first forward loading and reverse unloading are thus again different.

In the 100th cycle (Fig. 64), the first Lüders bands are observed only at 2.7 % strain (strain state 2). Since 2.7 % strain cannot be elastic, stress-induced martensitic transformation proceeds homogeneously until this strain. This is supported by the homogeneous strain recorded by the DIC. The number of nucleated bands increases in states 3,4 but does not grow massively (band fronts do not move) until the strain state 5, which already corresponds to 4 % strain. Reverse transformation on unloading is

homogeneous from the peak strain at 7.5 % strain down to 5 % and then a large number of Lüders bands are nucleated.

In the 400th cycle (Fig.65), first Lüders bands are again observed only at 2.7 % strain (strain state 5) and the strain localization pattern is quite similar to that observed in the 100th cycle.

6.6.3 Uniaxial cycling of superelastic NiTi flat dog-bone with notch

In order to investigate the effect of geometry, a single notch was cut into the flat sample, as shown in Fig. 66b. Fig. 66 shows the evolution of the stress-strain curve recorded during cyclic loading-unloading of the notched sample in tension under the same test conditions as in the tensile test in Fig. 62. Stress is higher because the reduced cross-section was used to calculate stresses. The cyclic stress-strain response of the notched sample is not much different from that of the original flat sample.

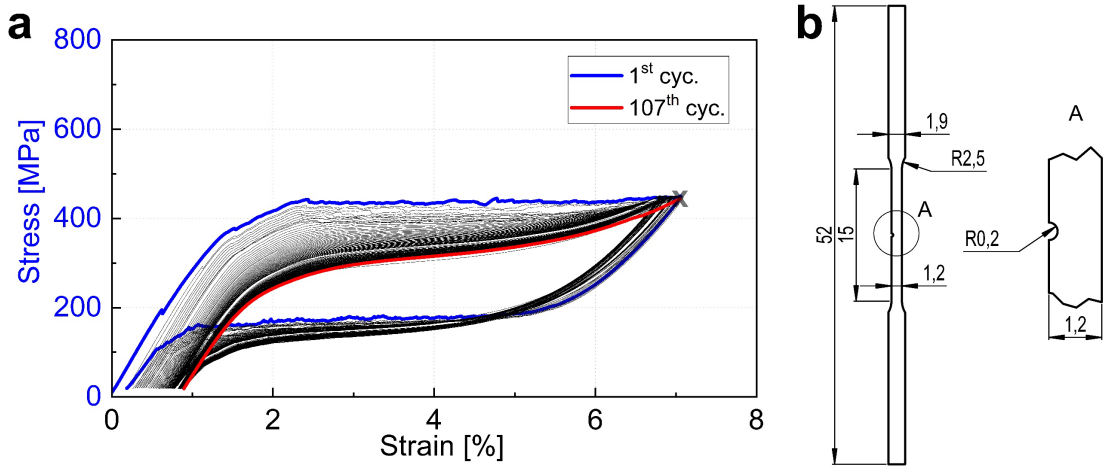

Figure 66: The macroscopic stress-strain curves during uniaxial cyclic loading-unloading in tension at 20 °C and strain rate of 0.001 s^{-1} till failure in a). In b) detailed drawing of laser cut shape of the sample from 100 µm thick SE NiTi sheet with a notch. The fracture occurred during loading in 107th cycle and is marked by X.

Strain localization patterns are, however, very different in the case of the notched ribbon. In the 1st cycle (Fig. 67), the first Lüders band front is nucleated in the notch area already at the end of the elastic range in strain state 2, but the transformation remains limited to the notch area until ~2.2 % strain (strain state 6 - 7). Transformation within the notch area can be detected as a change in the slope of the stress-strain curve. Upon further tensile loading, the sample deforms via propagation of Lüders band fronts at constant stress up to the end of the transformation plateau. At the peak strain (strain state 11), three untransformed regions around the notch remain untransformed. The reverse process takes place upon unloading with the last transforming sample volume in the notch region. In

the 50th (Fig.68) and 100th (Fig.69) cycles, the evolution of strain localization pattern upon cycling remains similar, although it is gradually homogenized.

The single notched dog-bone sample fractured in the 107th cycle in the notched area, where unrecoverable plastic strain accumulated, and a terminal crack nucleated during the tensile cycling.

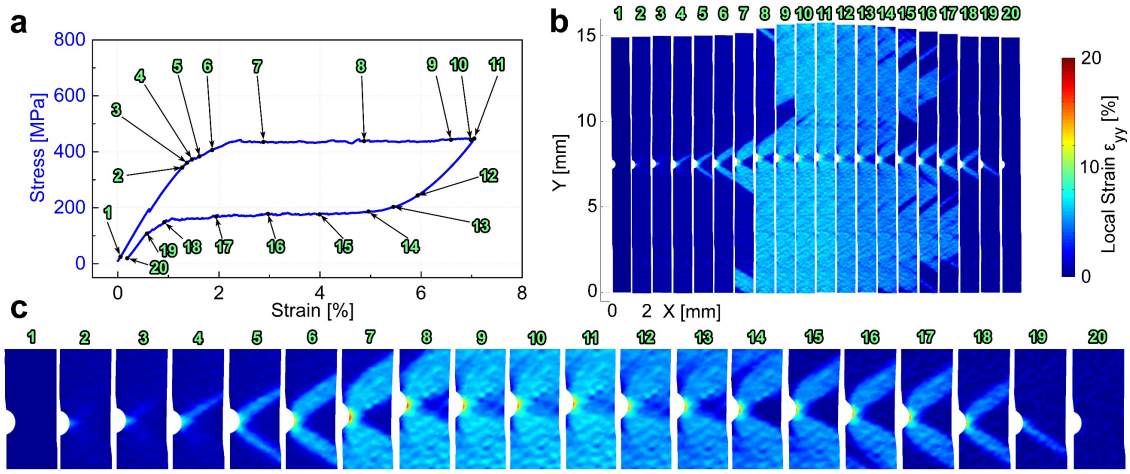

Figure 67: The macroscopic stress-strain curves during 1st SE loading-unloading in tension at 20 °C in a), with selected points on the macroscopic stress-strain curve corresponding to the local strain full-field DIC maps in b), and detailed local strain in surrounding the notch in c).

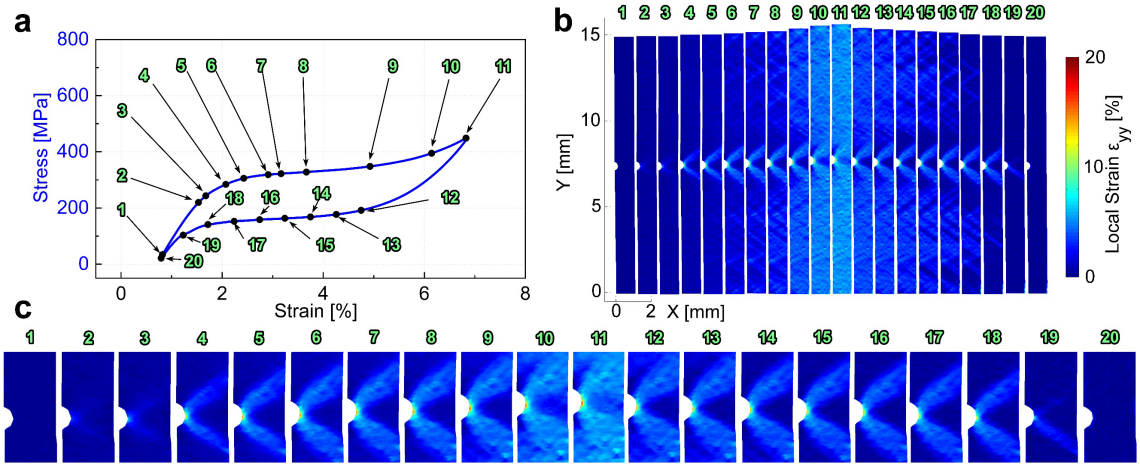

Figure 68: The macroscopic stress-strain curves during 50th SE loading-unloading in tension at 20 °C in a), with selected points on the macroscopic stress-strain curve corresponding to the local strain full-field DIC maps in b), and detailed local strain in surrounding the notch in c).

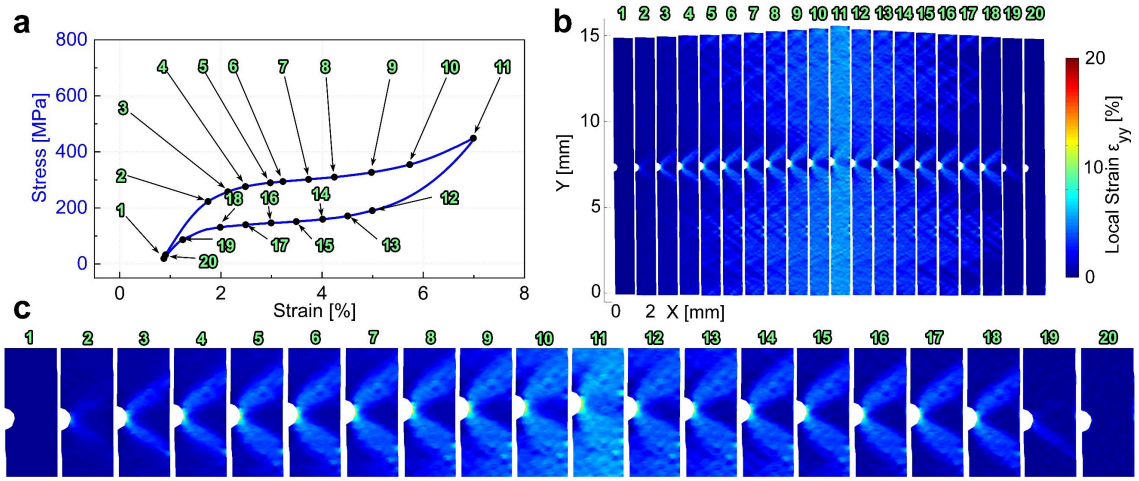

Figure 69: The macroscopic stress-strain curves during 100th SE loading-unloading in tension at 20 °C in a), with selected points on the macroscopic stress-strain curve corresponding to the local strain full-field DIC maps in b), and detailed local strain in surrounding the notch in c).

6.6.4 Uniaxial cycling of superelastic NiTi flat dog-bone with a circular hole

A circular hole was cut in the dog-bone sample (Fig. 70b). Superelastic stress-strain curve of the flat dog-bone sample with a circular hole is shown in Fig. 70a.

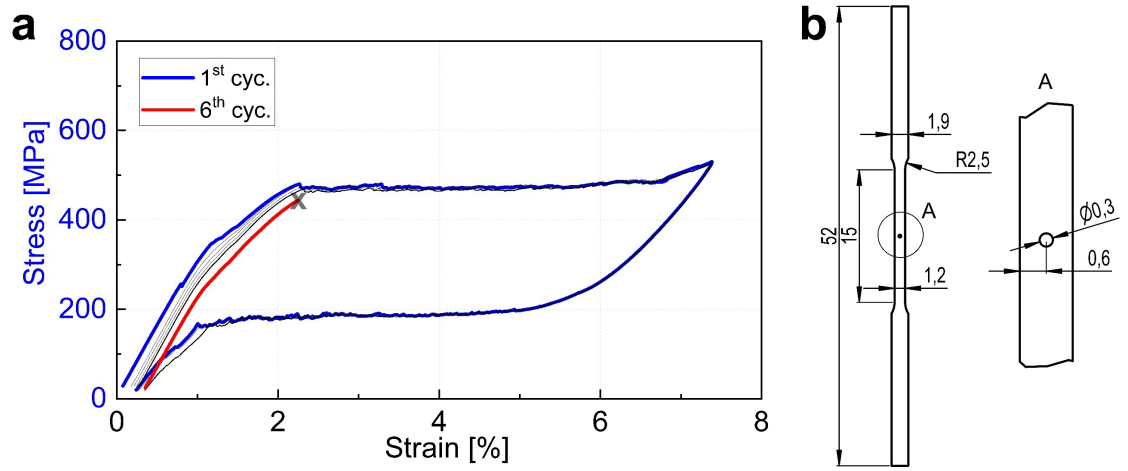

Figure 70: The macroscopic stress-strain curves during uniaxial cyclic loading-unloading in tension at 20 °C till failure in a). In b) detailed drawing of laser cut shape of the sample from 100 µm thick SE NiTi sheet with a circular hole. The fracture occurred during loading in the 6th cycle and is marked by X.

In the 1st cycle (Fig. 71), the sample was loaded elastically only between the strain states 1 and 2. First Lüders bands were nucleated in the hole area in strain state 3 and deformation localized within the hole area continued up to the strain state 6 when the first Lüders band nucleated at sample grip and propagated at constant stress till the end of the plateau in strain state 11. The untransformed volume in the circular hole area is clearly visible in strain state 12. The reverse process takes place upon unloading with the last transforming sample volume in the hole area.

In the 5th cycle (Fig. 72), a relatively small change in the strain localization pattern was observed. The largest difference in comparison to the 1st cycle is the increase of

strain near the hole accommodating residual strain after complete unloading (19) as shown in detail in Fig. 72c. Tensile deformation localized within the circular hole area between strain states 3 and 6 is more pronounced than in the 1st cycle/

In the 6th cycle (Fig. 73), the stress-strain response deviates from the linearity already at ~ 160 MPa (strain state 2). Tensile deformation localized within the circular hole area between strain states 3 and 6 is even more pronounced mainly within the part with pre-existing residual strain, the strain increased from 25 % to above 50 % (4-6). This large increase in local strain was followed by rapid fatal failure.

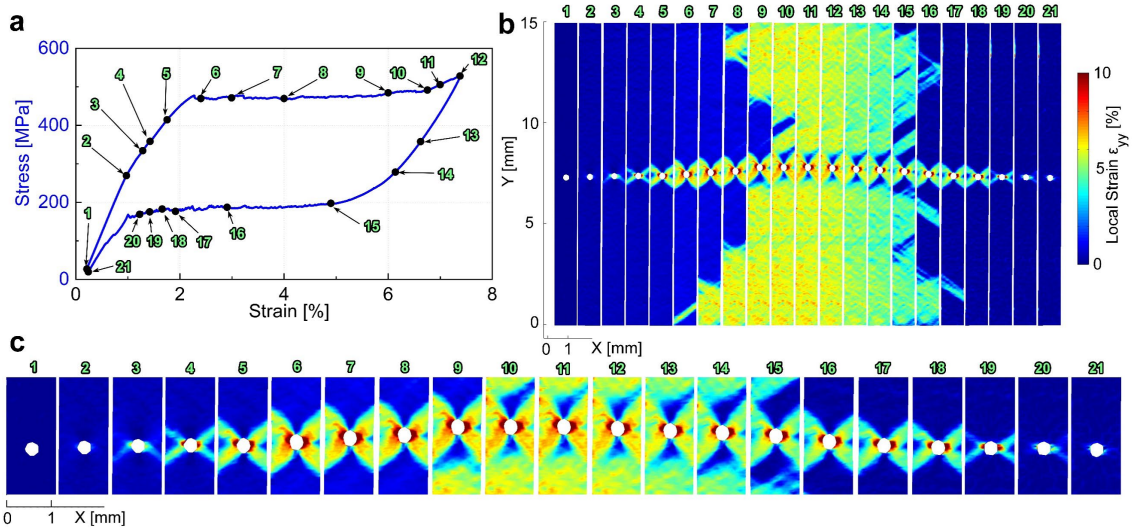

Figure 71: The macroscopic stress-strain curves during 1st SE loading-unloading in tension at 20 °C in a), with selected points on the macroscopic stress-strain curve corresponding to the local strain full-field DIC maps in b), and detailed local strain in surrounding of the hole in c).

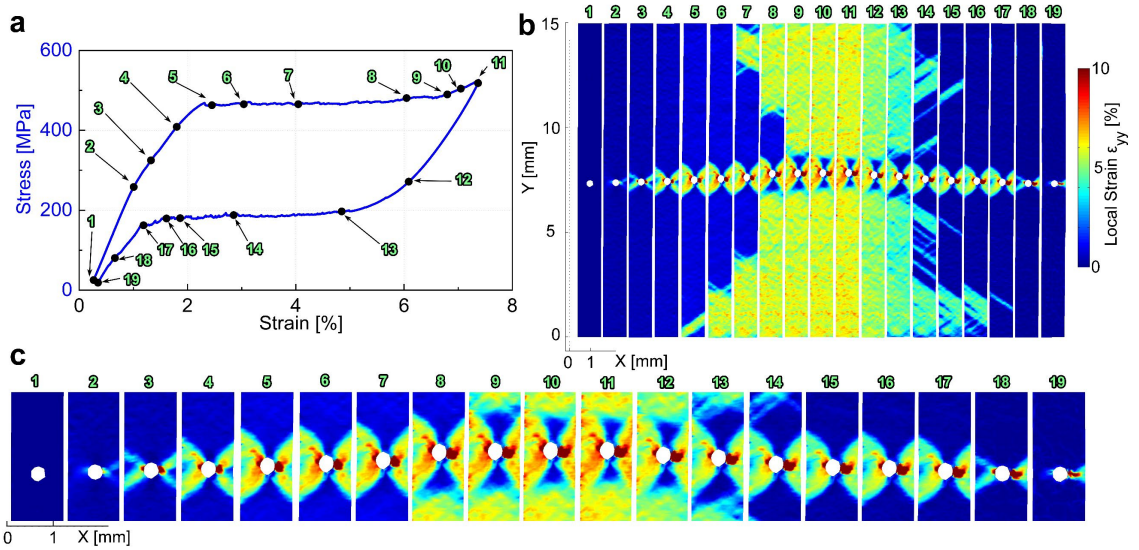

Figure 72: The macroscopic stress-strain curves during 5th SE loading-unloading in tension at 20 °C in a), with selected points on the macroscopic stress-strain curve corresponding to the local strain full-field DIC maps in b), and detailed local strain in surrounding of the hole in c).

The flat dog-bone sample with a circular hole fractured in the 6th cycle in the hole area, where unrecoverable plastic strain accumulated, and the terminal crack nucleated during the tensile cycling.

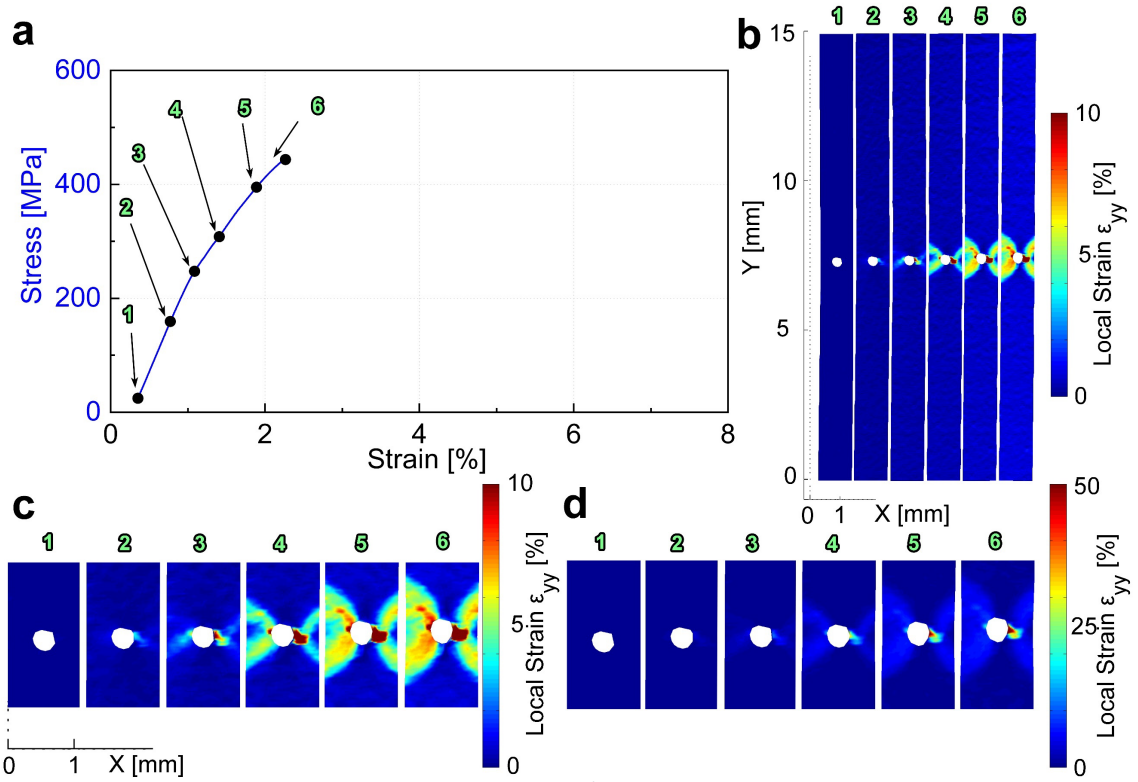

Figure 73: The macroscopic stress-strain curves during the 6th SE loading in tension at 20 °C in a), with selected points on the macroscopic stress-strain curve corresponding to the local strain full-field DIC maps in b), and detailed local strain in the surroundings of the hole in c).

6.6.5 Uniaxial cycling of superelastic NiTi flat dog-bone with an elliptical hole

An elliptical hole was cut in the dog-bone sample (Fig. 74b). Superelastic stress-strain curve of the flat dog-bone sample with an elliptical hole evolving during the 60 tensile cycles is shown in Fig. 74a.

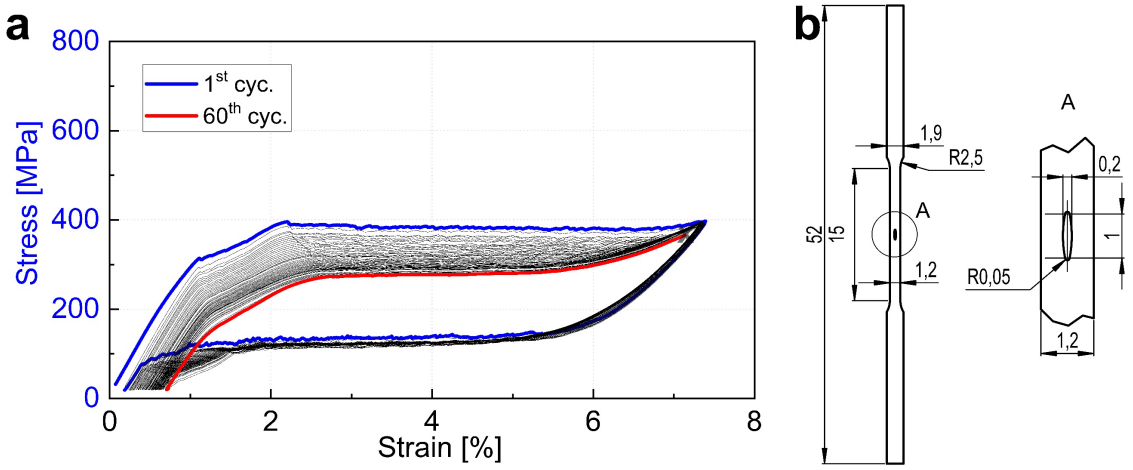

Figure 74: The macroscopic stress-strain curves during uniaxial cyclic loading-unloading in tension at 20 °C till failure in a). In b) detailed drawing of laser cut shape of the sample from 100 µm thick SE NiTi sheet with elliptical hole. The fracture occurred during loading in the 60th cycle and is marked by X.

In the 1st cycle (Fig. 75), the sample was loaded elastically only between the strain states 1 and 2. First Lüders bands were nucleated in the hole area in strain state 3 and deformation localized within the hole area continued up to strain state 7 when the first Lüders band nucleated below and above the elliptical hole. The corresponding band fronts propagated at constant stress till the end of the plateau in strain state 12. The untransformed volume in the area of the elliptical hole in strain state 12 is much smaller compared to the circular hole. The reverse process takes place upon unloading with the last transforming sample volume in the hole area.

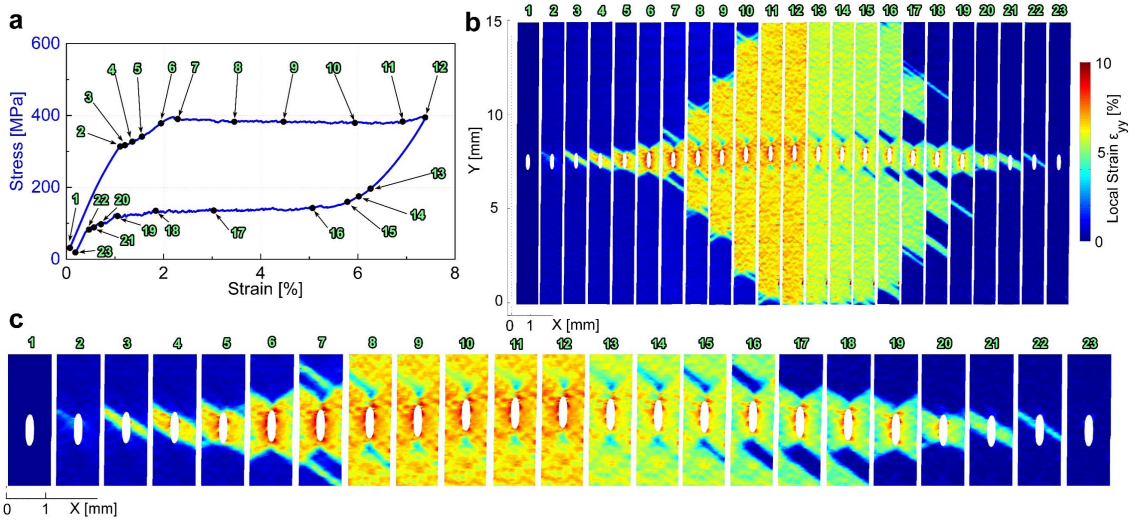

Figure 75: The macroscopic stress-strain curves during 1st SE loading in tension at 20 °C in a), with selected points on the macroscopic stress-strain curve corresponding to the local strain full-field DIC maps in b), and detailed local strain in the surroundings of the elliptical hole in c).

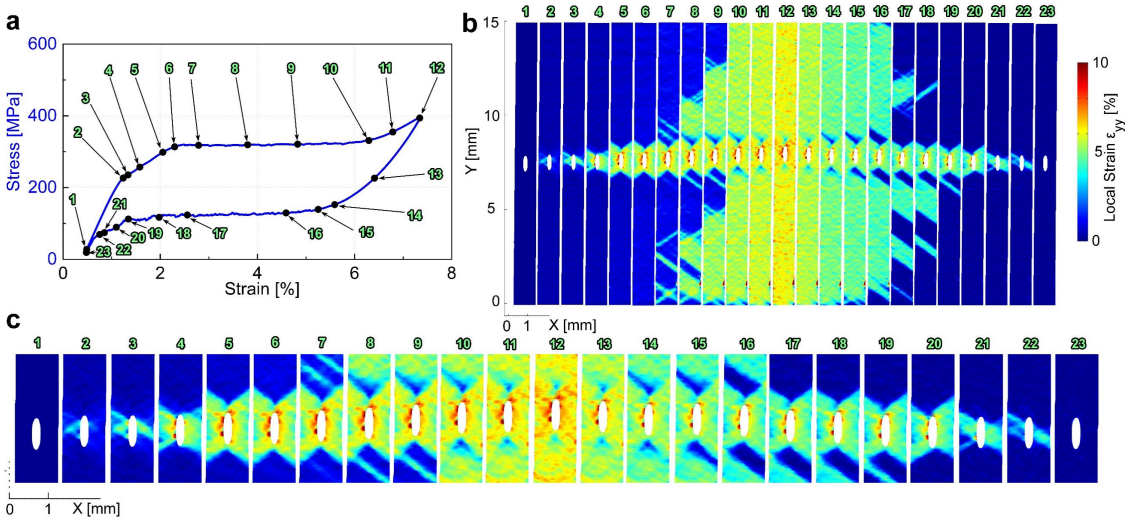

Figure 76: The macroscopic stress-strain curves during 20th SE loading in tension at 20 °C in a), with selected points on the macroscopic stress-strain curve corresponding to the local strain full-field DIC maps in b), and detailed local strain in the surroundings of the elliptical hole in c).

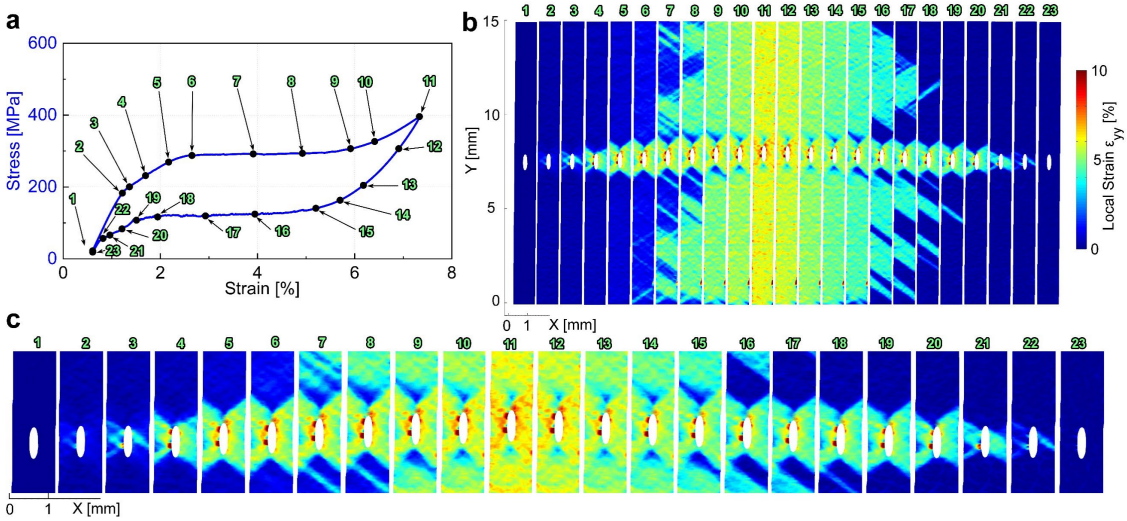

Figure 77: The macroscopic stress-strain curves during 50th SE loading in tension at 20 °C in a), with selected points on the macroscopic stress-strain curve corresponding to the local strain full-field DIC maps in b), and detailed local strain in the surroundings of the elliptical hole in c).

In the 20th cycle (Fig. 76), the stress-strain response deviates from the linearity already at ~ 220 MPa (strain state 2). However, when Lüders bands form (strain state 2-6) the deformation within the close vicinity of the elliptic hole reached high deformation (up to ~ 16 %), because of increased accumulation of defects during previous cycles several new Lüders bands are nucleated under and above the v-shaped overstrained area on both sides ends of the sample (7). The corresponding bands propagated at constant stress till the end of the plateau in strain state 11. The reverse process takes place upon unloading with the last transforming sample volume in the hole area. Besides that, more Lüders bands were formed in contrast to the 1st cycle.

In the 50^{h} cycle (Fig. 77), the stress-strain response deviates from the linearity already at ~ 180 MPa (strain state 2). Strain localization pattern evolves mainly in the area around the elliptical hole in strain state 3-7. The forward macroscopic stress plateau decreases to ~ 290 MPa. Newly nucleated bands around the elliptic hole (strain state 2-3) increased the local strain locally to ~ 20 % of the strain (strain state 3). The local strain in the Lüders bands decreased even more, indicating accumulation of defects in whole gauge length (7-18). The area surrounding the hole consists of a crack and remains constrained until the rest of the material closes the crack during reverse transformation (strain state 11-23).

The flat dog-bone sample with an elliptical hole fractured in the 60th cycle in the hole area, where unrecoverable plastic strain accumulated, and the terminal crack nucleated during the tensile cycling.

In Fig. 78a, the effect of the number of cycles until failure of superelastic NiTi dog-bones is presented for each variation of the macroscopic geometry. Each testing was performed under the same conditions (i.e., stress-strain limits and constant temperature). Fig. 78b shows profiles of local strain distribution across the cross-section in the mid-plane of all three flat dog-bone samples after first loading to the maximum stress (strain). Strain concentration is maximal for circular hole geometry for which the number of cycles until failure is minimal.

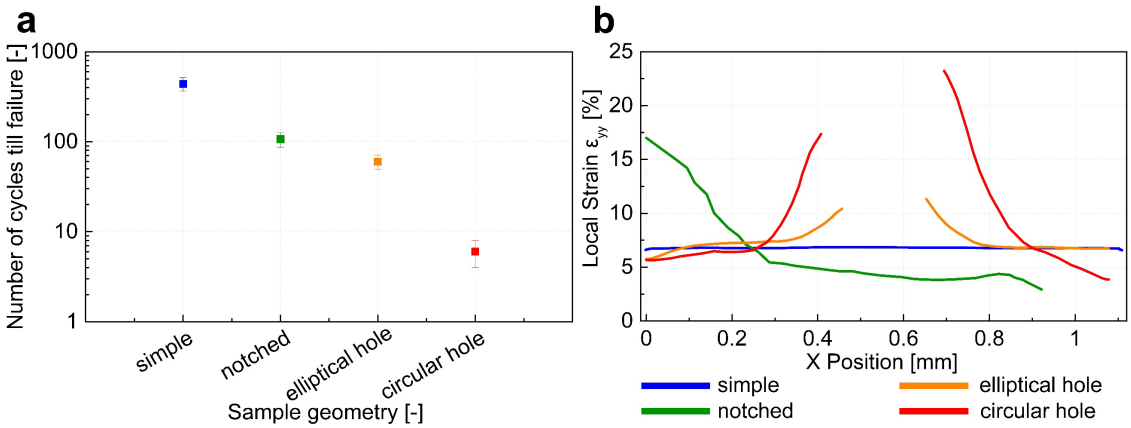

Figure 78: The dependence of number cycles until failure on the geometry of the tested flat superelastic NiTi dog bones with the same microstructure, and tested at the same temperature of 20 °C (plain-simple, one-side notched, with elliptic hole and with circular hole) in a) and local strain profiles after loading to martensite in the reduced cross-sections for each geometry in b).

6.6.6 Discussion

The effects of various stress concentrators on cyclic tensile deformation of flat superelastic NiTi ribbons were analyzed in this section using in-situ 2D DIC observations of the evolution of strain localization patterns upon tensile cycling. Stress concentrators in a form of nonmetallic inclusions exist in commercial bulk NiTi prepared from cast ingots and affect the fatigue performance of NiTi [9]. Another example is NiTi components of complex shapes (e.g., medical devices). Fatigue damage originates from those stress concentrators. Stress and strain redistribute around the stress riser and at the same time stress and strain redistribute within the moving Lüders band fronts [55,119,120]. It is thus of interest to investigate the redistribution of strains around stress risers depending on their geometry in NiTi components subjected to cyclic tensile strains, as reported in this chapter.

Results of the performed experiments on notched superelastic NiTi flat samples under cyclic tensile loadings have shown that:

1. Local strains in the notch tip area redistribute in a complex way in time and space upon tensile loading before Lüders band fronts start to propagate in the transformation plateau range of the stress-strain curve,
2. The macroscopic stress-strain response is affected by the presence and shape of a stress concentrator, particularly before the onset of martensitic transformation since the stress concentrator gives rise to nucleation of Lüders bands.
3. Due to the high local strains at the notch tip (~ 20 %), the material deforms there plastically.
4. there are strong correlations between the fatigue life and the local strain maxima at the notch tip. Larger local stress concentration at the notch tip leads to a faster accumulation of unrecoverable local strain at the notch tip and ultimately shorter fatigue life.

To analyze the time and spatial evolution of local strain in the notch area, the SMA model capturing strain localization phenomena and coupled martensitic transformation with plastic deformation would have to be numerically implemented and the problem of tensile deformation of the notched sample would have to be simulated by FE method. Such modeling research is currently underway by P. Sedlak and M. Frost from the

Institute of Thermomechanics of the Czech Academy of Sciences but is not yet ready at the time of completion of this thesis.

6.7 Fatigue of NiTi in thermomechanical actuator cycling

In this final chapter, I will present and discuss the results of experiments focusing on the fatigue of NiTi SMAs in thermomechanical actuator cycling. This research was not finished and shall be further continued. Before presenting the results, two circumstances shall be mentioned. The first issue is that evaluating the fatigue response of bulk NiTi subjected to thermomechanical cycling for millions of cycles requires specialized equipment which is not commercially available (fast heating by electric power is possible but slow cooling is a problem). The second issue is that thermomechanical fatigue tests are still not treated properly in the SMA field. Fatigue testing on NiTi SMAs shall be made in closed-loop thermomechanical load cycles starting from the austenite state – i.e., accumulation of residual martensite on unloading, which tends to occur in tensile cycling at a constant temperature, shall not be accepted. The sample subjected to isothermal tensile cycling shall be heated between cycles to recover the residual martensite, which is, however, technically difficult, and hence never done. Nevertheless, the cyclic thermomechanical loading test, in which the NiTi sample is thermally cycled under constant stress in a closed-loop regime, is the proper fatigue test for NiTi SMAs. In the case of SMA, the temperature is not a testing parameter, but the change in the test temperature is the driving force for the studied martensitic transformation.

Thermomechanical actuator cycling tests on NiTi SMA can be performed at various test conditions, under a constant load, under a variable load (e.g., against elastic spring), or under constant strain [121]. As an example, Fig. 79 (Fig. 80) shows strain-temperature response recorded upon thermal cycling of NiTi#1 450°C/30’ (Flexinol F90C) in closed-loop thermomechanical cycling tests at a constant tensile stress of 150, 400, and 600 MPa. The responses are different because the NiTi#1 450°C/30’ wire sample undergoes B2→R→B19’ transformation and Flexinol F90C only B2→B19’ transformation and simultaneously transformation temperature are different. Besides that, however, the observed strain-temperature responses are qualitatively similar. In-situ recorded electric resistance – temperature plot is included in Figs. 79,80.

Depending on the applied stress and temperature, various deformation/transformation processes take place in thermomechanical loading tests.

Therefore, it is necessary to determine a stress-temperature phase diagram summarizing the stress-temperature conditions at which these deformation/transformation processes take place (Fig. 81).

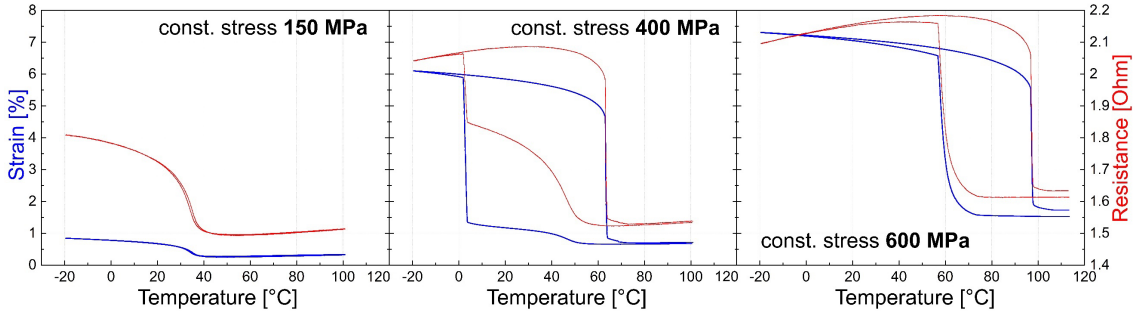

Figure 79: Strain-temperature and the evolution of resistance with the temperature of NiTi#1 450°C/30' loaded at 150, 400, and 600 MPa, represent reversible A→R, A→R→M, and A→M transformations, respectively.

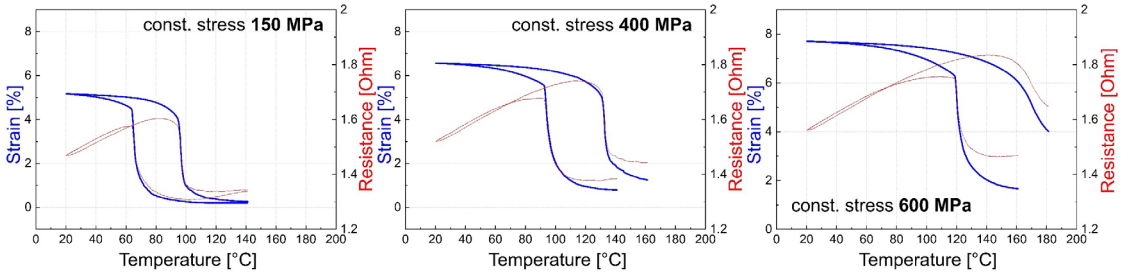

Figure 80: Strain-temperature (thermal cycles) of shape memory wire Flexinol F90C at 150, 400, and 600 MPa and their corresponding in-situ evolution of resistance.

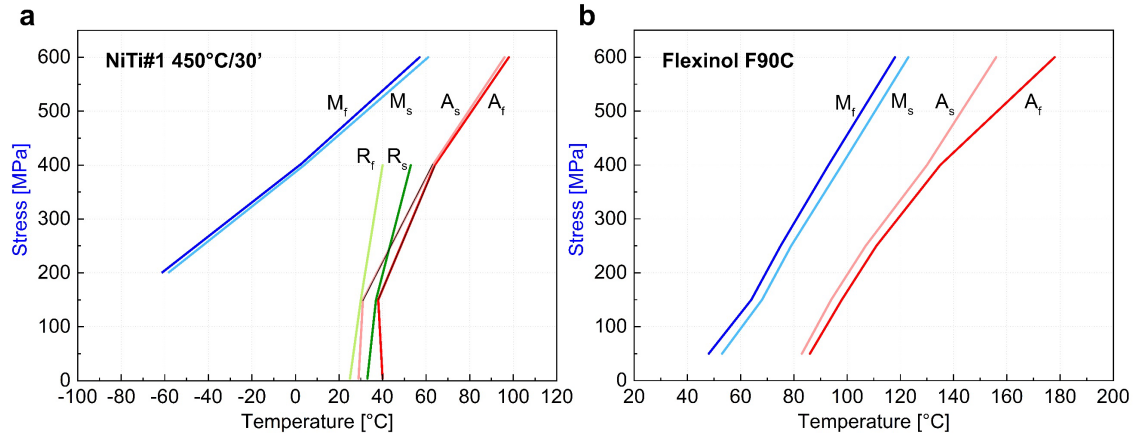

Figure 81: σ-T diagrams of transformation temperatures of NiTi#1 450°C/30'and Flexinol F90C in a) and b), respectively.

Due to the difference in microstructure and composition, relatively large strains are obtained upon thermal cycling of Flexinol F90C even at lower applied stresses (compare Fig. 79 and 80). On the other hand, reverse martensitic transformation in the thermal cycle at 600 MPa already proceeds at a relatively high temperature of 160-180 °C, which creates about 4 % of irrecoverable plastic strain, which is too much for NiTi actuator (plastic deformation must be considered as major deformation process). Fig. 82

shows strain-temperature records from thermal cycles on Flexinol F90C wire under constant stresses 50, 150, 250, 400, and 600 MPa.

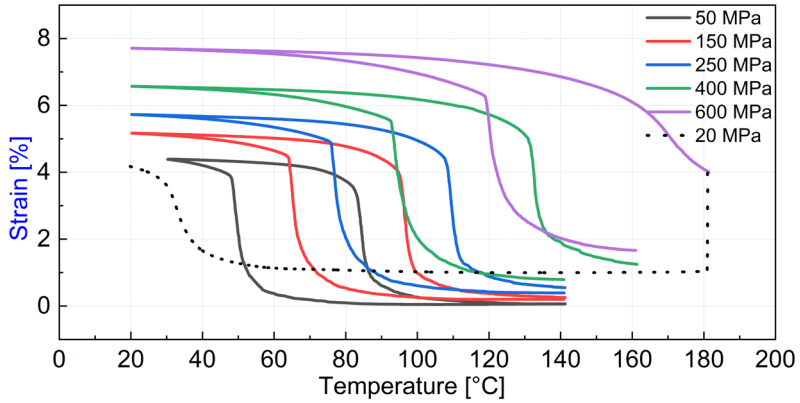

Figure 82: Strain-temperature cycles of NiTi Flexinol F90C at 50, 150, 250, 400, and 600 MPa. The dotted line corresponds to unloading after the cycle at 600 MPa to 20 MPa and cooling down to 20 °C corresponding to only 1 % of residual strain

6.7.1 Thermomechanical fatigue tests

While few thermomechanical loading cycles on NiTi SMAs are conveniently performed using an environmental furnace of thermomechanical loading testers, thermomechanical fatigue tests need to be performed by Joule heating the wire against active cooling. While in the former, the evolution of sample temperature is precisely defined (cooling/heating rates shall be low and thermal gradients shall be avoided), in the latter, it can be only estimated (cooling/heating rates shall be high and thermal gradients are unavoidable).

Fig. 83a shows the oscillation of tensile strain of Flexinol F90C wire thermally cycled by the electric current under constant applied stress 200 MPa. The sample did not break until 65000 cycles. Strain response upon cycling was relatively stable. Fig. 83b shows the evolution of accumulated unrecovered strain and actuation strain in the first 20000 thermal cycles). A sudden increase of stress (at 20k to 650 MPa and at 40k to 750 MPa) is due to the intentional overloading applied to investigate the stability of cyclic strain response to accidental overloading. Besides raising the unrecovered strain, however, the impact of overloading on material response is marginal. The experiment was stopped after 65000 cycles since the number of cycles till failure can be in hundreds of thousands or even millions and the experiment set up is not suitable for such tests.

Fig. 84 and 85 shows the oscillation of tensile strain of Flexinol F90C wire thermally cycled by the electric current under constant applied stress 500 MPa and 1000 MPa, respectively. The same joule heating pulse was used in tests under 200MPa, 500

MPa, and 1000 MPa. The actuation strain decreases with increasing applied stress partially because the wire is not heated enough at high stresses but also because of the plastic deformation which occurs upon heating under high applied stress.

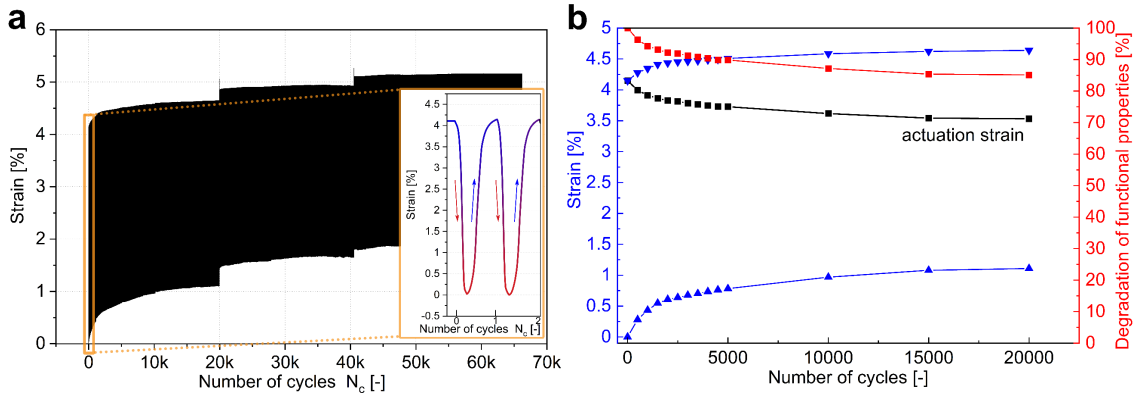

Figure 83: Actuator cycling of NiTi Flexinol F90C wire at 200 MPa via joule heating in a). The evolution in the first 20000th cycles of actuation strain, residual strain, and degradation of functional behavior at constant stress and pulse conditions in b). The cyclic stability is presented by the effect of sudden overloading to 650 and 750 MPa during 20k and 40k cycles, respectively in a).

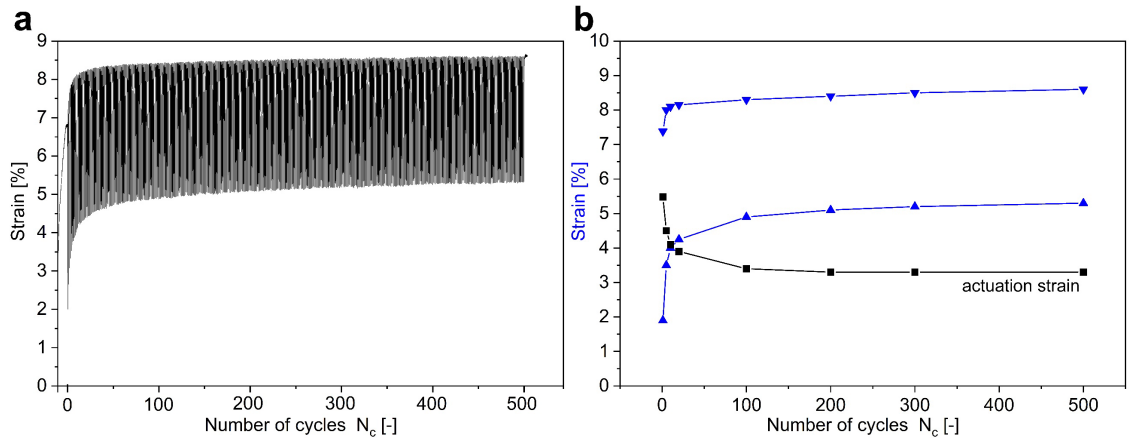

Figure 84: Actuator cycling of NiTi Flexinol F90C wire at 500 MPa via joule heating in a). The evolution in the first 500 cycles of actuation strain, residual strain at constant stress, and pulse conditions in b).

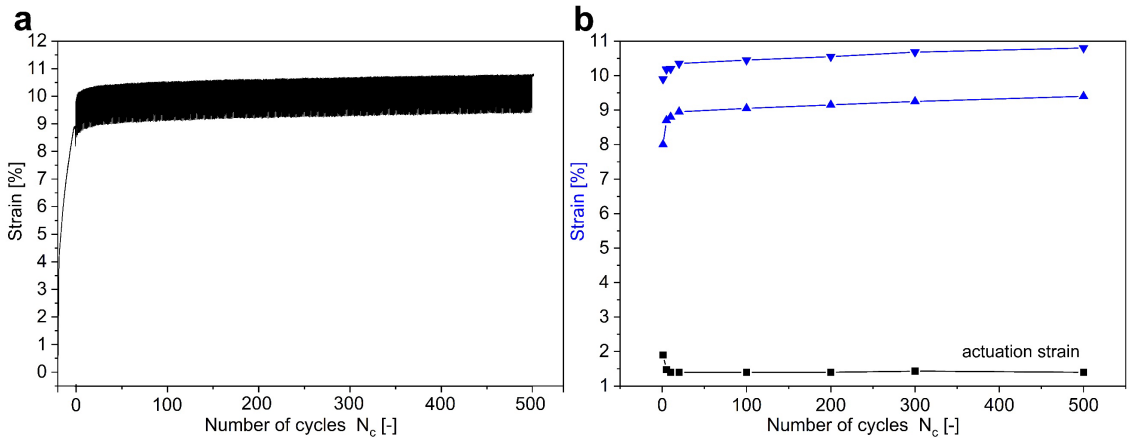

Figure 85: Actuator cycling of NiTi Flexinol F90C wire at 1000 MPa via joule heating in a). The evolution in the first 500 cycles of actuation strain, residual strain at constant stress, and pulse conditions in b).

6.7.2 Strain localization phenomena in thermomechanical loading tests

It was discussed in Chapters 5 and 6 how macroscopic strain localization in tension affects the monotonic and cyclic stress-strain behaviors of NiTi. There is a question whether such macroscopic strain localization occurs also if the martensitic transformation is induced thermomechanically in actuator tests. Besides the sample itself, the actuator test conditions, such as thermal gradients or heating rate, may also affect strain localization phenomena.

Results of a test dedicated to thermal cycling under very large applied stress 700 MPa are shown in Fig. 86. Three subsequent thermal cycles are performed on NiTi#1 wire (16 ms, d= 100 μm) as presented in Fig. 86a,b. Note that strain does not decrease on heating but reverse martensitic transformation occurs in these tests. This means that reverse martensitic transformation is accompanied by very large plastic deformation which compensates for the strain reversal upon heating. There was a question whether the macroscopic strain is localized during the heating under constant stress 700 MPa (stage 1).

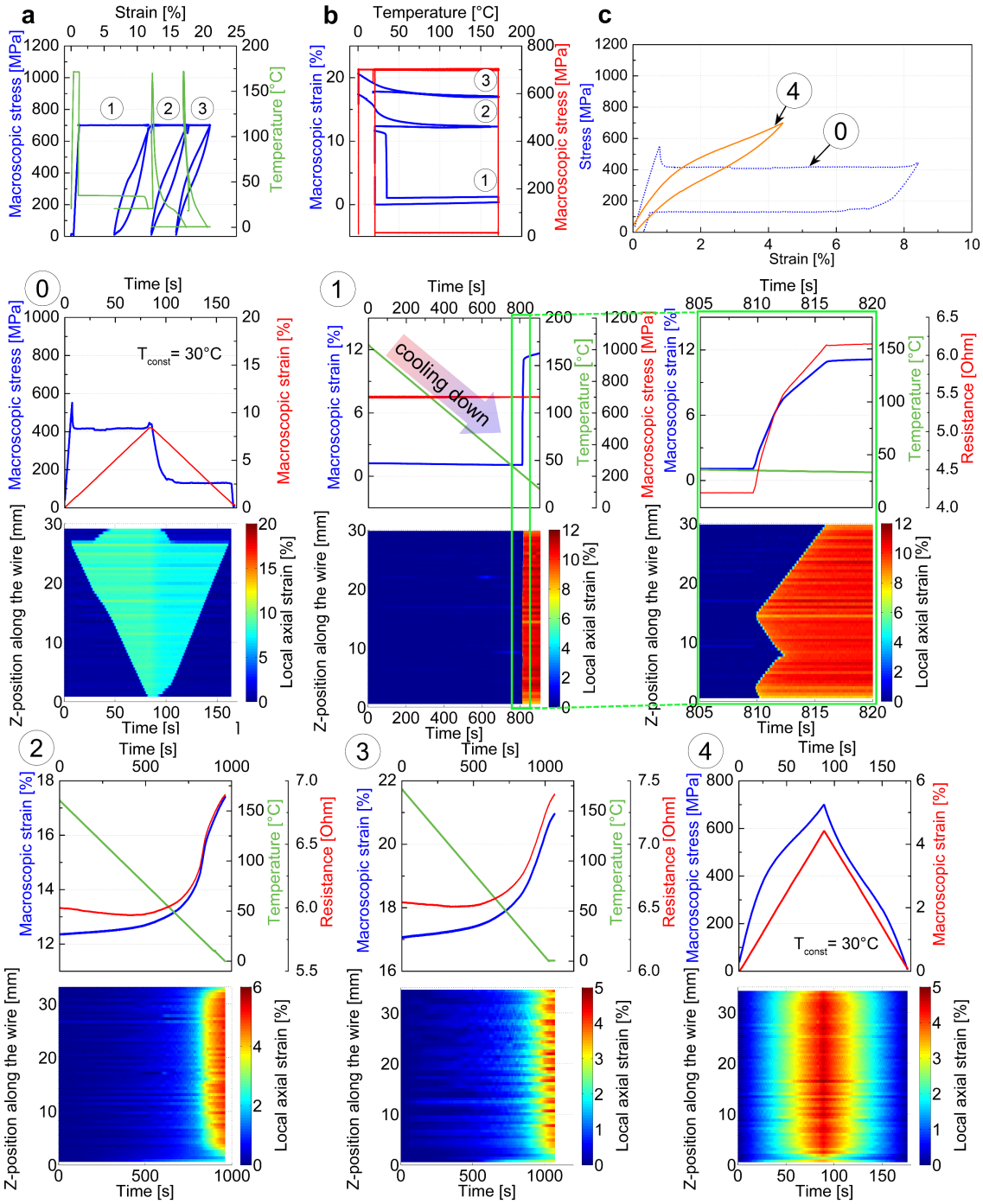

Figure 86: Schematic actuator cycling of NiTi#1 16 ms at a constant stress of 700 MPa during three subsequent cycles (1-3), tracking the change of functional behavior and local strain response. In a) stress-strain, b) strain-temperature, and in c) representing the difference between virgin (0) and the wire after thermal cycling at 700 MPa in (4) at constant strain rate 0.0005 s^{-1} and temperature 30 °C.

Results of the 1D-DIC observation show that strain is localized in the superelastic cycle at 30 °C (0 in Fig. 86). However, it is also localized upon the first heating under constant stress 700 MPa (1 in Fig. 86) but not in the 2nd and 3rd heating under constant stress due to the change of the austenitic microstructure of the wire by the plastic deformation during the first heating. Macroscopic strain is localized neither in the subsequently performed superelastic cycle at 30 °C (4 in Fig. 86) due to the same reason.

Fig. 87 shows the results of the 1D-DIC observation of strain localization patterns during thermal cycles on two NiTi#5 shape memory wires with two different microstructures (14 ms and 16 ms) subjected to a single cooling-heating cycle at a constant applied stress of 200 MPa.

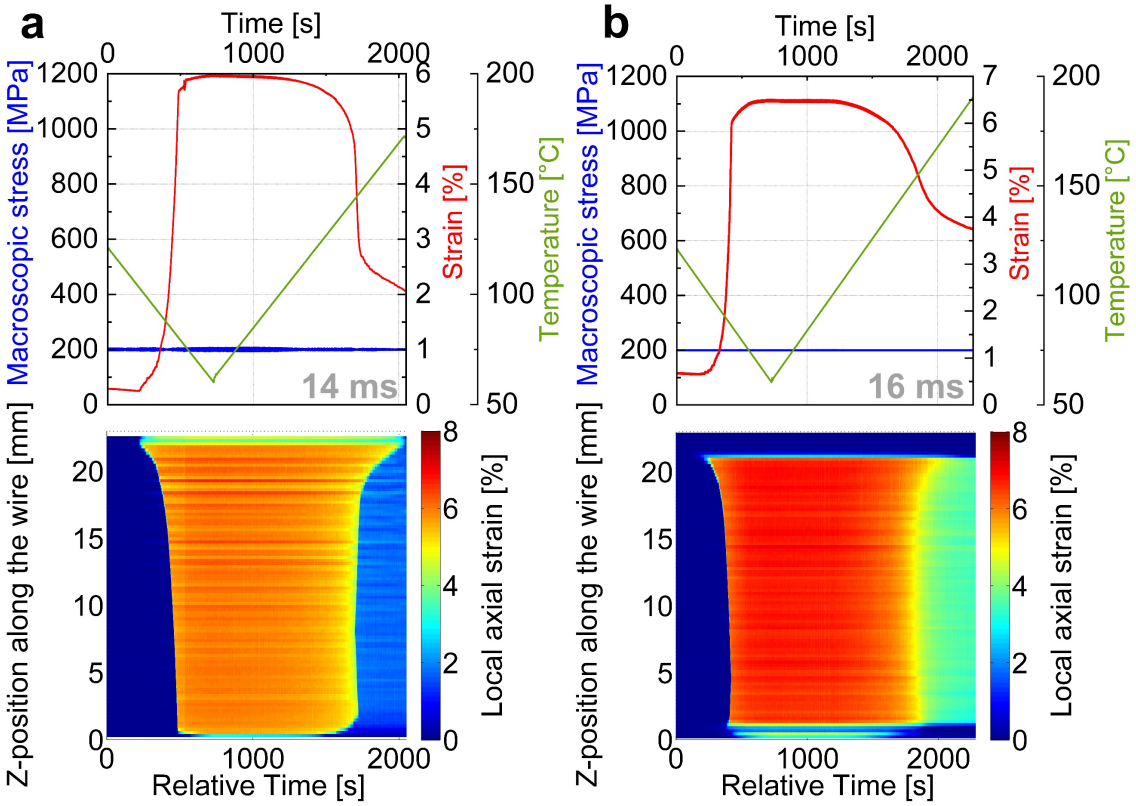

Figure 87: Local strain redistribution on the shape memory NiTi# 5 wires with 14 ms in a) and 16 ms in b) cycled thermally under 200 MPa.

Although both wires undergo reverse martensitic transformation at 150 °C and 200 MPa, the 16 ms wire with larger grain size generates 4 % unrecovered stress while 14 ms wire only ~ 1.5 % unrecovered strain. It was found that macroscopic strain is localized upon heating under 200 MPa stress in both wires, though the moving front is more spread in the case of the 16 ms wire. Strain localization thus cannot explain the difference in unrecovered strains.

6.7.3 Discussion

Thermomechanical fatigue testing of NiTi wires in tension requires the development of special equipment and testing strategies, which I am currently trying to develop. Therefore, this chapter contains only preliminary results obtained using currently available equipment for mechanical fatigue testing.

Preliminary experiments reported in this chapter has been shown that:

1. Plastic deformation accompanying reverse martensitic transformation under applied stress is critical for cyclic stability of strain temperature response of NiTi actuator wires.
2. A very large number of thermomechanical load cycles (>100000) can be achieved in the thermal cycling of commercial NiTi under low applied stress (<200 MPa).
3. It is proposed that, if a reverse martensitic transformation in an actuator test takes place above critical [stress, temperature] conditions (depending on wire microstructure and chemical composition), cyclic instability of thermomechanical response increases and the number of cycles until failure drastically decreases (this remains to be experimentally verified).
4. Macroscopic strain localization may/need not occur in thermomechanical loading cycles equally as in isothermal loading cycles.
5. Macroscopic strain localization was observed upon cooling the NiTi actuator wire under the constant stress of 700 MPa but not upon heating under 700 MPa stress. This is again due to the plastic deformation accompanying reverse martensitic transformation.
6. A very large number of thermomechanical load cycles (>100000) can be achieved in thermal cycling under low applied stress (<200 MPa).
7. Macroscopic strain localization may occur in thermomechanical loading cycles equally as in isothermal loading cycles.

7 Conclusions

NiTi shape memory alloy wires can theoretically recover strains as large as 5 % in tensile loading-unloading and, hence, sustain millions of closed-loops mechanical or thermomechanical loading cycles until fatigue failure. In practice, superelastic NiTi wires cycled in tension fail after ~ 5000 cycles, which represents a key obstacle to the realization of exciting engineering applications and further growth of NiTi technologies. The aim of my experimental work, part of which is summarized in this thesis, was to discover why this is the case and how the fatigue lifetime of commercial NiTi in cyclic tension can be potentially improved.

Following conclusions of the work, going beyond the state-of-the-art understanding of NiTinol fatigue, are pointed out:

Methodical

1. A digital image correlation method for in-situ analysis of localized deformation of ultrathin NiTi wires in cyclic tension was developed and systematically employed in mechanical and thermomechanical fatigue tests on NiTi. Systematic application of the method in cyclic (thermo)mechanical loading tests enabled us to obtain a deeper understanding of the phenomena controlling strain localization, accumulation of damage, and ultimately fatigue performance of NiTi shape memory alloys.

Localized tensile deformation of NiTi on multiple scales

2. Tensile deformation of superelastic NiTi wire taking place via stress-induced martensitic transformation followed by plastic deformation of stress-induced martensite gives rise to complex strain localization patterns (long plateaus, multiple plateaus, necking). In particular, necking within Lüders bands limits the ductility of NiTi deformed in tensile tests at elevated temperatures of 200-400 °C.
3. Macroscopic strain localization into Lüders band fronts propagating at constant tensile stress in NiTi is controlled by the yield stress and strain hardening rate through the Considère's criterion for stability of macroscopic tensile deformation.

4. Plastic deformation B19' martensite in NiTi can be either localized or homogeneous in dependence on the test temperature and virgin austenitic microstructure of the wire (grain size)
5. Plastic deformation of B19' martensite in NiTi proceeds vi a newly discovered kwinking deformation mechanism involving a combination of deformation twinning with dislocation slip-based kinking [122]. The mechanism enabling NiTi to deform plastically at stresses around 1GPa up to very large plastic strains at fracture (20-60 %) becomes activated during cyclic deformation locally in near nonmetallic inclusions, near the stress concentrators, etc.
6. Localized plastic deformation of martensite phase in NiTi proceeds either as necking leading to fracture at 13-15 % strain or as propagation of macroscopic Lüders band fronts in which unusually large plastic strain is localized (up to 40 % strain in dependence on wire microstructure and test temperature).
7. Localized deformation with 40 % strain within the propagating Lüders band front was observed in tensile tests on NiTi wires having specific microstructures (grain size ~ 230 nm) in a narrow temperature interval (10-60 °C).
8. On the grain scale, the macroscopic Lüders band front propagating through the flat dog-bone superelastic NiTi sample (grain size ~ 22 μm) is formed by mesoscale deformation bands in grains in which stress-induced B2→B19' transformation is probably immediately followed by plastic deformation of the stress-induced B19' martensite by kwinking. Strain localized within the mesoscale deformation bands exceeds the crystallographic limit of the B2→B19' transformation and is unrecoverable on unloading and heating

Fatigue of NiTi in tension

9. NiTi wire subjected to thermomechanical cyclic loads, in which martensitic transformation takes place under stress, deforms by coupled elastic deformation, deformation processes derived from martensitic transformation, and plastic deformation in martensite and austenite.
10. In sharp contrast to fatigue of conventional metals and alloys, high stresses, large mean strains, and/or large strain (stress) amplitudes imposed in tensile cycling of superelastic NiTi do not necessarily result in worse fatigue performance. In particular, NiTi wire loaded cyclically around ~ 800 MPa in the martensite phase

at 8 % mean strain shows 10 times longer fatigue life than NiTi wire cycled around ~ 200 MPa in the R-phase state at 0.5 % mean strain.

11. Fatigue lifetime of superelastically cycled NiTi wires: i) decreases with increasing test temperature (plateau stress) regardless of the applied strain or stress limit, ii) does not correlate with the instability of stress-strain response and accumulated residual strain (functional fatigue), iii) increases with increasing strain rate due to the decrease of transforming volume in a single closed-loop cycle.

Strain localization phenomena in fatigue testing of NiTi

12. Strain localization phenomena affect drastically the performance of superelastic NiTi wires in partial superelastic cyclic tests since the material deforms (transforms) only in locations of the wire, where Lüders band fronts move upon tensile cycling. Depending on the mean strain and strain (stress) amplitude, the externally imposed cyclic strain either delocalizes or remains localized during the partial superelastic cycling. The latter significantly decreases fatigue lifetime since the local strain amplitude can be as large as ~ 6 % even in tensile tests with a prescribed strain amplitude of 1 %.
13. If stress-induced martensitic transformation upon partial tensile cycling proceeds in a stress plateau, the magnitude of strain (stress) amplitude has only a minor effect on the fatigue life due to macroscopic strain localization.
14. Plastic deformation accompanying stress-induced martensitic transformation in locations, where the Lüders band front move, generates lattice defects and internal stress in the wire microstructure which thus evolves upon tensile cycling, while in locations, where Lüders band fronts do not move, remain unaffected. Since transformation stress decreases upon tensile cycling, the imposed strain amplitude tends to remain localized during superelastic fatigue tests.
15. Periodic overloading of superelastically cycled NiTi wire may result in a significant increase in fatigue life. The observation was explained by the beneficial effect of periodic plastic deformation taking place selectively at crack tips in cycled material. There are multiple characteristics of overloading whose impact on fatigue life, which must be investigated including maximum stress(strain), number of overloading cycles, mean strain and amplitude of

overloading cycles, and frequency of overloading and adjusted to reach the effect for NiTi wire with particular virgin annealing microstructure.

16. A very long fatigue lifetime of commercial NiTi wire was achieved in superelastic tensile cycling with adaptive limits at 10 °C (N_c > 200000 cycles). This is considered a real breakthrough. The observation was explained simply as a consequence of a combination of minimization of the upper plateau stress and optimization of virgin austenitic microstructure for resistance to accumulation of fatigue damage.
17. Strain localization phenomena and the character of stress risers (notch, circular hole, elliptical hole) significantly affect the number of cycles until failure in superelastic fatigue tests on NiTi.

7.1 Aims of the thesis and how they were fulfilled

1. A deeper understanding of fatigue of NiTi shape memory alloys, characterization of strain localization, and accumulation of irreversible changes in the microstructure.

   The aim was fulfilled - see conclusions 1, 12-17.

2. Investigation of martensitic transformation localization effects during cyclic deformation of NiTi alloys and limits of reversibility of martensitic transformation.

   Strain localization phenomena observed in monotonic and cyclic tensile tests on NiTi alloys of various shapes and compositions were investigated (conclusions 2-8 and 12-18).

3. Analysis of the temperature dependence of transformation/deformation modes in NiTi alloys having different microstructures.

   The effects of temperature and stress at which martensitic transformation proceeds in (thermo)mechanical loading tests were investigated (conclusions 9-11 & Chapter 6.7).

4. Examination of the effect of sample preparation, especially heat treatment and shape modification, on fatigue of NiTi alloys.

   The effects of various heat-treatment in an environmental furnace and Joule heating on the fatigue of NiTi were analyzed. The effects of sample shape (NiTi wires, flat ribbon with single notch, circular hole, and elliptical hole) on fatigue of NiTi were analyzed.

7.2 Future work

There are multiple areas in which I would be interested to continue my research on NiTi-based shape memory alloys. Almost all would be motivated by multiscale problems of localized deformation, leading to the fatigue of NiTi. However, if this shall be carried out in FZU, it would require project funding.

The following topics carry the potential for improvement in understanding NiTinol fatigue:

1. Gathering of further experimental material for the development of SMA models capturing thermomechanical behaviors due to combined martensitic transformation and plastic deformation. This issue is also critical for cyclic deformation and fatigue. There is a GACR project supporting this research until 2024.
2. In-situ Nanomechanical and micromechanical experiments on NiTi in SEM using dedicated equipment (DEBEN, FEMTOTools, and/or ASTAR in TEM).
3. Effect of alloying on the fatigue properties of NiTiX.
4. The effects of the composition on the deformation of NiTi at high temperatures.
5. Thermomechanical actuator fatigue of NiTi, which would also require the development of dedicated equipment.

List of publications of the author related to the topic of the dissertation

[1] KADEŘÁVEK, L., ŠITTNER, P., MOLNÁROVÁ, O., KLIMŠA, L., & L. HELLER. Localized Plastic Deformation of Superelastic NiTi Wires in Tension. *Shape Memory and Superelasticity*, (2023), 1-19. [IF= 2.5; Number of citations= 0] *

[2] SITTNER, P., IAPAROVA, E., KADERAVEK, L., CHEN, Y., & O. TYC. Tensile deformation of NiTi shape memory alloy thermally loaded under applied stress. *Materials & Design*, (2023), 111638. [IF= 9.4; Number of citations= 1]

[3] BIAN, X., HELLER, L., TYC, O., KADEŘÁVEK, L., & P. ŠITTNER. In-situ synchrotron x-ray diffraction texture analysis of tensile deformation of nanocrystalline superelastic NiTi wire at various temperatures. *Materials Science and Engineering: A*, *853*, (2022), 143725. [IF= 6; Number of citations= 5]

[4] BIAN, X., HELLER, L., KADEŘÁVEK, L., & P. ŠITTNER. In-situ synchrotron X-ray diffraction texture analysis of tensile deformation of nanocrystalline NiTi wire in martensite state. *Applied Materials Today*, *26*, (2022), 101378. [IF= 8.6; Number of citations= 13]

[5] BENEŠOVÁ, B., FROST, M., KADEŘÁVEK, L., ROUBÍČEK, T., & P. SEDLÁK. An experimentally-fitted thermodynamical constitutive model for polycrystalline shape memory alloys. *Discrete and Continuous Dynamical Systems-S*, *14*(11), (2021), 3925-3952. [IF= 2.4 ; Number of citations= 2] *

[6] VOKOUN, D., PILCH, J., KADEŘÁVEK, L., & P. ŠITTNER. Strength of superelastic NiTi velcro-like fasteners. *Metals*, *11*(6), (2021), 909. [IF= 2.7; Number of citations= 1] *

[7] FROST, M., ŠEVČÍK, M., KADEŘÁVEK, L., ŠITTNER, P., & P. SEDLÁK. Reconstruction of phase distributions in NiTi helical spring: comparison of diffraction/scattering computed tomography and computational modeling. *Smart Materials and Structures*, *29*(7), (2020), 075036. [IF= 4.1 ; Number of citations= 4] *

[8] ŠITTNER, P., MOLNÁROVÁ, O., KADEŘÁVEK, L., TYC, O., & L. HELLER. Deformation twinning in martensite affecting functional behavior of NiTi shape memory alloys. *Materialia*, *9*, (2020), 100506. [IF= 3.4; Number of citations= 34] *

[9] ŠITTNER, P., HELLER, L., SEDLÁK, P., CHEN, Y., TYC, O., MOLNÁROVÁ, O., ... & H. SEINER. B2⇒ B19′⇒ B2 T Martensitic Transformation as a Mechanism of Plastic Deformation of NiTi. *Shape Memory and Superelasticity*, *5*, (2019), 383-396. [IF= 2.5; Number of citations= 10] *

[10] VOKOUN, D., KADEŘÁVEK, L., BALOGOVÁ, J., FEKETE, L., LANDA, M., DRAHOKOUPIL, J., ... & L. HELLER. Effect of FIB milling on NiTi films and NiTi/Si micro-bridge sensor. *Smart Materials and Structures*, *29*(1), (2019), 015001. [IF= 4.1; Number of citations= 2] *

[11] CHEN, Y., MOLNÁROVÁ, O., TYC, O., KADEŘÁVEK, L., HELLER, L., & P. ŠITTNER. Recoverability of large strains and deformation twinning in martensite during tensile deformation of NiTi shape memory alloy polycrystals. *Acta Materialia*, *180*, (2019), 243-259. [IF= 8.2 ; Number of citations= 57] *

[12] CHEN, Y., TYC, O., KADEŘÁVEK, L., MOLNAROVA, O., HELLER, L., & P. ŠITTNER. Temperature and microstructure dependence of localized tensile deformation of superelastic NiTi wires. *Materials & Design*, *174*, (2019), 107797. [IF= 9.4; Number of citations= 41] *

[13] HELLER, L., SEINER, H., ŠITTNER, P., SEDLÁK, P., TYC, O., & L. KADEŘÁVEK. On the plastic deformation accompanying cyclic martensitic transformation in thermomechanically loaded NiTi. *International Journal of Plasticity*, *111*, (2018), 53-71. [IF= 8.5; Number of citations= 63] *

[14] ŠITTNER, P., SEDLÁK, P., SEINER, H., SEDMÁK, P., PILCH, J., DELVILLE, R., ... & L. KADEŘÁVEK. On the coupling between martensitic transformation and plasticity in NiTi: Experiments and continuum based modelling. *Progress in Materials Science*, *98*, (2018), 249-298. [IF= 48.1; Number of citations= 94] *

[15] FROST, M., SEDLÁK, P., HELLER, L., KADEŘÁVEK, L., & P. ŠITTNER. Experimental and computational study on phase transformations in superelastic NiTi snake-like spring. *Smart Materials and Structures*, *27*(9), (2018), 095005. [IF= 4.1; Number of citations= 12] *

[16] VOKOUN, D., RACEK, J., KADEŘÁVEK, L., KEI, C. C., YU, Y. S., KLIMŠA, L., & P. ŠITTNER. Atomic layer-deposited TiO 2 coatings on NiTi surface. *Journal of Materials Engineering and Performance*, *27*, (2018), 572-579. [IF= 2; Number of citations= 7] *

[17] HELLER, L., ŠITTNER, P., SEDLÁK, P., SEINER, H., TYC, O., KADEŘÁVEK, L., ... & M. VRONKA. Beyond the strain recoverability of martensitic transformation in NiTi. *International Journal of Plasticity*, *116*, (2019), 232-264. [IF= 8.5; Number of citations= 78] *

[18] FROST, M., SEDLÁK, P., KADEŘÁVEK, L., HELLER, L., & P. ŠITTNER. Modeling of mechanical response of NiTi shape memory alloy subjected to combined thermal and non-proportional mechanical loading: a case study on helical spring actuator. *Journal of Intelligent Material Systems and Structures*, *27*(14), (2016),1927-1938. [IF= 2.7 ; Number of citations= 24]

[19] VOKOUN, D., SYSEL, P., HELLER, L., KADEŘÁVEK, L., SVATUŠKA, M., GORYCZKA, T., ... & P. ŠITTNER. NiTi-polyimide composites prepared using thermal imidization process. *Journal of Materials Engineering and Performance*, *25*, (2016), 1993-1999. [IF= 2; Number of citations= 5] *

[20] KEI, C. C., YU, Y. H., RACEK, J., VOKOUN, D., & L. KADEŘÁVEK. Corrosion and mechanical properties of atomic layer deposited TiO2 coatings on NiTi implants. In *2016 IEEE International Conference on Industrial Technology (ICIT)*, (2016), 1328-1332. IEEE. [IF= 1; Number of citations= 2]

[21] RACEK, J., ŠITTNER, P., HELLER, L., PILCH, J., SEDLÁK, P., & L. KADEŘÁVEK. Electrochemistry of NiTi wires/springs subjected to static/cyclic loadings. *Materials Today: Proceedings*, *2*, (2015), S965-S969. [IF= 1.4 ; Number of citations= 7]

List of References

[1] HARTL, D. J., and DIMITRIS C. LAGOUDAS. Aerospace applications of shape memory alloys. *Proceedings of the Institution of Mechanical Engineers, Part G: Journal of Aerospace Engineering* 221.4 (2007): 535-552.

[2] JANI, J.M., et al. A review of shape memory alloy research, applications and opportunities. Materials & Design 56 (2014): 1078-1113.

[3] HUMBEECK, J.V. Non-medical applications of shape memory alloys. Materials Science and Engineering: A 273 (1999): 134-148.

[4] DUERIG, T. W., A. PELTON, and D. STÖCKEL. An overview of nitinol medical applications. Materials Science and Engineering: A 273 (1999): 149-160.

[5] SONG, CH., History and current situation of shape memory alloys devices for minimally invasive surgery. The Open Medical Devices Journal 2.1 (2010).

[6] ELAHINIA, M., et al. Fabrication of NiTi through additive manufacturing: A review. Progress in Materials Science 83 (2016): 630-663.

[7] OTSUKA, K., and X. Ren. Physical metallurgy of Ti-Ni-based shape memory alloys, *Prog. Mater. Sci*., (2005), 50, 511-678.

[8] OTSUKA, K., and C.M. WAYMAN. Shape Memory Materials. *Cambridge, University Press*, (1998).

[9] FRENZEL, J. On the importance of structural and functional fatigue in shape memory technology. Shape Memory and Superelasticity, (2020), 6.2: 213-222.

[10] JAMES, R. D., and K. F. HANE. "Martensitic transformations and shape-memory materials." *Acta materialia* 48.1 (2000): 197-222.

[11] KHALIL-ALLAFI, J., A. DLOUHY, and G. EGGELER. Ni4Ti3-precipitation during aging of NiTi shape memory alloys and its influence on martensitic phase transformations. *Acta materialia* 50.17 (2002): 4255-4274.

[12] WAITZ, T., V. KAZYKHANOV, and H. P. KARNTHALER. Martensitic phase transformations in nanocrystalline NiTi studied by TEM. *Acta Materialia* 52.1 (2004): 137-147.

[13] FRENZEL, J., et al. Influence of Ni on martensitic phase transformations in NiTi shape memory alloys. *Acta Materialia* 58.9 (2010): 3444-3458.

[14] FRENZEL, J., et al. On the effect of alloy composition on martensite start temperatures and latent heats in Ni–Ti-based shape memory alloys. *Acta Materialia* 90 (2015): 213-231.

[15] WAITZ, T. The self-accommodated morphology of martensite in nanocrystalline NiTi shape memory alloys. *Acta Materialia* 53.8 (2005): 2273-2283.

[16] ŠITTNER, P., et al. On the coupling between martensitic transformation and plasticity in NiTi: experiments and continuum based modelling. *Progress in Materials Science* 98 (2018): 249-298.

[17] HELLER, L., et al. Beyond the strain recoverability of martensitic transformation in NiTi. *International Journal of Plasticity* 116 (2019): 232-264.

[18] EGGELER, G., et al. Structural and functional fatigue of NiTi shape memory alloys. *Materials Science and Engineering: A* 378.1-2 (2004): 24-33.

[19] BENAFAN, O., et al. Thermomechanical cycling of a NiTi shape memory alloy-macroscopic response and microstructural evolution. *International Journal of Plasticity* 56 (2014): 99-118.

[20] SEDMÁK, P., et. al. Instability of cyclic superelastic deformation of NiTi investigated by synchrotron X-ray diffraction. *Acta Materialia* 94 (2015): 257-270.

[21] ÖLANDER, A. The crystal structure of AuCd. *Zeitschrift für Kristallographie-Crystalline Materials* 83.1-6 (1932): 145-148.

[22] ORTIN, J., and A. PLANES. Thermodynamic analysis of thermal measurements in thermoelastic martensitic transformations. *Acta metallurgica* 36.8 (1988): 1873-1889

[23] ORTIN, J., and A. PLANES. Thermodynamics of thermoelastic martensitic transformations. *Acta Metallurgica* 37.5 (1989): 1433-1441.

[24] ORTIN, J., and A. PLANES. Thermodynamics and hysteresis behaviour of thermoelastic martensitic transformations. *Le Journal de Physique IV* 1.C4 (1991): C4-13.

[25] BHATTACHARYA, K. *Microstructure of martensite: why it forms and how it gives rise to the shape-memory effect*. Vol. 2. Oxford University Press, (2003).

[26] BUEHLER, W. J., and F. E. WANG. A summary of recent research on the nitinol alloys and their potential application in ocean engineering. *Ocean Engineering* 1.1 (1968): 105-120.

[27] MEISNER, L. L., et al. Effect of nonmetallic and intermetallic inclusions on crater formation on the surface of TiNi alloys under the electron-beam impact. Procedia Structural Integrity 2 (2016): 1465-1472.

[28] CODA, A., et al. Characterization of inclusions in VIM/VAR NiTi alloys. Journal of materials engineering and performance 21.12 (2012): 2572-2577

[29] SHABALOVSKAYA, S, J. ANDEREGG, AND J. V. HUMBEECK. Critical overview of Nitinol surfaces and their modifications for medical applications. Acta Biomaterialia 4.3 (2008): 447-467.

[30] MIYAZAKI, S., et al. Lüders-like deformation observed in the transformation pseudoelasticity of a Ti Ni alloy. *Scripta Metallurgica* 15.8 (1981): 853-856.

[31] LIU, Y., et al. Asymmetry of stress–strain curves under tension and compression for NiTi shape memory alloys. *Acta materialia* 46.12 (1998): 4325-4338.

[32] LEO, P. H., T. W. SHIELD, and O. P. BRUNO. Transient heat transfer effects on the pseudoelastic behavior of shape-memory wires. *Acta Metallurgica et Materialia* 41.8 (1993): 2477-2485.

[33] O. LAURENT, and D. FAVIER. Stress-induced martensitic transformation of a NiTi alloy in isothermal shear, tension and compression. *Acta Materialia* 46.15 (1998): 5579-5591.

[34] SITTNER, P., Y. LIU, and V. NOVÁK. On the origin of Lüders-like deformation of NiTi shape memory alloys. *Journal of the Mechanics and Physics of Solids* 53.8 (2005): 1719-1746.

[35] FAVIER, D., et al. Mechanical instability of NiTi in tension, compression and shear. *IUTAM Symposium on Mechanics of Martensitic Phase Transformation in Solids*. Springer, Dordrecht, (2002).

[36] GADAJ, S. P., W. K. NOWACKI, and E. A. PIECZYSKA. Temperature evolution in deformed shape memory alloy. *Infrared physics & technology* 43.3-5 (2002): 151-155.

[37] SUN, Q., and Z. LI. Phase transformation in superelastic NiTi polycrystalline micro-tubes under tension and torsion—from localization to homogeneous deformation. *International Journal of Solids and Structures* 39.13-14 (2002): 3797-3809.

[38] SHAW, J. A., and S. KYRIAKIDES. Thermomechanical aspects of NiTi. *Journal of the Mechanics and Physics of Solids* 43.8 (1995): 1243-1281.

[39] SHAW, J. A., and S. KYRIAKIDES. On the nucleation and propagation of phase transformation fronts in a NiTi alloy. *Acta materialia* 45.2 (1997): 683-700.

[40] IADICOLA, M. A., and J. A. SHAW. The effect of uniaxial cyclic deformation on the evolution of phase transformation fronts in pseudoelastic NiTi wire. *Journal of Intelligent Material Systems and Structures* 13.2-3 (2002): 143-155.

[41] BRINSON, L. C., I. SCHMIDT, and R. LAMMERING. Stress-induced transformation behavior of a polycrystalline NiTi shape memory alloy: micro and macromechanical investigations via in situ optical microscopy. *Journal of the Mechanics and Physics of Solids* 52.7 (2004): 1549-1571.

[42] NG, K. L., and Q. P. SUN. Stress-induced phase transformation and detwinning in NiTi polycrystalline shape memory alloy tubes. *Mechanics of materials* 38.1-2 (2006): 41-56.

[43] XIAO, Y., P. ZENG, and L. LEI. Experimental investigation on local mechanical response of superelastic NiTi shape memory alloy. *Smart Materials and Structures* 25.1 (2015): 017002.

[44] JIANG, D., et al. Bending of pseudoelastic NiTi tubes. *International Journal of Solids and Structures* 124 (2017): 192-214.

[45] FROST, M., et al. Modeling of mechanical response of NiTi shape memory alloy subjected to combined thermal and non-proportional mechanical loading: a case study on helical spring actuator. *Journal of Intelligent Material Systems and Structures* 27.14 (2016): 1927-1938.

[46] XIAO, Y., et al. In situ observation on temperature dependence of martensitic transformation and plastic deformation in superelastic NiTi shape memory alloy. *Materials & Design* 134 (2017): 111-120.

[47] HECZKO, O., et al. "Magnetic domains and twin microstructure of single crystal Ni–Mn–Ga exhibiting magnetic shape memory effect." *IEEE Transactions on Magnetics* 51.11 (2015): 1-4.

[48] PIECZYSKA, E. A., et al. Thermomechanical investigations of martensitic and reverse transformations in TiNi shape memory alloy. *Bulletin of the Polish Academy of Sciences: Technical Sciences* (2004): 165-171.

[49] ALARCON, E., and L. HELLER. Deformation infrared calorimetry for materials characterization applied to study cyclic superelasticity in NiTi wires. *Materials & Design* 199 (2021): 109406.

[50] XIAO, Y., P. ZENG, and L. LEI. Effect of double-edge semi-circular notches on the mechanical response of superelastic NiTi shape memory alloy: Experimental observations. *The Journal of Strain Analysis for Engineering Design* 51.8 (2016): 555-562.

[51] BECHLE, N. J., and S. KYRIAKIDES. Localization in NiTi tubes under bending. *International Journal of Solids and Structures* 51.5 (2014): 967-980.

[52] DALY, S., G. RAVICHANDRAN, and K. BHATTACHARYA. Stress-induced martensitic phase transformation in thin sheets of Nitinol. *Acta Materialia* 55.10 (2007): 3593-3600.

[53] REEDLUNN, B., et al. Tension, compression, and bending of superelastic shape memory alloy tubes. *Journal of the Mechanics and Physics of Solids* 63 (2014): 506-537.

[54] REEDLUNN, B., et al. Axial-torsion behavior of superelastic tubes: Part I, proportional isothermal experiments. *International Journal of Solids and Structures* 199 (2020): 1-35.

[55] SEDMÁK, P., et al. Grain-resolved analysis of localized deformation in nickel-titanium wire under tensile load." *Science* 353.6299 (2016): 559-562.

[56] FROST, M., et al. Reconstruction of phase distributions in NiTi helical spring: comparison of diffraction/scattering computed tomography and computational modeling. *Smart Materials and Structures* 29.7 (2020): 075036.

[57] KIMIECIK, M., J. W. JONES, and S. DALY. Quantitative Studies of microstructural phase transformation in Nickel–Titanium. *Materials Letters* 95 (2013): 25-29.

[58] DELVILLE, R., et al. Transmission electron microscopy investigation of dislocation slip during superelastic cycling of Ni–Ti wires. *International Journal of Plasticity* 27.2 (2011): 282-297.

[59] DELVILLE, R., et al. Microstructure changes during non-conventional heat treatment of thin Ni–Ti wires by pulsed electric current studied by transmission electron microscopy. *Acta Materialia* 58.13 (2010): 4503-4515.

[60] MOLNÁROVÁ, O., et al. 3D Reconstruction of martensitic microstructures in grains of deformed nanocrystalline NiTi wires by TEM. *Available at SSRN 3797420* (2021).

[61] GAO, Y., et al. An origin of functional fatigue of shape memory alloys. *Acta Materialia* 126 (2017): 389-400.

[62] MALETTA, C., et al. Fatigue properties of a pseudoelastic NiTi alloy: Strain ratcheting and hysteresis under cyclic tensile loading. *International Journal of Fatigue* 66 (2014): 78-85.

[63] URBANO, M. F., et al. Inclusions size-based fatigue life prediction model of NiTi alloy for biomedical applications. *Shape Memory and Superelasticity* 1.2 (2015): 240-251.

[64] WANG, X. M., et al. The effect of notches on the fatigue behavior in NiTi shape memory alloys. *Materials Science and Engineering: A* 610 (2014): 188-196.

[65] PELTON, A. R., et al. Fatigue and durability of Nitinol stents. *Journal of the mechanical behavior of biomedical materials* 1.2 (2008): 153-164.

[66] PELTON, A. R. Nitinol fatigue: a review of microstructures and mechanisms. *Journal of Materials Engineering and Performance* 20.4 (2011): 613-617.

[67] ROBERTSON, S. W., A. R. Pelton, and R. O. Ritchie. Mechanical fatigue and fracture of Nitinol. *International Materials Reviews* 57.1 (2012): 1-37.

[68] WU, Y., et al. Deshielding effects on fatigue crack growth in shape memory alloys-A study on CuZnAl single-crystalline materials. *Acta Materialia* 176 (2019): 155-166.

[69] CASATI, R., et. al. Effect of electrical heating conditions on functional fatigue of thin NiTi wire for shape memory actuators. Procedia Engineering 10 (2011): 3423-3428.

[70] MAHTABI, M. J., et al. Fatigue of Nitinol: The state-of-the-art and ongoing challenges. Journal of the mechanical behavior of biomedical materials 50 (2015): 228-254.

[71] RAHIM, M., et al. Bending rotation HCF testing of pseudoelastic Ni-Ti shape memory alloys. *Materialwissenschaft und Werkstofftechnik* 44.7 (2013): 633-640.

[72] TAKEDA, Kohei, et al. Enhancement of fatigue life in TiNi shape memory alloy by ultrasonic shot peening. *Materials Transactions* (2015): MBW201408.

[73] RAHIM, M., et al. Impurity levels and fatigue lives of pseudoelastic NiTi shape memory alloys. Acta Materialia 61.10 (2013): 3667-3686.

[74] GOLLERTHAN, S., et al. Fracture mechanics and microstructure in NiTi shape memory alloys. *Acta Materialia* 57.4 (2009): 1015-1025.

[75] BAXEVANIS, T., and D. C. LAGOUDAS. Fracture mechanics of shape memory alloys: review and perspectives. *International Journal of Fracture* 191.1-2 (2015): 191-213.

[76] Handbook, A. S. M. VOLUME 12: Fractography. *ASM International* 517 (2004): 654.

[77] MUGHRABI, H. Fatigue, an everlasting materials problem-still en vogue. *Procedia Engineering* 2.1 (2010): 3-26.

[78] BUENCONSEJO, P. J. S., H. Y. KIM, and S. MIYAZAKI. Effect of ternary alloying elements on the shape memory behavior of Ti–Ta alloys. *Acta materialia* 57.8 (2009): 2509-2515.

[79] KIM, H. Y., and S. MIYAZAKI. Ni-free Ti-based shape memory alloys. (2018).

[80] PERKINS, J. Lattice transformations related to unique mechanical effects. *Metallurgical Transactions* 4.12 (1973): 2709-2721.

[81] MIYAZAKI, S., Y. IGO, and K. OTSUKA. Effect of thermal cycling on the transformation temperatures of Ti-Ni alloys. *Acta metallurgica* 34.10 (1986): 2045-2051.

[82] SIMON, T., et al. On the multiplication of dislocations during martensitic transformations in NiTi shape memory alloys. *Acta Materialia* 58.5 (2010): 1850-1860.

[83] ATLI, K. C., et al. Influence of crystallographic compatibility on residual strain of TiNi based shape memory alloys during thermo-mechanical cycling. *Materials Science and Engineering: A* 574 (2013): 9-16.

[84] NORFLEET, D. M., et al. Transformation-induced plasticity during pseudoelastic deformation in Ni–Ti microcrystals. *Acta Materialia* 57.12 (2009): 3549-3561.

[85] LIU, Y., G. TAN, and S. MIYAZAKI. Deformation-induced martensite stabilisation in [1 0 0] single-crystalline Ni–Ti. *Materials Science and Engineering: A* 438 (2006): 612-616.

[86] WAGNER, M. F. X., N. NAYAN, and U. RAMAMURTY. Healing of fatigue damage in NiTi shape memory alloys. *Journal of Physics D: Applied Physics* 41.18 (2008): 185408.

[87] GALL, K., and H. J. MAIER. Cyclic deformation mechanisms in precipitated NiTi shape memory alloys. *Acta Materialia* 50.18 (2002): 4643-4657.

[88] CUI, J., et al. Combinatorial search of thermoelastic shape-memory alloys with extremely small hysteresis width. *Nature materials* 5.4 (2006): 286-290.

[89] GROSSMANN, Ch, et al. Elementary transformation and deformation processes and the cyclic stability of NiTi and NiTiCu shape memory spring actuators. *Metallurgical and Materials Transactions A* 40.11 (2009): 2530-2544.

[90] CHLUBA, C., et al. Effect of crystallographic compatibility and grain size on the functional fatigue of sputtered TiNiCuCo thin films. *Philosophical Transactions of the Royal Society A: Mathematical, Physical and Engineering Sciences* 374.2074 (2016): 20150311.

[91] CHLUBA, Ch., et al. Ultralow-fatigue shape memory alloy films. *Science* 348.6238 (2015): 1004-1007.

[92] MALARD, B., et al. In situ investigation of the fast microstructure evolution during electropulse treatment of cold drawn NiTi wires. *Acta Materialia* 59.4 (2011): 1542-1556.

[93] DIMAKOS, K.s, A. MARIOTTO, and F. GIACOSA. Optimization of the fatigue resistance of Nitinol stents through shot peening. *Procedia Structural Integrity* 2 (2016): 1522-1529.

[94] YE, Ch., et al. Bimodal nanocrystallization of NiTi shape memory alloy by laser shock peening and post-deformation annealing. *Acta materialia* 59.19 (2011): 7219-7227.

[95] DEARNALEY, G., and N. E. W. HARTLEY. Ion implantation into metals and cabrides. *Thin Solid Films* 54.2 (1978): 215-232.

[96] BIGEON, M. J., and M. MORIN. Thermomechanical study of the stress assisted two way memory effect fatigue in TiNi and CuZnAl wires. *Scripta materialia* 35.12 (1996).

[97] TREADWAY, J., et al. Tensile and fatigue behavior of superelastic shape memory rods. *Materials & Design* 86 (2015): 105-113.

[98] MOLNÁROVÁ, O., ŠITTNER, P., VESELÝ, J., & M. CIESLAR. TEM analysis of deformation bands created by tensile deformation of superelastic NiTi wires. *Materials Characterization*, *167*, (2020), 110470.

[99] CHEN, Y., et al. Temperature and microstructure dependence of localized tensile deformation of superelastic NiTi wires. *Materials & Design* 174 (2019): 107797.

[100] ŠITTNER, P., SEDLÁK, P., SEINER, H., SEDMÁK, P., PILCH, J., DELVILLE, R., ... & L. KADEŘÁVEK. On the coupling between martensitic transformation and plasticity in NiTi: Experiments and continuum based modelling. *Progress in Materials Science*, *98*, (2018), 249-298.

[101] PILCH, J., L. HELLER, and P. SITTNER. Final thermomechanical treatment of thin NiTi filaments for textile applications by electric current. European Symposium on Martensitic Transformations. EDP Sciences, (2009).

[102] CHEN, Y., MOLNÁROVÁ, O., TYC, O., KADEŘÁVEK, L., HELLER, L., & P. ŠITTNER. Recoverability of large strains and deformation twinning in martensite during tensile deformation of NiTi shape memory alloy polycrystals. *Acta Materialia*, *180*, (2019), 243-259.

[103] BIAN, X., HELLER, L., KADEŘÁVEK, L., & P. ŠITTNER. In-situ synchrotron X-ray diffraction texture analysis of tensile deformation of nanocrystalline NiTi wire in martensite state. *Applied Materials Today*, *26*, (2022), 101378.

[104] BENEŠOVÁ, B., FROST, M., KADEŘÁVEK, L., ROUBÍČEK, T., & P. SEDLÁK. An experimentally-fitted thermodynamical constitutive model for polycrystalline shape memory alloys. *Discrete and Continuous Dynamical Systems-S*, *14*(11), (2021), 3925-3952.

[105] ŠITTNER, P., HELLER, L., SEDLÁK, P., CHEN, Y., TYC, O., MOLNÁROVÁ, O., ... & H. SEINER. B2⇒ B19′⇒ B2T martensitic transformation as a mechanism of plastic deformation of NiTi. *Shape Memory and Superelasticity*, *5*(4), (2019), 383-396.

[106] ŠITTNER, P., SEDLÁK, P., SEINER, H., SEDMÁK, P., PILCH, J., DELVILLE, R., ... & L. KADEŘÁVEK. On the coupling between martensitic transformation and plasticity in NiTi: experiments and continuum based modelling. *Progress in Materials Science*, *98*, (2018), 249-298.

[107] KADEŘÁVEK, L., ŠITTNER, P., MOLNÁROVÁ, O., KLIMŠA, L., & L. HELLER. Localized Plastic Deformation of Superelastic NiTi Wires in Tension. Shape Memory and Superelasticity, (2023), 1-19.

[108] CONSIDERE, M. *Mémoire sur l'emploi du fer et de l'acier dans les constructions*. Vue Ch. Dunod. (1885).

[109] SEINER H., The (20–1) interfaces in plastically formed NiTi martensite-twins or 'kwinks'? Presentation 1 available online from ASM international, https://www.asminternational.org/news/videos//journal_content/56/10192/42847968/VIDEO

[110] ŠITTNER, P., MOLNÁROVÁ, O., KADEŘÁVEK, L., TYC, O., & L. HELLER. Deformation twinning in martensite affecting functional behavior of NiTi shape memory alloys. *Materialia*, *9*, (2020), 100506.

[111] CHEN, Y., LI, A., MA, Z., ZHANG, H., JIANG, D., REN, Y., & L. CUI. Achieving Strength-Ductility Synergy via Huge Lüders-Type Deformation. *Available at SSRN 3834116*.

[112] ZHANG, X., FENG, P., HE, Y., YU, T., and Q. SUN. Experimental study on rate dependence of macroscopic domain and stress hysteresis in NiTi shape memory alloy strips. *International Journal of Mechanical Sciences*, *52*(12), (2010). 1660-1670

[113] POLATIDIS, E., ŠMÍD, M., KUBĚNA, I., HSU, W. N., LAPLANCHE, G., and H. VAN SWYGENHOVEN. Deformation mechanisms in a superelastic NiTi alloy: An in-situ high resolution digital image correlation study. *Materials & Design*, *191*, (2020). 108622.

[114] AMMAR, O., HADDAR, N., & L. DIENG. Experimental investigation of the pseudoelastic behaviour of NiTi wires under strain-and stress-controlled cyclic tensile loadings. *Intermetallics*, *81*, (2017), 52-61

[115] ZHENG, L., HE, Y., & Z. MOUMNI. Effects of Lüders-like bands on NiTi fatigue behaviors. *International Journal of Solids and Structures*, *83*, (2016), 28-44.

[116] XIE, X., KAN, Q., KANG, G., LU, F., & K. CHEN. Observation on rate-dependent cyclic transformation domain of super-elastic NiTi shape memory alloy. *Materials Science and Engineering: A*, *671*, (2016), 32-47.

[117] HAGHGOUYAN, B., HAYRETTIN, C., BAXEVANIS, T., KARAMAN, I., & D. C. LAGOUDAS. Fracture toughness of NiTi–Towards establishing standard test methods for phase transforming materials. *Acta Materialia*, *162*, (2019), 226-238.

[118] PAUL, P. P., FORTMAN, M., PARANJAPE, H. M., ANDERSON, P. M., STEBNER, A. P., & L. C. BRINSON. Influence of structure and microstructure on deformation localization and crack growth in NiTi shape memory alloys. *Shape Memory and Superelasticity*, *4*(2), (2018), 285-293.

[119] ZHENG, L., HE, Y., & Z. MOUMNI. Investigation on fatigue behaviors of NiTi polycrystalline strips under stress-controlled tension via in-situ macro-band observation. *International Journal of Plasticity*, *90*, (2017), 116-145.

[120] WANG, X. M., LU, Z. Z., & Z. F. YUE. The effect of notches on the fracture behavior in NiTi shape memory alloys. *International Journal of Solids and Structures*, *46*(3-4), (2009), 557-571.

[121] SITTNER, P., IAPAROVA, E., KADEŘÁVEK, L., CHEN, Y., & O. TYC. Tensile Deformation of Niti Shape Memory Alloy Thermally Loaded Under Applied Stress. *Available at SSRN 4240593*.

[122] MOLNAROVA, O., TYC, O., HELLER, L., SEINER, H., & P. ŠITTNER. Evolution of martensitic microstructures in nanocrystalline NiTi wires deformed in tension. *Acta Materialia*, *218*, (2021), 117166.